Summer 8-15-2017

Weak Measurement and Quantum Smoothing of a Superconducting Qubit

Dian Tan
Washington University in St. Louis

WASHINGTON UNIVERSITY IN ST. LOUIS

Department of Physics

Dissertation Examination Committee:
Kater Murch, Chair
Erik Henriksen
Henric Krawczynski
Alexander Seidel
David Wisbey

Weak Measurement and Quantum Smoothing of a Superconducting Qubit

by

Dian Tan

A dissertation presented to
The Graduate School
of Washington University in
partial fulfillment of the
requirements for the degree
of Doctor of Philosophy

August 2017

Saint Louis, Missouri

Table of Contents

List of Figures

Acknowledgements

I am deeply indebted to many great people that I have met in the last five years. Most importantly, I would like to thank my advisor Professor Kater Murch for the opportunity to work in the his group and for all of his guidance over these years. Being his first student is definitely a great honor for me and a persistent motivation to push me forward. I still remember how naive I was about my research including sample fabrication, data analysis, and quantum measurement techniques when I first joined the lab. But at last it turned out that it is a super rewarding experience working with him. It is Kater with his great patience, wisdom, always correct intuitions and wonderful ideas, who made my PhD research smooth and productive. Without Kater, I would have never achieved so much in my PhD research. How I wish that I could have learned more from him. Moreover, his passion and dedication to science and life will always inspire and encourage me in my future career. I would also never forget the lab dinners at his house where he also taught me how to make Pizza.

I am very thankful to Professor Klaus Mølmer whom I benefited from a lot. The theoretical part of all my thesis work is done with his collaboration. I am always impressed by his fabulous ideas during our discussion and have enjoyed a lot working with him in the past three years.

I would like to thank Professors Erik Henriksen, Henric Krawczynski, Alexander Seidel, David Wisbey for sitting in my committee and for their insightful comments on my thesis.

I would also like to thank everyone in the Murch lab for all the support, encouragement and conversations. Especially, I would like to thank Neda Foroozani for her mentoring in my first year and her wise advice to me regarding my future ca-

reer. I would also like to thank Mahdi Naghiloo for his help in experiments and his wife Fatemeh Naghiloo for bringing us delicious Iranian food. I would like to thank Patrick Harrington for preparing the reception of my dissertation defense. I would particularly like to thank Jonathon Monroe for proofreading my thesis. I would also like to thank all the undergraduates in the Murch lab, past and present for finishing all their projects making our measurements much easier.

The staff in the physics department, Debbie, Sarah, Tammy, Linda, Patty, Alison, David, Todd and Tony are always willing to help me during the past five years. I am very grateful for them to make my life much more convenient in the department.

Finally, I owe many thanks to my friends and my family who are always supporting me and believing in me in the past years. Especially, I would like to thank my mother and my wife for their love all these years. Words cannot express how grateful I am to them.

Dian Tan

Washington University in St. Louis

August 2017

Dedicated to my family.

ABSTRACT OF THE DISSERTATION

Weak Measurement and Quantum Smoothing of a Superconducting Qubit

by

Dian Tan

Doctor of Philosophy in Physics

Washington University in St. Louis, 2017

Professor Kater Murch, Chair

In quantum mechanics, the measurement outcome of an observable in a quantum system is intrinsically random, yielding a probability distribution. The state of the quantum system can be described by a density matrix $\rho(t)$, which depends on the information accumulated until time t, and represents our knowledge about the system. The density matrix $\rho(t)$ gives probabilities for the outcomes of measurements at time t. Further probing of the quantum system allows us to refine our prediction in hindsight. In this thesis, we experimentally examine a quantum smoothing theory in a superconducting qubit by introducing an auxiliary matrix $E(t)$ which is conditioned on information obtained from time t to a final time T. With the complete information before and after time t, the pair of matrices $[\rho(t), E(t)]$ can be used to make smoothed predictions for the measurement outcome at time t. We apply the quantum smoothing theory in the case of continuous weak measurement unveiling the retrodicted quantum trajectories and weak values. In the case of strong projective measurement, while the density matrix $\rho(t)$ with only diagonal elements in a given basis $|n\rangle$ may be treated as a classical mixture, we demonstrate a failure of this classical mixture description in determining the smoothed probabilities for the measurement outcome at time t with both diagonal $\rho(t)$ and diagonal $E(t)$. We study the correlations between quantum states and weak measurement signals and examine aspects of the time symmetry of continuous quantum measurement. We also extend

our study of quantum smoothing theory to the case of resonance fluorescence of a superconducting qubit with homodyne measurement and observe some interesting effects such as the modification of the excited state probabilities, weak values, and evolution of the predicted and retrodicted trajectories.

Chapter 1

Introduction

The past decade has seen remarkable experimental progress in the field of quantum information and quantum foundations using superconducting quantum circuits [1, 2]. One of the main components in this field is the superconducting quantum bit which is essentially an anharmonic oscillator, comprised of Josephson junctions shunted by a large capacitor, providing the lowest two energy levels as the qubit. Superconductivity and the Josephson effect are the key elements to the successful application of the quantum circuits. Superconductivity, which is the frictionless flow of electrical fluid through the metal below a critical temperature, ensures that the qubit will show its quantum properties without loss, and the Josephson effect provides nonlinearity without introducing dissipation or dephasing which is crucial for manipulation and state control of the qubit [3]. Nowadays, superconducting transmon qubits have been demonstrated with coherence times exceeding 100 μs [4, 5], a four-order-of-magnitude increase in coherence compared with the first Cooper-pair box qubit [6]. With such long coherence times superconducting qubits are becoming an ideal platform to perform quantum computing and to investigate the foundations of quantum mechanics in an unprecedented way [7, 8].

Superconducting qubits are typically operated with characteristic frequencies, ω in the gigahertz frequency range and are compatible with microwave techniques. Gigahertz frequencies mean microwave photons which are three orders of magnitude below thermal energy at room temperature, and thus require very low temperature

which is achievable with a dilution refrigerator. Moreover, because the dipole moment of the qubit is sufficiently large, strong coupling to microwave modes and microwave photons is possible. Thus we can use microwave photons to manipulate and readout the state of the qubit [9].

The circuit quantum electrodynamics formalism allows us to describe this interaction and utilize it for quantum information purposes. Using a commercial dilution refrigerator with the capability of cooling to temperatures of a few milikelvin, we can utilize microwave techniques to explore the quantum properties of superconducting qubits when the temperature T is cold enough such that the thermal energy is much less than the qubit transition energy, $k_B T \ll \hbar\omega_q$, where ω_q is the qubit frequency, and k_B is Boltzmann's constant.

The quantum properties we wish to observe have a much smaller energy scale than that of the classical measurement instruments. For example, if the mean photon number in a driven cavity is around 1, then the output power from the cavity with its resonant frequency $\omega_r/2\pi = 6$ GHz and bandwidth $\kappa = 10$ MHz is on the order of -140 dBm (10^{-17} watts) while the typical powers used in the microwave signal processing at room temperature are on the order of -30 dBm, thus large amplifications are required in order to detect such tiny signals at room temperature. Note that minimum cell phone signal is -113 dBm. For example, a typical cell phone signal strength is between -100 dBm and -50 dBm (LTE Network "5 bars" is about -50 dBm). Amplifiers typically add noise to the signals that are amplified. This can be expressed in terms of a noise temperature T_N or in terms of added photons $N = k_B \times T_N/\hbar\omega$. Fortunately, much progress has been made on detecting such minuscule signals. The first important improvement making the detection possible is the development of cryogenic High-Electron-Mobility Transistors (HEMT) amplifiers which work at the temperature 4 K and reduce the added noise significantly by approximately two orders of magnitude compared to room-temperature amplifiers [10]. The typical HEMT amplifiers can be operated in the range of 1 to 12 GHz with more than 30 dB gain and their added noise is at the level of 20 photons. Thus by only using the HEMT amplifier, the quantum efficiency, which is the ratio of vacuum noise to total noise (1/2)/(N+1/2)

is limited to around 1%.

Despite the excellent performance of the HEMT amplifiers at 4 K stage, the noise level still remains much higher than zero-point fluctuations, $k_B T_N \gg \hbar\omega/2$. Such a low quantum efficiency prevents the use of quantum measurement back-action as a resource for quantum control. The quantum efficiency η basically indicates how close a measurement comes to ideal Heisenberg-limited back-action (how much information that we collect).

The technological advance that enables the research described in this thesis is the quantum-limited Josephson parametric amplifier. Using these, it is possible to dramatically improve the quantum efficiency thereby enabling a number of experiments that probe the physics of quantum measurement. The first Josephson parametric amplifier was demonstrated by Yurke in the 1980's by employing microwave and nanofabrication techniques [11, 12]. These parametric amplifiers were further investigated by several groups [13–19]. Nowadays, the use of Josephson parametric amplifiers has reduced the noise level of microwave measurements by one more order of magnitude with quantum-limited performance. Josephson parametric amplifiers can in principle operate noiselessly, adding zero photons of noise [20]. Significant research has been invested in studying this limit while many experiments have demonstrated 70-80 % efficiency [21], others have placed limits on the intrinsic inefficiency of the amplifier as high as 99% [22]. Once all the other losses in the measurement chain are taken into account, the overall quantum efficiency we typically achieve is between 30% and 50%.

Due to the remarkable recent progress in the fabrication of quantum circuits including superconducting qubits and parametric amplifiers, it is possible for us study the problems in quantum information and quantum foundations in a marriage of quantum mechanics, parameter estimation theory and nanoscale engineering in the context of quantum measurements.

1.1 Superconducting quantum circuits

Richard Feynman said "We are really getting control of nature on a very delicate and beautiful level" [23]. Indeed, progress in fabricating and understanding superconducting circuits has enabled us to conduct experiments to test quantum mechanics in a way that only existed in thought experiments before. Moreover, such control would eventually lead to the success of quantum computers based on superconducting circuits with potential applications in quantum simulation, optimization, factorization, and finding eigenvalues of large Hamiltonians [24–31].

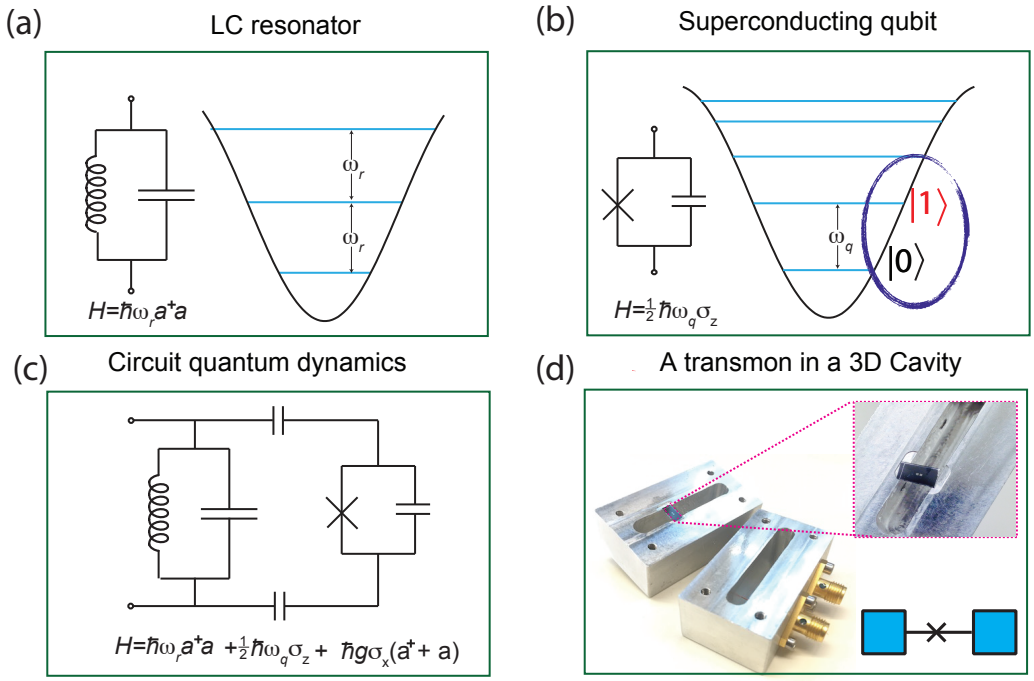

Figure 1.1: Lumped element model for quantum circuits. (a) A microwave LC resonator. (b) A qubit. (c) Qubit-cavity hybrid system. (d) A transmon qubit in a 3D Al cavity.

1.1.1 Superconducting qubits

Superconducting qubits exhibit quantized energy states of electronic charge, magnetic flux or junction phase, corresponding to different types of superconducting qubits

[32, 33]: charge qubit [34], flux qubit [35] and phase qubit [36, 37]. The type of the qubit depends on the design parameters of the constituent circuit elements such as capacitors, inductors and Josephson junctions. In this thesis, as illustrated in Fig. 1.1(b, d) we only focus on the transmon qubit which is typically a charge qubit but with large capacitance in order to suppress the charge noise in this device [38]. Besides superconducting qubits, there are also other realizations of quantum two state systems: atoms [39] or ions [40], nitrogen vacancy centers [41, 42], polarizations of a photon [43], and quantum dots [44]. However, compared to other two level systems, superconducting qubits have many advantages. Thus, they are considered as one of the most likely candidate for the applications of quantum information science and technology. First, the Hamiltonian of the quantum system can be particularly adjusted since parameters of the devices can be engineered in design. Second, superconducting circuits are compatible with microwave control and can be operated at nanosecond time scales thus we can take the advantage of the well developed microwave tools. Moreover, the superconducting qubits can be easily scaled up in a chip using lithographic techniques.

Spectacular improvement has been made over the past decade in the field of superconducting circuits which brought these devices from a scientific curiosity to technological reality. In the year of 1999, the first superconducting qubit was made by NEC group and coherent oscillations were observed in this qubit [6]. Therefore it has proven possible that we can put these qubits into coherent superposition states so that they can act as quantum bits. 18 years later, IBM just announced that it has built two new universal quantum computers which have 16 and 17 superconducting qubits respectively, and Google is testing a 20-qubit quantum computer and aims to make a 49-qubit computer that can solve problems far beyond the capacity of ordinary computers (Quantum supremacy) by the end of 2017. While the goal of creating future quantum computers that can be used to solve some hard problems far beyond the capability of classical computers, has driven the development of superconducting qubits, these devices can be also employed as a testbed to study fundamental physics such as quantum control, quantum measurement, and quantum feedback.

1.1.2 Josephson parametric amplifiers

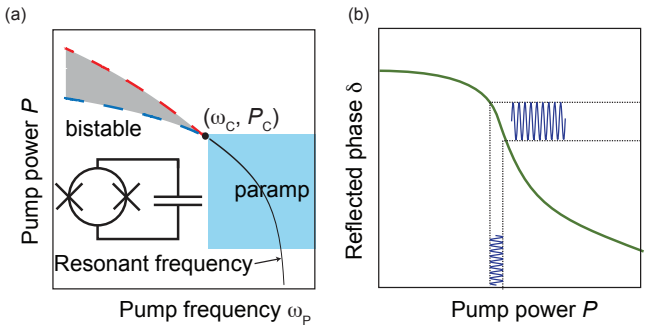

Figure 1.2: Josephson parametric amplifier. (a) The resonance response is linear at low pump power. As the pump power increases, the nonlinear response of JPA appears and the JPA goes into a regime labeled as paramp and shaded in blue. After a critical point, (ω_c, P_c), the JPA goes into a bifurcated regime. (b) The paramp transfer function shows that the small input sinusoidal signal can be mapped to the phase of the reflected pump, indicating the amplication of the input signal.

In this thesis, the parametric amplifier that we use is called a lumped element Josephson Parametric amplifier (LJPA) [45, 46]. The term parametric implies that some parameter of the Josephson parametric amplifiers can be periodically modulated by a pump signal in order to achieve gain by transferring power from the pump to a signal at some frequency. If we consider that the amplifier is driven at a frequency with some power at which the reflected phase δ is very sensitive to power (the region displayed in Fig. 1.2(b)), and then the system will show strong response to small perturbations which are caused by the tiny signal field thus we can have gain. A similar process in quantum optics modulates the refractive index of a nonlinear medium with a pump to affect the modes which are detuned from the pump thus stimulate population of the mode with photons provided by the pump [47]. As illustrated in Fig. 1.2(a) inset, the LJPA is a nonlinear resonator comprised of a SQUID loop of two large Josephson junctions and a capacitor. By adding a Josephson inductance inside a resonator, we can achieve parametric amplification in a well-controlled frequency band while suppressing it for frequencies outside. Fig. 1.2(a) displays the resonance response of the amplifier to the pump power. At low pump power, the response is linear meaning that the resonance frequency does not depend on the pump power. As

the power increases, the resonance bends to low frequencies and we go into a region where the non-linearity from the Josephson junction comes into play. This is the region labeled paramp where we operate the LJPA. As we further increase the pump power, the system goes into a bistable region where two stable solutions exist for the pumping frequency [48].

1.2 Introduction to quantum smoothing

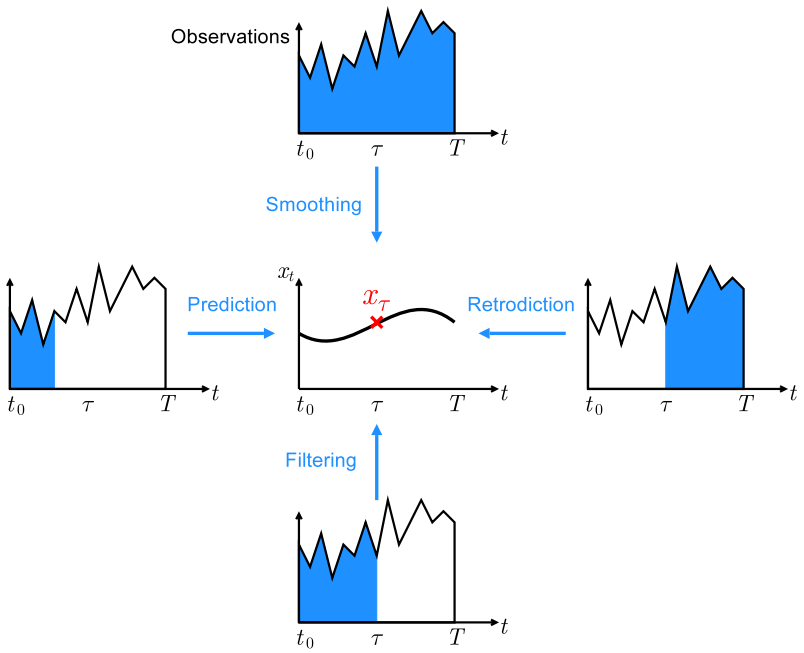

Figure 1.3: Four classes of estimation problems. Adapted from Tsang [49].

Estimation exists almost everywhere in our daily life. There are a lot of examples of estimation happening to us everyday. You may apply the estimation in cooking such as how much sauce, oil, salt, and other seasonings you like to use. You may estimate the temperature of hot water before you dip a tea bag to make a cup of tea. You may estimate what time you have to leave in the morning in order to be in the lab at 9 am. For making ends meet, you may have to estimate how much money you can spend this month in your bank account so you don't go over the limit. Moreover, if you

still have enough savings, this can help improving your estimation next month. Often we need to make an estimation if we don't know an exact answer in a guess of what would happen in our daily life. In science, estimation theory is used to determine the state of a system with the information obtained with observations. The information that is obtained before a measurement M on a system at time τ can be represented by a density matrix ρ which represents a state of knowledge. In this thesis we will anote "effect matrix", E, which is similiar to ρ, but encodes information obtained after the measurement from time τ to a final time T [50]. Thus the combination of ρ and E gives us complete information about the the state of the system. As illustrated in Fig. 1.3, estimation problems are usually classified into four classes: prediction, filtering, retrodiction, and smoothing. Prediction is the estimation of measurement outcome at time τ given observations before that time $(\rho(t), t < \tau)$. Filtering is the estimation given observations before and up to τ $(\rho(t), t \leq \tau)$. Retrodiction is obtained given observations after τ $(E(t), \tau < t \leq T)$ and smoothing is based on the observation before and after time τ $(\rho(t), t \leq \tau, E(t), \tau < t \leq T)$ [49]. Prediction and filtering have been studied extensively due to their real-time applications. Here we are focusing on the application of smoothing to make better parameter estimations in a quantum system. Moreover, we have the access to study some interesting pre- and post-selection effects with quantum trajectory theory.

Aharonov et al. [51–54] proposed and applied the concept of pre- and post-selected states to generate some fundamental questions and counter-intuitive phenomena in quantum physics such as weak values. Tsang in 2009 [49, 55] derived the probability conditioned on the complete measurement record and made a smoothed prediction for classical parameters that affect the evolution of a quantum system with the measurement results on the quantum system. He first applied the concept of smoothing from the classical system to the quantum system and enabled the application of quantum smoothing in quantum systems. Mølmer et. al. [50] generalized the quantum smoothing theory and proposed the past quantum state theory which can be used to better estimate an unknown result for a measurement performed on a quantum system at a time t with information both before and after time t. Wiseman et. al. defined a

smoothed quantum state which can enable better state estimation [56]. This thesis is devoted to the experimental tests of these quantum smoothing theories, in particular the Past Quantum State theory developed by Mølmer et al..

Quantum smoothing can be applied to the field of quantum sensing or communication which can give more accurate estimation of the signal at some time in the past. Quantum smoothing theory also offers us a way to formally make probability statements about what happen in the past given the later data. By taking the advantage of more accurate estimation with quantum smoothing, we are able to detect error occurrences in quantum measurements with quantum state tracking. With the capability of correcting the errors, we might apply feedback which is very important in quantum control [57–59].

1.3 Overview of the thesis

Chapter 2 presents some theoretical background relevant to experimental realizations of quantum measurement. In Particular, Section 2.5 describes the theoretical basis of Quantum Smoothing which is the basis of the experimental tests in this thesis. Chapter 3 discusses the application of quantum smoothing theory in the case of classical mixtures. This simplest application of smoothing reveals fundamental quantum features of measurement. In chapter 4, we describe experiments where we performed weak continuous measurement on a superconducting qubit. We study the predicted and retrodicted trajectories in continuous weak measurement using the quantum trajectory formalism. In chapter 5, with the technique of pre- and post-selection, we examine aspects of time-symmetry in a superconducting qubit by showing that the pre-selected average signal is the time reversal of the post-selected average signal in quantum measurement. We also study the correlations between the weak signal and the qubit state. Chapter 6 discusses the application of the Past Quantum State in homodyne detection for a quantum emitter which is comprised of a superconducting qubit resonant with a 3D aluminum cavity. We see several interesting pre- and post-selection effects in this system. In chapter 7, we conclude by giving future application

of the theory of Past Quantum State, e.g. tomography for the effect matrix E.

1.4 Summary of key results

The key results of the work presented in this thesis are in the following:

In our first experiment, we test Past Quantum State theory in the case of strong projective measurements where the density matrix ρ and the effect matrix E are both diagonal. We show that diagonal ρ can be treated as classical mixtures. However, the more complete description of the system involving E in addition to diagonal ρ is not equivalent to a classical mixture. Our experimental and theoretical results are in good agreement to support our conclusion [60].

In the second experiment, we have demonstrated the use of the quantum trajectory formalism to infer the quantum state of a superconducting qubit conditioned on the outcome of continuous measurement. The density matrix ρ, can be used to make predictions about the outcome of a measurement conducted at time t, if more information is available in the future, an effect matrix E which represents the information after time t can be used to make retrodictions about the measurements conducted at time t when t is in the past. Together, ρ and E, can be used to make a smoothed prediction for events in the past and give more confident predictions. This is the first time that these matrices have been calculated and applied to a fully quantum system in the context of continuous weak measurement [61].

In the third experiment, we study correlations between the weak signal and the state of a continuously monitored superconducting qubit with pre- and post-selection [62].

We have also applied the Past Quantum State formalism to a quantum emitter that was continuously monitored by homodyne detection in the last experiment of this thesis. We have experimentally confirmed these predictions for the average homodyne signal and furthermore observed anomalous weak values using the Past Quantum State theory. By employing quantum trajectory theory, we have studied the evolution of the emitter state by employing quantum trajectory theory, showing

that the evolution of these trajectories is stochastic, but are confined to deterministic regions at some time t in the Bloch sphere [63].

Chapter 2

Quantum mechanics and quantum measurement

In this Chapter, we introduce the basics of quantum measurement and superconducting qubits with a focus on the transmon qubit. We also provide a brief introduction to the basic principles of the circuit quantum electrodynamics. At the end of the chapter, we describe how we use such knowledge in a realistic experiment and how we apply quantum smoothing theory.

2.1 Measurement in quantum mechanics

It is well known that quantum mechanics has an inherently probabilistic nature regarding measurement outcomes of observables and that quantum measurement plays an essential role in the interpretation of quantum mechanics. This thesis is about measurement, and how recent experimental advances are helping reshape our understanding of measurement in quantum mechanics. Thus, before describing the experimental and theoretical work of this thesis, we briefly review the basic textbook descriptions of quantum measurement and develop the tools necessary for the work in this thesis.

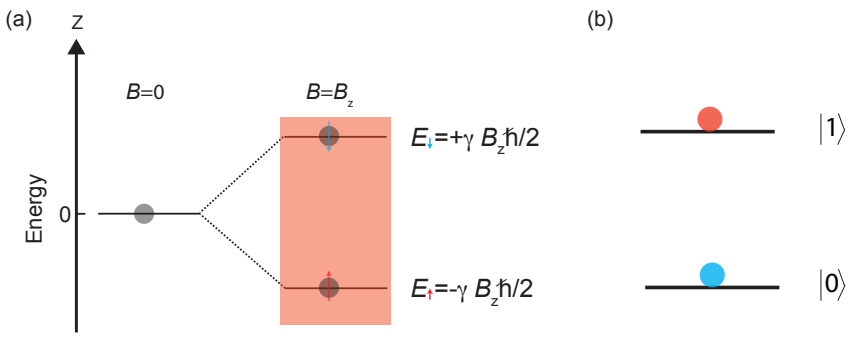

Figure 2.1: Energy levels for a spin 1/2 particle in a uniform magnetic field. (a) The the z component of the spin can be aligned either up or down, its energy level is going to split into two levels in the magnetic field due to the interaction between the magnetic dipole moment and the magnetic field. (b) A qubit being in its ground and excited state can realize a pseudo-spin 1/2 system.

2.1.1 Pseudo-spin 1/2

Let's first consider a spin 1/2 particle in a uniform magnetic field [64]. Its magnetic dipole moment μ is given by $\mu = \gamma \mathcal{S}$, here γ is the gyromagnetic ratio and $\mathcal{S}$ is the spin angular momentum. We can also calculate the energy in the magnetic field, $E = -\mu B = -\gamma \mathcal{S} B$. For a spin 1/2 particle in a magnetic field along z axis, we have $\mathcal{S}_z = \pm\hbar/2$ for spin up and spin down, thus its energy E will split into two levels as illustrated in Fig. 2.1. In this thesis, we borrow the concept of spin 1/2 and realize a pseudo-spin 1/2 system (qubit). The ground state $|0\rangle$ and the excited states $|1\rangle$, similar to the spin up and spin down respectively, realize a pseudo-spin 1/2 system which can be well described by the 2×2 density matrix $\rho(t)$. Furthermore, with this connection to the spin, we can use common known Pauli operator to describe the quantum state.

2.1.2 Stern-Gerlach experiment

A paradigm of quantum measurement is the Stern-Gerlach experiment which motivated major developments in modern physics and sheds light on quantum measurement [65]. The Stern-Gerlach experiment showed that a beam of rapidly moving neutral silver atoms, which were evaporated from an oven, traveled through an in-

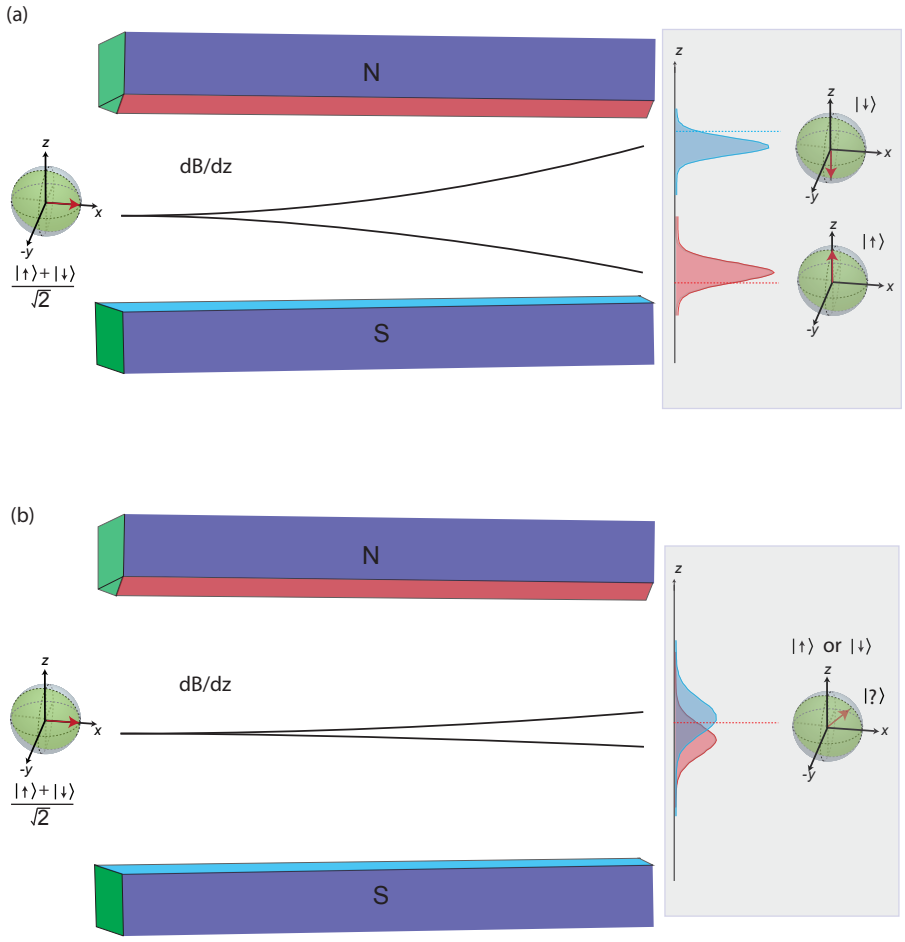

Figure 2.2: Stern-Gerlach experiment. The spins are initially in eigenstate of the $\mathcal{S}_x$ operator (aligned along x) and sent through the above Stern-Gerlach apparatus which measures z component of the spins. (a) If the magnetic field gradient is strong enough, then the spins would be deflected into two separated distributions after the Stern-Gerlach apparatus. (b) If the the magnetic field gradient is very weak, the distributions would have some overlap with each other.

homogeneous magnetic field and were deflected into two parts — some of the silver atoms are deflected up and some deflected down. As illustrated in Fig. 2.2(a), if we have some spins along the x axis, an eigenstate of σ_x, after the the Stern-Gerlach apparatus with large enough magnetic field gradient, dB/dz, we can obtain two separated distributions along the z axis which are associated with eigenvalues of σ_z. We assume that the distributions arise because the atoms are in Gaussian minimum uncertainty states. Therefore, we can distinguish whether the spins are up or down after the measurement and this is called strong projective measurement. Here $\sigma_u (u = x, y, z)$ are the Pauli spin operators that acts on the spin state. But if the magnetic field gradient is very weak, the distributions are overlapped thus we cannot distinguish whether the spins are up or down. This is known as weak measurement where only partial information about the spin state is extracted. The Stern-Gerlach experiment indicated that there must be an intrinsic property which is now known as spin angular momentum leading to these quantized results of measurement outcome. The Stern-Gerlach experiment is in agreement with the predictions for measurement outcomes in spin $\frac{1}{2}$ systems which paves ways for later developments in quantum measurement thus in the field of quantum information.

2.1.3 Born's rule

Born's rule gives us the probability of getting the outcomes of a measurement for a given observable. Let's give an example of a two level system. If a qubit is in the superposition state $|\psi\rangle = \alpha|0\rangle + \beta|1\rangle$, and a measurement is performed on this state in its energy eigenbasis (σ_z), then Born's rule tells us that the outcome of the measurement of the z component of the spin is $+1$, an eigenvalue of $\sigma_z|0\rangle = +1|0\rangle$ with probability $|\alpha|^2$ and -1 with probability $|\beta|^2$ [66]. This measurement is called von Neumann measurement which says that if we measure an observable A with a set of projection operators $\hat{P}_a = |a\rangle\langle a|$ for a system in a state $|\Psi\rangle$ and obtain a measurement result a then the state of the system is immediately in the state $|a\rangle$ after the measurement [67],

$$|\Psi\rangle \xrightarrow{\hat{P}_a} |a\rangle. \tag{2.1}$$

The von Neumann measurements performed on the system are instantaneous and non-unitary (irreversible), causing the wave function collapse to one of its eigenstates. For example, if we have a two level system which is initially prepared in its superposition state,

$$|\psi_i\rangle = \frac{(|0\rangle + |1\rangle)}{\sqrt{2}}. \tag{2.2}$$

A projective measurement performed on this system will collapse the system in one of its eigenstate $|0\rangle$ ($|1\rangle$) with eigenvalue +1 (-1) in σ_z basis. Moreover, we know that the measurement causes z-component of the spin to change from 0 to +1 or -1 and x-component of the spin from 1 to 0. After the measurement, we know the z-component of the spin for sure but we know "nothing" about the x-component of the spin. This is due to the back-action from the quantum measurement. Why does this happen? Because of the Heisenberg uncertainty principle, two non-commuting observables cannot be measured to a infinite precision simultaneously, if the measurement has been performed in σ_z basis, then the information about σ_x is lost due to the strong projective measurement in this basis [68].

2.1.4 Aharonov-Bergmann-Lebowitz rule

In this section, we discuss measurement probability conditioned on both the initial state $|\psi_i\rangle$ and final state $|\psi_f\rangle$ which is given by Aharonov-Bergmann-Lebowitz rule (ABL rule) [69, 70]. Based on Born's rule we know that the probability for the measurement outcome a of an observable $\hat{A}$ at time t is $P(a) = |\langle a|\psi_i\rangle|^2$, yet after this measurement, the system can be subjected to further probing, and the probability that the system will be found in state $|\psi_f\rangle$ conditioned on the system which has already been observed in the state $|a\rangle$ is $P(f|a) = |\langle\psi_f|a\rangle|^2$. So the probability that system yields outcome a and is subsequently detected in a final state $|\psi_f\rangle$ is given by the product of the above two probabilities: $P(f,a) = P(f|a)P(a) = |\langle\psi_f|a\rangle|^2|\langle a|\psi_i\rangle|^2$. The probability that the system will be observed in state $|\psi_f\rangle$, given a measurement of $\hat{A}$ has been performed with all possible measurement results a (not necessary known to us) is $P(f) = \sum_{a'} P(f,a') = \sum_{a'} |\langle\psi_f|a'\rangle\langle a'|\psi_i\rangle|^2$. With the above probabilities and

by applying Bayes' theorem, we have the probability $P_{ABL}(a)$ for the measurement of $\hat{A}$ is a, if we consider only the selected measurement events where the initial state was $|\psi_i\rangle$ and the final state was $|\psi_f\rangle$,

$$P_{ABL}(a) = P(a|f) = \frac{|\langle\psi_f|a\rangle|^2|\langle a|\psi_i\rangle|^2}{\sum_{a'}|\langle\psi_f|a'\rangle\langle a'|\psi_i\rangle|^2}. \tag{2.3}$$

ABL rule is in essence a conditional probability which provides a time-symmetric description of quantum mechanics, leading to a series of interesting pre- and post-selected effects such as anomalous weak values [51–53, 71], that we will return to later in this thesis.

2.2 Superconducting qubits

The two level quantum system being used in this thesis is the superconducting transmon qubit. We first show that how to quantize a classical electrical circuit. After that, we examine the basics of the transmon qubit.

2.2.1 Quantization of an electrical circuit

In this section, we will give an example to briefly show the method of quantizing an LC resonator in order to understand how we make an electric circuit behave as a qubit. There are more thorough derivations regarding the details of the circuit quantization in the references [3, 72, 73].

Let's consider a simple electronic circuit which consists of a capacitor, C, in parallel with an inductor, L. We have the following relations for the current across the capacitor, $I_C = C\frac{dV_c}{dt}$, and the voltage drop across the inductor, $V_L = L\frac{dI_L}{dt}$. We know that $I_C = I_L = I$ and $V_C = -V_L = V$ based on Kirchoff's rule. Therefore, we have

$$\frac{d^2I}{dt^2} = -\frac{1}{LC}I, \tag{2.4}$$

then we have the solution $I(t) = A\cos(\omega t) + B\sin(\omega t)$, where $\omega = \frac{1}{\sqrt{LC}}$, A and B are constants determined by initial conditions. Apparently, the LC circuit behaves as a

simple harmonic oscillator. The total energy of the oscillator E is given by

$$E = \frac{1}{2}LI^2 + \frac{1}{2}CV^2, \tag{2.5}$$

thus the Hamiltonian of the LC circuit can be expressed as

$$H = \frac{\Phi^2}{2L} + \frac{Q^2}{2C}, \tag{2.6}$$

where we use the relation for magnetic flux in the inductor, $\Phi = LI$, and the charge on the capacitor, $Q = CV$.

Moreover, we can have the following relations [74],

$$\frac{\partial H}{\partial \Phi} = \Phi/L = I = \dot{Q}, \qquad \frac{\partial H}{\partial Q} = Q/C = -LI = -\dot{\Phi}. \tag{2.7}$$

Hence we know the pair Φ and Q are canonical variables and can be written as operators. This pair satisfies the commutation relation $[\hat{\Phi}, \hat{Q}] = i$.

2.2.2 Superconducting transmon qubit

A harmonic oscillator can not be used as a qubit since its energy levels are equally separated. Fortunately, we have the Josephson junction which is crucial for realizing a superconducting qubit due to its non-linearity and lack of dissipation. In order to build a circuit which provides this harmonic oscillator potential we need an inductor and a capacitor. Josephson junctions are microwave circuit elements which act as dissipationless, non-linear inductors. They are formed by a sandwich structure consisting of two superconducting leads connected by a thin insulating barrier. In this section, we will first give a description of the Josephson junction and then briefly introduce the superconducting transmon qubit.

It is well know that the dissipationless supercurrent through the junction and the voltage across the junction are described by the following relations [75]

$$I = I_0 \sin\phi, \qquad V = \frac{\Phi_0}{2\pi}\dot{\phi}. \tag{2.8}$$

Here I_0 is the critical current, ϕ is the phase difference between the two leads and Φ_0 is the magnetic flux quantum $h/2e$. The Junction inductance can be expressed using the definition $L = V/\dot{I}$,

$$L_J = L_{J0}/\cos\phi = L_{J0}/\sqrt{I - (I/I_0)^2}, \tag{2.9}$$

where we define $L_{J0} \equiv \Phi_0/2\pi I_0$. Therefore, the inductance of Josephson junction is related to the current flowing through the junction. This nonlinear response of the inductance to the current can be used to make an anharmonic oscillator. Thus by taking advantage of the anharmonicity in this oscillator, we now are able to distinguish individual transition and choose the lowest two levels as the qubit.

In addition, if the junction is biased with a voltage V, we can see that the current will oscillate in the following way based on the Eq. (2.8) [76],

$$I = I_0 \sin(\phi_0 + 2\pi V t/\Phi_0). \tag{2.10}$$

We can also make a tunable Josephson inductance with SQUID (Superconducting QUantum Interference Device) loop which consists of two Josephson junctions [77]. The critical current I_c of the SQUID can be expressed as a function of the magnetic flux Φ_{ext} from the external magnetic field

$$I_c = 2I_0|\cos(\pi\Phi_{ext}/\Phi_0)|. \tag{2.11}$$

Next, we give a quantum description of an isolated Josephson junction in terms of Cooper pair number, N, in order to better understand the behavior of Josephson junction in a microscopic way. This description follows references [65, 78, 79]. We define the Cooper pair number operator $\hat{N}$ with its eigenstate $|N\rangle$ which represents the number of Cooper pairs on one side of superconducting lead of the junction. We can also have the conjugate operator $\hat{\phi}$ with its eigenstate $|\phi\rangle$ which represents the phase difference between the two leads.

Here we define

$$|\phi\rangle = \sum_{N=-\infty}^{\infty} e^{iN\phi}|N\rangle, \tag{2.12}$$

and its inverse relation

$$|N\rangle = \frac{1}{2\pi}\int_0^{2\pi} e^{-iN\phi}|\phi\rangle d\phi. \tag{2.13}$$

We can easily verify that $\langle N|M\rangle = \delta_{NM}$ and $\langle\phi|\phi'\rangle = 2\pi\delta(\phi-\phi')$, where $\delta_{NM} = \frac{1}{2\pi}\int_0^{2\pi} e^{-i(N-M)\phi}d\phi$ and $\delta(\phi-\phi') = \frac{1}{2\pi}\sum_{N=-\infty}^{\infty} e^{-iN(\phi-\phi')}$.

We can use the identity relation $I = \frac{1}{2\pi}\int_0^{2\pi}|\phi'\rangle\langle\phi'|d\phi'$ and then define,

$$e^{i\hat{\phi}} = \frac{1}{2\pi}\int_0^{2\pi} e^{i\phi'}|\phi'\rangle\langle\phi'|d\phi'. \tag{2.14}$$

Therefore, we have $e^{i\hat{\phi}}|\phi\rangle = e^{i\phi}|\phi\rangle$ and $e^{i\hat{\phi}}|N\rangle = |N-1\rangle$ [65, 78, 79]. From the above equation we can express the operator $e^{i\hat{\phi}}$ in terms of the Cooper pair number state $|N\rangle$,

$$e^{i\hat{\phi}} = \sum_{N=-\infty}^{\infty}|N-1\rangle\langle N|, \qquad e^{-i\hat{\phi}} = \sum_{N=-\infty}^{\infty}|N\rangle\langle N-1|. \tag{2.15}$$

Next, we should obtain the Hamiltonian of the isolated Josephson junction which is determined by the Cooper pair tunneling. For example, if there is one Cooper pair tunneling through the barrier from one superconducting lead to the other, then the number of Cooper pairs will decrease by one on one side while increase by one on the other side correspondingly. This tunneling can be described by the operator $|N\rangle\langle N+1|$, and we may have $H_J \backsim \sum_{N=-\infty}^{\infty}|N\rangle\langle N+1|$ by considering all the possible number states. Since the Hamiltonian has to be Hermitian in this case, we may write the Hamiltonian for the isolated Josephson junction in the following from,

$$H_J = -\frac{E_J}{2}\sum_{N=-\infty}^{\infty}|N\rangle\langle N+1| + |N+1\rangle\langle N|. \tag{2.16}$$

If we use the phase operator in Eq (2.15), the above Hamiltonian can be rewritten

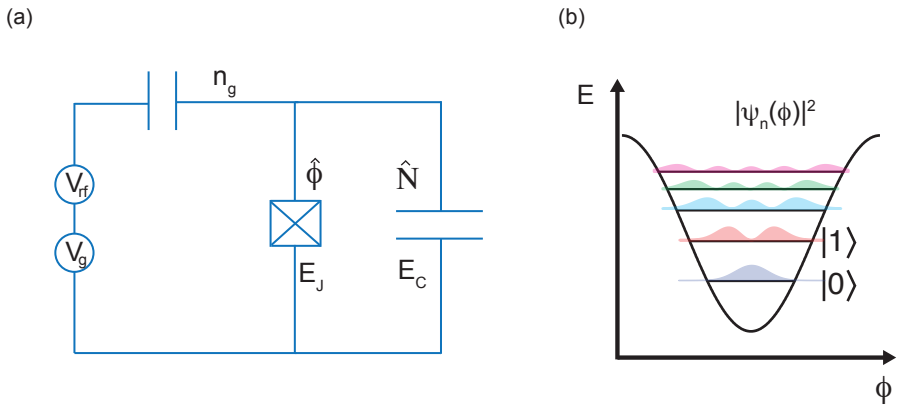

Figure 2.3: The transmon qubit. (a) Circuit schematic for a transmon qubit which is comprised of a Josephson junction characterized by the Josephson energy E_J and a shunted capaciter with energy E_C. It is coupled to an eternal voltage V_g and a RF source V_{rf}. (b) Energy levels and wavefunctions of a cosinusoidal potential.

as

$$H_J = -\frac{E_J}{2}[e^{i\hat{\phi}} + e^{-i\hat{\phi}}] = -E_J \cos\hat{\phi}. \tag{2.17}$$

Therefore, the Josephson junction has a sinusoidal potential energy which provides the non-linearity for the superconducting qubits which we will describe below.

The circuit of a superconducting transmon qubit is comprised of a Josephson junction shunted by a capacitor as displayed in Fig. 2.3, and its Hamiltonian can be written as [80]

$$\hat{H}_q = 4E_c(\hat{N} - n_g)^2 - E_J \cos\hat{\phi}, \tag{2.18}$$

where $E_J = \hbar I_c/2e$ and $E_c = e^2/2C$ are the Josephson energy and charging energy, I_c is the critical current of the Josephson junction and C is the total shunting capacitance. $\hat{N}$ and $\hat{\phi}$ satify the commutation relation, $[\hat{\phi}, \hat{N}] = i$. The above Hamiltonian can be solved exactly in phase representation,

$$[-4E_C(\frac{\partial}{\partial\phi} - n_g)^2 - E_J\cos(\hat{\phi})]\psi(\phi) = E\psi(\phi), \tag{2.19}$$

We use $\hat{N} = -i\frac{\partial}{\partial\phi}$ and obtain the eigenenergies and eigenwavefunctions characterized

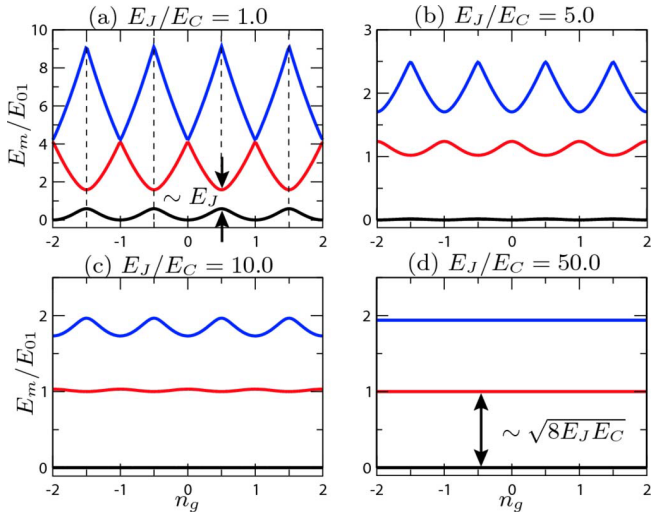

Figure 2.4: Energy structure of superconducting qubits. When $\frac{E_J}{E_C}$ is small, the transition energies are very sensitive to the charge noise which degrades the coherence times. As $\frac{E_J}{E_C}$ increases, we go into a regime where the energy levels are insensitive to the charge noise. Adapted from ref. [82].

by E_J and E_C in terms of Mathieu functions [81–83],

$$E_n = E_C \mathcal{M}_A(\mu_n, -\frac{E_J}{2E_C}), \tag{2.20}$$

$$\psi_n(\phi) = \frac{1}{\sqrt{2\pi}}[\mathcal{M}_C(\frac{E_n}{E_C}, -\frac{E_J}{2E_C}, \frac{\phi}{2}) - i^{2n+1}\mathcal{M}_S(\frac{E_n}{E_C}, -\frac{E_J}{2E_C}, \frac{\phi}{2})], \tag{2.21}$$

where $\mathcal{M}_A$, $\mathcal{M}_C$, $\mathcal{M}_S$ are the Mathieu characteristic value, the even Mathieu function, odd Mathieu function respectively and $\mu_n = (-1)^{n+1} + [n \mod 2]$ are the indexes for the eigenenergies.

As we can see from the Eq. (2.20), the eigenvalues of the qubit depend on the ratio of $\frac{E_J}{E_C}$ thus this value determines which type of qubit the circuit represents. For example, when $\frac{E_J}{E_C} \approx 1$, the circuit can represent a Cooper pair box qubit which is very sensitive to the charge noise since the energy levels depend on charge which tends to fluctuate (Fig. 2.4(a) [82]). As $\frac{E_J}{E_C}$ increases, the energy levels are less dependent on the charge noise. But if $\frac{E_J}{E_C} \approx 50$ we reach in a region where the charge noise is greatly suppressed such that the qubit is insensitive to the charge noise as illustrated

in Fig. 2.4. In the region, the qubit is the so-called transmon qubit. The frequency of the transmon qubit is determined by the value of E_J and E_C, $\omega_q/2\pi = \sqrt{8E_JE_C} - E_C$. The anharmonicity of the transmon qubit $\alpha \approx -E_C$ which is the energy difference between the lowest two energy levels. With such anharmonicity, we can realize a qubit with the lowest two energy levels and perform fast gate operations. For a transmon qubit, typically, we have $\omega_q \approx 5$ GHz and $\frac{E_J}{E_C} \approx 50$ which would require $E_J \approx 12.5$ GHz and $E_C \approx 250$ MHz. It is worth mentioning that we sacrifice the anharmonicity in order to suppress the charge noise to get decent relaxation times in transmon qubit which to some extent limits the readout fidelity from the high level transitions and degrade fast gate operations [84]. Recently, the MIT group led by W. Oliver fabricated flux qubits with much larger anharmonicity but have similar relaxation times compared to transmon qubit, which might be a better candidate for the purpose of quantum computing [85].

2.3 Circuit QED

In 2012, Serge Haroche and David Wineland won the Nobel prize "for ground breaking experimental methods that enable measuring and manipulation of individual quantum systems". One challenge for measuring a quantum system is that the state of a quantum system is very sensitive to its surrounding noise which makes it very fragile, and thus hard to observe experimentally. On the one hand, we desire a quantum system that is highly isolated from the surrounding noise. One the other hand, we have to be able to control the quantum system and measure it which effectively makes it open to the environment [86–90]. Therefore, we need to develop a method which can eliminate the noise channels that we don't want and keep the channels that are used for controlling and measuring the quantum system. Cavity quantum electrodynamics (QED) or circuit QED satisfies the requirement above and provides us the method to study the interaction between light and matter [91–94]. The cavity or circuit QED system generally consists of three components as illustrated in Fig 2.5: a quantum system whose properties are to be measured, the pointer system (probe) which is the

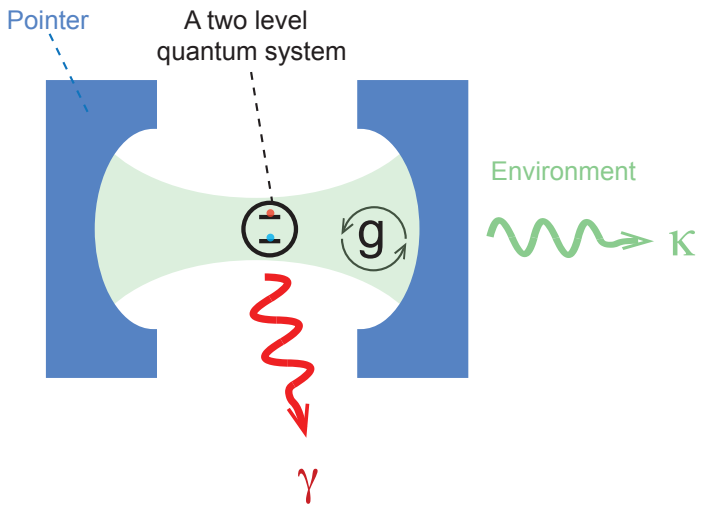

Figure 2.5: Schematic of cavity QED. A qubit interacts with the electromagnetic field in a cavity with a strength g. The qubit relaxes at a rate γ and the cavity decays at a rate κ.

measuring apparatus coupled with the quantum system, and the environment which causes the decoherence of the quantum system. The purpose of this section is to given an overview on the measuring principles in circuit QED.

2.3.1 The Jaynes-Cummings Hamiltonian

The Hamiltonian of the circuit QED system is comprised of three terms: a qubit term, H_q, a cavity term, H_c and an interaction term, H_{int}. We can write the total Hamiltonian for the qubit-cavity system [95],

$$\begin{aligned} H &= H_q + H_c + H_{int} \\ &= \tfrac{1}{2}\hbar\omega_q\hat{\sigma_z} + \hbar\omega_c(\hat{a}^\dagger\hat{a} + \tfrac{1}{2}) + \hbar g(\hat{a} + \hat{a}^\dagger)(\hat{\sigma}_+ + \hat{\sigma}_-), \end{aligned} \tag{2.22}$$

where ω_q is the qubit frequency, g is the coupling strength between the qubit and the cavity, $\hat{\sigma}_+$ and $\hat{\sigma}_-$ are the qubit raising and lowering operators given by $\frac{1}{2}(\hat{\sigma}_x \pm i\hat{\sigma}_y)$. We can simplify the above Hamiltonian by ignoring the terms in the interaction part that don't conserve energy using the rotating wave approximation, we then obtain

the Jaynes-Cummings Hamiltonian [96],

$$H_{JC} = \frac{1}{2}\hbar\omega_q\hat{\sigma_z} + \hbar\omega_c(\hat{a}^\dagger\hat{a} + \frac{1}{2}) + \hbar g(\hat{a}\hat{\sigma}_+ + \hat{a}^\dagger\hat{\sigma}_-). \tag{2.23}$$

We can diagonalize the JC Hamiltonian to obtain its eigenvalues [97],

$$E_{\pm,n} = \hbar n\omega_c \pm \frac{\hbar}{2}\sqrt{4ng^2 + \Delta^2}, \tag{2.24}$$

and eigenstates,

$$\begin{aligned} \psi_n(+) &= \sin\theta_n|g,n\rangle + \cos\theta_n|e,n-1\rangle, \\ \psi_n(-) &= \cos\theta_n|g,n\rangle - \sin\theta_n|e,n-1\rangle, \\ \theta_n &= \tfrac{1}{2}\arctan(\tfrac{2g\sqrt{n}}{\Delta}), \end{aligned} \tag{2.25}$$

where n is the total number of excitations in the qubit-cavity system and $\pm$ represent the higher energy and lower energy state in the n excitation mode, $\Delta = \omega_q - \omega_c$ is the detuning between the qubit and the cavity.

2.3.2 Dispersive measurement

In this section, we will discuss the situation when the qubit is far detuned from the cavity compared to the coupling strength, $\Delta \gg g$, such that there is no energy exchange but still an interaction between the qubit and cavity. In such a situation, the fact that the cavity's resonance depends on the state of the qubit can be used as an indirect measurement to probe the state of the qubit via a measurement of the cavity field.

Here we define a small parameter $\lambda = \frac{g}{\Delta}$ and apply a unitary transformation, $D = e^{\lambda X}$ and $X = (\hat{a}\hat{\sigma}_+ + \hat{a}^\dagger\hat{\sigma}_-)$, to the Eq. (2.22). Then we use the Baker-Hausdorf expansion [65, 98],

$$D^\dagger H_{JC} D = H_{JC} + \lambda[X, H_{JC}] + \frac{1}{2}\lambda^2[X,[X,H_{JC}]] + ... + \frac{1}{n!}\lambda^n[X,[X,[X,...[X,H_{JC}]]]...], \tag{2.26}$$

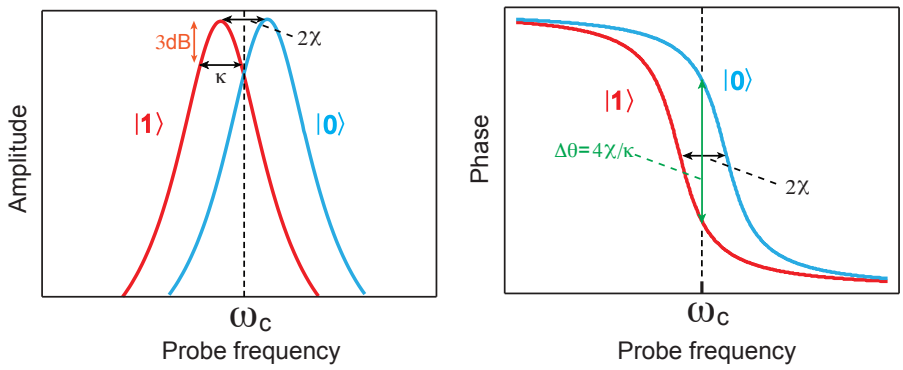

Figure 2.6: Qubit state-dependent phase shift. The cavity resonance shifts an amount 2χ when the qubit jumps from $|1\rangle$ to $|0\rangle$ or vice versa in the dispersive regime. The cavity phase responds differently when the qubit is in the ground state $|0\rangle$ (Blue curve) and excited state $|1\rangle$ (red curve). If the cavity is probed at a frequency ω_c, the phase difference for $|0\rangle$ and $|1\rangle$ is $\Delta\theta = 4\chi/\kappa$.

to expand the Jaynes-Cummings Hamiltonian H_{JC} to the second order in λ and obtain [99, 100],

$$H_{disp} = \frac{1}{2}\hbar\omega_q\hat{\sigma}_z + \hbar\omega_c(\hat{a}^\dagger\hat{a} + \frac{1}{2}) + \hbar\frac{g^2}{\Delta}\hat{a}^\dagger\hat{a}\hat{\sigma}_z + \frac{1}{2}\hbar\frac{g^2}{\Delta}\hat{\sigma}_z. \tag{2.27}$$

The above Hamiltonian allows us to perform a QND measurement of the qubit state in the energy basis ($\hat{\sigma}_z$) using the cavity as a probe since $[H_{dis}, \hat{\sigma}_z] = 0$ [68, 101, 102]. We can also rewrite the Hamilton H_{disp} in the following form

$$H_{disp} = \frac{1}{2}\hbar\omega_q\hat{\sigma}_z + \hbar(\omega_c + \frac{g^2}{\Delta}\hat{\sigma}_z)(\hat{a}^\dagger\hat{a} + \frac{1}{2}), \tag{2.28}$$

then we can find that the cavity resonance frequency depends on the state of the qubit ($\hat{\sigma}_z$) which will enable us to probe the cavity frequency to infer the state of the qubit as illustrated in Fig. 2.6. The cavity resonance shifts an amount 2χ when the qubit switches from the $|0\rangle$ to $|1\rangle$ which is given by

$$\chi = \frac{g^2}{\Delta} = \frac{1}{2}(\omega_c(|0\rangle) - \omega_c(|1\rangle)) = \frac{1}{2\hbar}[(E_{n+1,|1\rangle} - E_{n,|1\rangle}) - (E_{n+1,|0\rangle} - E_{n,|0\rangle})] \tag{2.29}$$

Please note that the above expression is true in the pure qubit case (two levels) but

is only an approximation for the transmon, where higher energy levels come to play [103–105].

If we rearrange the terms in Eq. (2.22) in another way and obtain

$$H_{disp} = \frac{1}{2}\hbar(\omega_q + \frac{g^2}{\Delta} + \frac{2g^2}{\Delta}\hat{a}^\dagger\hat{a})\hat{\sigma}_z + \hbar\omega_c(\hat{a}^\dagger\hat{a} + \frac{1}{2}). \tag{2.30}$$

The above equation shows that the qubit frequency is shifted by the photons in the cavity. This is the ac Stark effect which can be used to calibrate the average photon number $\bar{n} = \langle\hat{a}^\dagger\hat{a}\rangle$ in the cavity for a given readout power. In experiments, χ is determined by measuring ac Stark shift.

2.3.3 Phase sensitive amplification

In this section, we briefly discuss the working principle of phase sensitive amplifiers in which the output signal depends on the phase of the pump. The description in this section follows reference [106]. For more rigorous and detailed description, please refer to the Refs. [45, 105–107].

As we introduced in the Chapter 1, the JPA is a weakly nonlinear resonator and its schematic is similar to the transmon qubit but with much smaller nonlinearity. The Hamiltonian that describes the JPA can be given by

$$H_{JPA} = \hbar\omega_r\hat{A}^\dagger\hat{A} + \hbar\frac{K}{2}(\hat{A}^\dagger)^2(\hat{A})^2, \tag{2.31}$$

where A is the annihilation operator for the resonator field with resonant frequency ω_r and K is the Kerr nonlinearity.

Based on the input-output model which is illustrated in Fig. 2.7 and the above Hamiltonian, we obtain the equation of motion for the resonator field [106],

$$\dot{\hat{A}} = -i\omega_r\hat{A} - iKA^\dagger\hat{A}\hat{A} - \frac{\kappa+\gamma}{2}\hat{A} + \sqrt{\kappa}\hat{A}_{in}(t) + \sqrt{\gamma}\hat{b}_{in}(t), \tag{2.32}$$

The field modes can be written as the sum of a classical part associated with paramp pump (α, α_{in}, α_{out}) and a quantum part of quantum signal of our interest

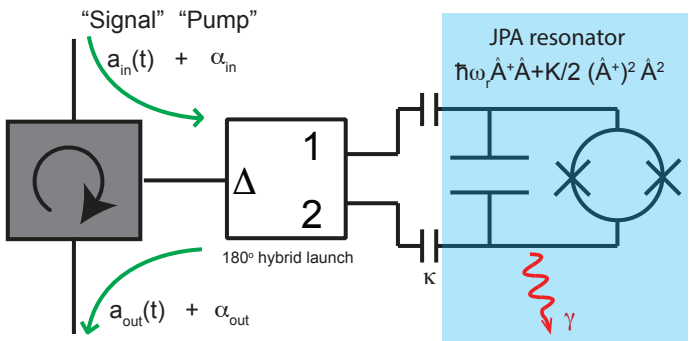

Figure 2.7: Input and output model for Josephson parametric amplifier. The JPA is capacitively coupled to the transmission through a microwave hybrid with a rate κ. The loss of JPA to the environment, $\hat{b}_{in}$, is characterized by a rate γ.

$(a,\ a_{in},\ a_{out})$,

$$\hat{A}_{in}(t) = (a_{in}(t) + \alpha_{in})e^{-i\omega_p t}, \tag{2.33}$$

$$\hat{A}_{out}(t) = (a_{out}(t) + \alpha_{out})e^{-i\omega_p t}, \tag{2.34}$$

$$\hat{A}(t) = (a(t) + \alpha)e^{-i\omega_p t}. \tag{2.35}$$

Here we assume that the pump power is much larger than the signal, $\langle a_{in}^\dagger a_{in}\rangle \ll |\alpha|^2$, thus we only consider the linear terms in a. With that we obtain the following equation after plugging the Eq. (2.33) into Eq. (2.32) [106],

$$\dot{a} = i(\omega_p - \omega_r - 2K|\alpha|^2 + i\frac{\kappa+\gamma}{2})a(t) - iK\alpha^2 a^\dagger(t) + \sqrt{\kappa}a_{in}(t) + \sqrt{\gamma}b_{in}(t). \tag{2.36}$$

Since the above equation is linear, we can express the solution in its Fourier transformation such as $a(t) = \frac{\kappa+\gamma}{\sqrt{2\pi}}\int_{-\infty}^{\infty} d\Delta e^{-i\Delta(\kappa+\gamma)t}a_\Delta$, $a_{in}(t) = \frac{\kappa+\gamma}{\sqrt{2\pi}}\int_{-\infty}^{\infty} d\Delta e^{-i\Delta(\kappa+\gamma)t}a_{in,\Delta}$ and $b_{in}(t) = \frac{\kappa+\gamma}{\sqrt{2\pi}}\int_{-\infty}^{\infty} d\Delta e^{-i\Delta(\kappa+\gamma)t}b_{in,\Delta}$, here Δ is the detuning between the signal frequency and the pump frequency. After plugging these into the Eq. (2.32) and using the input and output formalism, $A_{out}(t) = \sqrt{\kappa}A(t) - A_{in}(t)$ [108], we have,

$$a_{out,\Delta} \approx \sqrt{G}a_{in,\Delta} + e^{i\delta}\sqrt{G-1}a_{in,-\Delta}^\dagger, \tag{2.37}$$

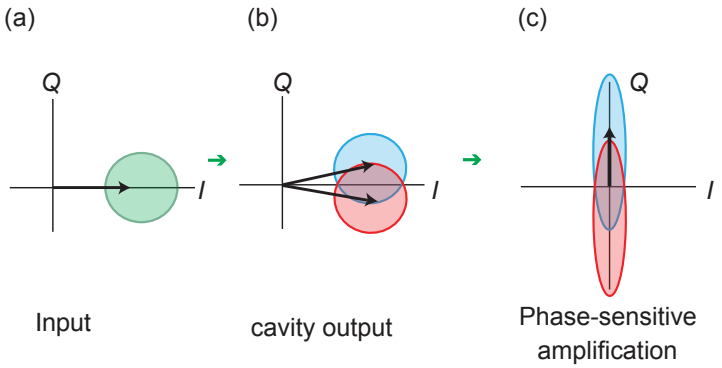

Figure 2.8: Dispersive measurement. (a) The cavity is probed with a coherent input microwave tone at a frequency ω_r. (b) After reflecting off the cavity, the output tone acquires a qubit-state-dependent phase shift. (c) A specific quadrature is amplified by operating the JPA in a phase sensitive mode.

where G is the power gain which mainly depends on the detuning between the pump and resonance of JPA and drive power of the pump. If G is large enough and $\Delta = 0$, we might have $a_{out,\Delta} \approx \sqrt{G}(a_{in} + e^{i\delta}a_{in}^{\dagger})$, here δ is relative phase between the signal and the pump. Thus it is apparent that the amplified quadrature is related to the phase δ and this process is called phase sensitive amplification.

In this thesis, homodyne detection is employed to measure only one single mode quadrature through mixing the output signal with a strong tone at the same frequency, referred to as the local oscillator (LO). In the microwave domain, we use a commercial mixer that modulates our signal $A\sin(\omega_r t + \phi)$ by a strong carrier $A\cos(\omega_r t + \delta)$ provided by the LO at the same frequency. We obtain the measurement outcome $I\cos\delta + Q\sin\delta$ (here we define $I = A\cos\phi$ and $Q = A\sin\phi$) by averaging out the fast oscillating component at frequency $2\omega_r$. We can adjust the phase δ to determine which quadrature we want to detect after phase sensitive amplification. As displayed in Fig. 2.8, the cavity tone is only amplified along one specific quadrature while de-amplified along the other quadrature before mixing by the LO. This is the so-called squeezing which doesn't add any noise into the measurement signal [20]. For more details for how the parametric amplifier works, there are more detailed discussions in these references [106, 107, 109].

2.4 Realistic measurement

In this section, we will first briefly introduce the theory of positive operator-valued measures (POVMs), which are used to describe a general quantum measurement throughout the whole thesis. We then use the stochastic master equation to describe how we update the state of the quantum system with the measurement signal.

2.4.1 POVMs

A quantum measurement can be described by a set of operators $\{\Omega_m, m \in M\}$, which satisfy $\sum_m \Omega_m^\dagger \Omega_m = I$. Here M is the ensemble of all the possible measurement outcomes. If the system is in the state $|\psi\rangle$, the probability of obtaining the measurement outcome m is $P(m) = \langle\psi|\Omega_m^\dagger\Omega_m|\psi\rangle$, leaving the system in the state $\psi_f = \Omega_m|\psi\rangle/\sqrt{P(m)}$. Equivalently, if the system is described by a density matrix ρ, then the probability for this measurement outcome is $P(m) = \mathrm{Tr}(\Omega_m^\dagger\rho\Omega_m)$ and the state of the system after the measurement is $\rho_f = \Omega_m^\dagger\rho\Omega_m/\mathrm{Tr}[\Omega_m^\dagger\rho\Omega_m]$.

In the work of this thesis, we can define a set of POVMs, Ω_V, to describe the continuous weak measurement with the continuous outcome V. Similarly, the probability for obtaining the outcome V in this weak measurement is expressed by $P(V) = \mathrm{Tr}(\Omega_V^\dagger\rho\Omega_V)$, which is typically the sum of two Gaussian distributions weighted by the state populations for the ground and excited states. We will give detailed discussions in Chapter 5 and Chapter 6.

2.4.2 Measurement of the environment

In real experiments, the measurement process occurs over some finite time scale τ which is determined by the interaction between the quantum system and the probe system. This is characterized by the measurement strength S which can be obtained from the separation of the measurement probability distributions for the ground and excited states (ΔV) and their Gaussian variance (σ^2), $S = \frac{\Delta V^2}{\sigma^2}$ [110]. If the quantum system is weakly coupled to the probe system such that the uncertainty in a single measurement is very large compared with the separation between the eigenvalues

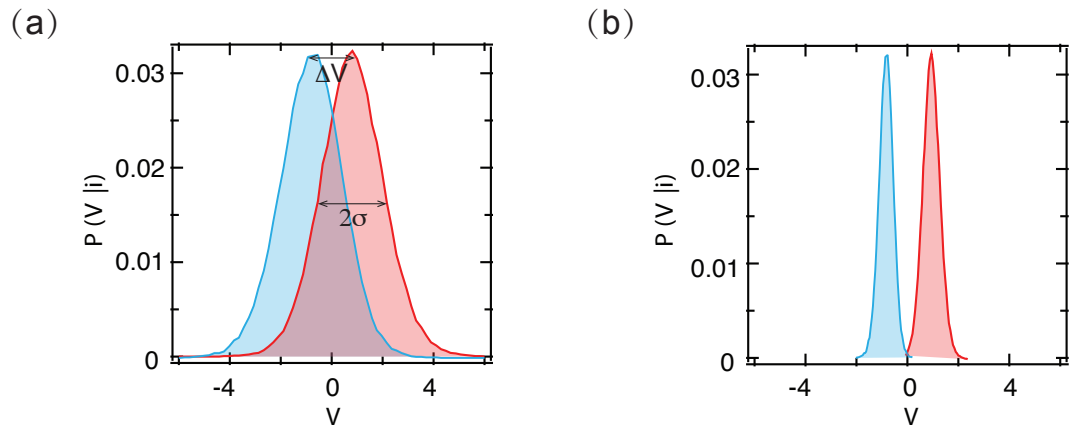

Figure 2.9: Signal distributions for weak and strong measurement. Red: signal probability distribution for excited state, blue: signal probability distribution for ground state.

of the observable, e.g. as illustrated in Fig. 2.9(a). If the probability distributions for the ground and excited state overlap, given a measurements result, it is hard to determine whether it's in the ground or excited state, this result is a so-called weak measurement [111]. The weaker the measurement, the smaller the separation between these two distributions. Hence, only partial information about the quantum system is extracted in weak measurements without collapsing the state of the quantum system, and we can observe how the system evolves under measurement [112]. If we integrate a series of these quantum measurements over time $T \gg \tau$, in this case the two probability distributions for the ground and excited state will be completely separated and it is easy to tell whether the measurement result clearly indicates the ground or excited state as shown in Fig. 2.9(b). If we perform such a measurement, the qubit instantaneously collapses to the ground or excited state (our state of knowledge changes abruptly). This situation corresponds to a strong projective measurement (von Neumann measurements) as we have discussed before. In the following, we shall discuss how we infer the evolution of quantum state with the weak measurement signals by employing quantum trajectory theory in continuous weak measurement.

2.4.3 Stochastic master equation

The effect of the environment is to intermingle states. Thus, in in order to describe the evolution of a system interacting with its environment we must first describe statistical mixture states rather than pure states. The evolution of a quantum system in the pure state $\psi(t)$ at time t is governed by Schödinger's equation. Equivalently, the system can be also described by a density matrix ρ if it is in a mixed state which corresponds to a quantum statistical ensemble. The density matrix ρ at time t_0 can be expressed as:

$$\rho(t_0) = \sum_n P(n)|\psi_n\rangle\langle\psi_n|, \tag{2.38}$$

where $P(n)$ is the weight and $|\psi_n\rangle$ is the wave function that evolves in time based on the Schödinger's equation, $i\hbar\frac{d}{dt}|\psi_n(t)\rangle = H(t)|\psi_n(t)\rangle$. For example, the state $|\psi_i\rangle$ in equation (2.2) is equivalent to the density matrix $\rho_i(t_0) = \begin{pmatrix} \frac{1}{2} & \frac{1}{2} \\ \frac{1}{2} & \frac{1}{2} \end{pmatrix}$.

The state of the system at time t is given by,

$$\rho(t) = U(t, t_0)\rho(t_0)U^+(t, t_0), \tag{2.39}$$

where $U(t, t_0)$ is the time-evolution operator which is determined by the Hamiltonian of the quantum system. If we differentiate this equation with respect to time and then plug into the Schödinger's equation, we can have the equation of motion for the density matrix $\rho(t)$,

$$\frac{d}{dt}\rho(t) = -i[H(t), \rho(t)]. \tag{2.40}$$

The evolution of a closed or isolated quantum system can be described by the above equation which is known as the Liouville-von Neumann equation.

A quantum system only undergoing unitary evolution is a closed system which does not interact with the environment, while manipulation or control of the quantum system makes it an open system. The dynamics of an open quantum system is well

described by the Lindblad master equation [113, 114],

$$\frac{d}{dt}\rho(t) = \mathcal{L}\rho = -i[H, \rho(t)] + \sum_{k=1}^{K} \mathcal{D}[L_k]\rho(t), \tag{2.41}$$

where H is the Hamiltonian, L_k is Lindblad operator describing the dissipative coupling to the evironment and $\mathcal{D}[L_k] = \{L_k \rho_t L_k^\dagger - \frac{1}{2} L_k^\dagger L_k, \rho_t\}$ is the dissipation superoperator.

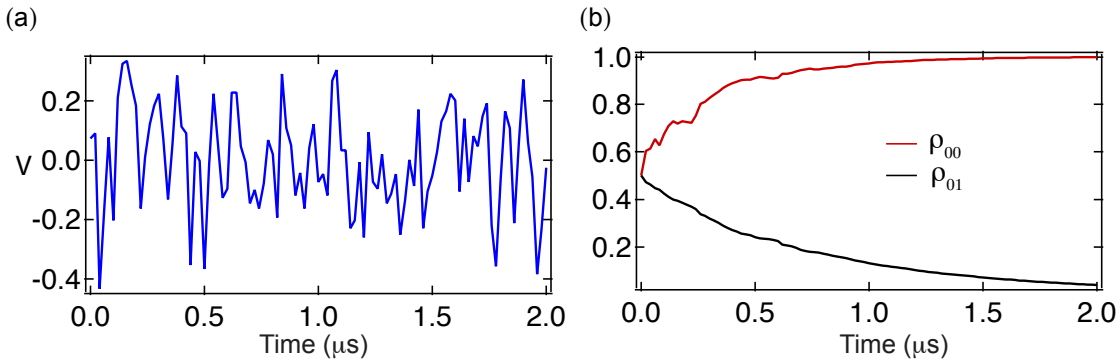

Figure 2.10: How to calculate the density matrix ρ. (a) The measured quantum noise $V(t)$ as a function of time t using homodyne measurement. (b) The inferred density matrix components from $V(t)$ by employing the Eq. (2.41).

If the system is subject to a continuous measurement, the evolution of the density matrix $\rho(t)$ conditioned on the measurement outcomes before time t is given by the stochastic master equation in Itô form [113]:

$$\frac{d}{dt}\rho(t) = \mathcal{L}\rho = -i[H, \rho(t)] + \sum_{k=1}^{K} \mathcal{D}[L_k]\rho(t) + \sqrt{\eta}(c\rho(t) + \rho(t)c^\dagger)V(t), \tag{2.42}$$

where c is the measurement observable, η is the measurement quantum efficiency and $V(t)$ is the random noisy measurement signal at time t with mean value $\sqrt{\eta}Tr((c + c^\dagger)\rho(t))dt$ and variance $\sigma^2 = dt$. As displayed in Fig. 2.10(a), the measurement signal $V(t)$ reflects the quantum fluctuations of the measured electromagnetic mode which contain qubit state information. By plugging the measurement signal into the above equation, we can obtain the components of the density matrix as illustrated in Fig.

2.10(b) with the initial state $|+x\rangle$. Therefore, we can use the above stochastic master equation with the continuous weak measurement signal to obtain quantum trajectories and explore interesting problems in quantum foundations. Note that by averaging many runs of the trajectories inferred from the Eq. (2.42), we can recover the deterministic trajectory calculated from the Eq. (2.41).

2.5 Quantum smoothing

In this section, we discuss how we apply quantum smoothing to a monitored quantum system with quantum measurement. We first illustrate the idea of how the further probing after time t affects the probability for the outcome of the measurement Ω_m at time t. A more rigorous description of the Past Quantum State formalism is presented in reference [50].

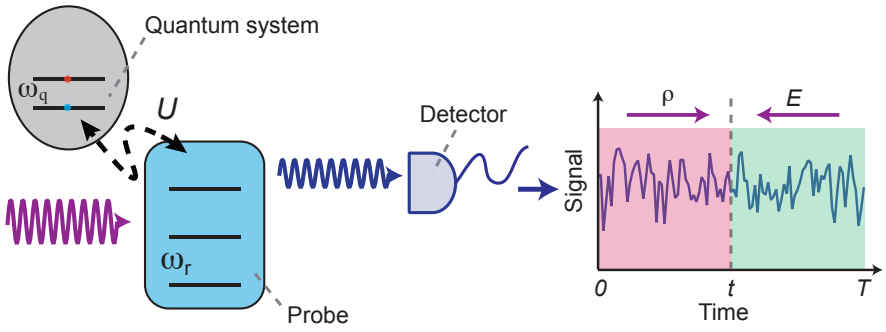

Figure 2.11: Schematic of the quantum measurement on the system-probe state characterized by a a unitary interaction U. The density matrix ρ depends on the measurement signal before time t and the effect matrix E depends on the measurement signal after time t.

As illustrated in the Fig. 2.11, we have a quantum system which is prepared in state $|\psi_0\rangle$, we then perform a first measurement M_1 which gives the outcome of m_1. We have a new state $M_1|\psi_0\rangle$ after the measurement. The probability of getting the outcome m_1 is $P(m_1) = \langle\psi_0|M_1^\dagger M_1|\psi_0\rangle = ||M_1|\psi_0\rangle||^2$ which is simply Born's rule. If we do a second measurement M_2 with the measurement outcome m_2, we have to apply the corresponding operator M_2 acting on the state $M_1|\psi_0\rangle$

after the first measurement to get the state $M_2M_1|\psi_0\rangle$. We then obtain the joint probability of getting these two measurement outcomes m_1 and m_2, $P(m_1, m_2) = ||M_2M_1|\psi_0\rangle||^2$. This probability is the square of the norm of the state $M_2M_1|\psi_0\rangle$ which is obtained by acting on the initial state with the first measurement operator M_1 and then M_2. In experiments, we can measure the system continuously in time thus we can do a series of the measurements. We can perform n measurements on the quantum system and will obtain a series of outcomes from m_1 to m_n, the state evolution goes from the initial state $|\psi_0\rangle$ to a final state $M_n...M_t...M_2M_1|\psi_0\rangle$ which is obtained by applying the operators M_1, M_2 ..., M_t, M_n to the initial state $|\psi_0\rangle$. Thus the state evolves as function of time which is a random trajectory conditioned on the measurement outcomes. The joint probability of these outcomes is given by this formula, $P(m_1, m_2, ..., m_t, ..., m_n) = ||M_n...M_t...M_2M_1|\psi_0\rangle||^2$. Up to now, we know how to obtain the probability of getting the measurement outcomes at time t, simply by acting on the measurement operators from M_1 up to M_t which is $P(m_1, m_2, ..., m_t) = ||M_t...M_2M_1|\psi_0\rangle||^2$ as discussed above. But in this thesis, we are interested to keep measuring the quantum system after time t and want to ask how the further probing affects this probability for the measurement outcome at time t? At time t, we use a measurement Ω_m to replace the M_t for clarity. The conditioned probability of getting the measurement outcome m with measurements before and after time t can be expressed in the following way, $P_C(m) \sim ||M_n...\Omega_m...M_2M_1|\psi_0\rangle||^2$. Therefore, we can obtain the probability of getting result m from Ω_m at time t and then an ensuring set of measurements $M_{t+1}...M_n$ from further probing after time t.

$$P_C(m) = ||M_n...\Omega_m...M_2M_1|\psi_0\rangle||^2 / \sum_m ||M_n...\Omega_m...M_2M_1|\psi_0\rangle||^2 \tag{2.43}$$

However, the quantum state is generally not pure, thus it has to be described by a density matrix ρ_0. The state evolves after the first measurement M_1 with outcome m_1 in such way, $\rho_0 \to M_1\rho_0M_1^\dagger$. The probability of getting the outcome m_1 is $P(m_1) = \mathrm{Tr}(M_1\rho_0M_1^\dagger)$. If we do a series of these measurements, the conditioned probability of

getting the measurement outcome m at time t is given by

$$P_C(m) \sim \mathrm{Tr}(M_n...M_{t+1}\Omega_m M_{t-1}...M_2M_1\rho_0 M_1^\dagger M_2^\dagger...M_{t-1}^\dagger \Omega_m^\dagger M_{t+1}^\dagger...M_n^\dagger). \tag{2.44}$$

Due to the cyclic property of the trace, we can remove the $M_n...M_{t+1}$ from the left to the right and then we have

$$P_C(m) \sim \mathrm{Tr}(\Omega_m \underbrace{M_{t-1}...M_2M_1\rho_0 M_1^\dagger M_2^\dagger...M_{t-1}^\dagger}_{\rho} \Omega_m^\dagger \underbrace{M_{t+1}^\dagger...M_n^\dagger I M_n...M_{t+1}}_{E}). \tag{2.45}$$

We can denote this part $M_{t-1}...M_2M_1\rho_0 M_1^\dagger M_2^\dagger...M_{t-1}^\dagger$ in $P_C(m)$ as ρ which is a normal quantum trajectory conditioned on the measurement outcomes. This piece $M_{t+1}^\dagger...M_n^\dagger I M_n^\dagger...M_{t+1}^\dagger$ is from the further probing and called E which is a backwards trajectory that starting with the identity matrix I. Thus we obtained the formalism for the smoothed probability of getting the measurement outcome m at time t which is conditioned on both ρ and E,

$$P_P(m) = \frac{\mathrm{Tr}(\Omega_m \rho \Omega_m^\dagger E)}{\sum_m \mathrm{Tr}(\Omega_m \rho \Omega_m^\dagger E)}. \tag{2.46}$$

This is the retrodicted probability conditioned on the density matrix ρ and the effect matrix E which can make a better prediction for measurement outcome m of a general quantum measurement with further information obtained after the measurement at time t. Therefore it is reasonable that $\Xi = (\rho, E)$ plays the role of a quantum state and hence we call it "Past Quantum State". In this thesis, we consider the quantum state as our knowledge — a tool which is used to make predictions for measurement outcomes. Note that the density matrix ρ makes the best prediction for any measurement that could be performed at time t. Here we ask how these predictions change when conditioned on further probing results? We have shown that the measurement probability can be calculated by including another matrix E and will find that the combination of ρ and E makes more confident but still correct predictions. Also note that ρ and E are still independent of the measurement at time t.

Chapter 3

Quantum smoothing for classical mixtures

Quantum states can be usually described by a density matrix $\rho(t)$ rather than a wavefunction $|\psi\rangle$ because the state is not generally pure. If the density matrix $\rho(t)$ evolves without any coherence, it is always diagonal in a definite eigenbasis $\{|n\rangle\}$, thus the system described by the diagonal density matrix can be considered as a classical mixture since it can only be in an incoherent mixture of the eigenstates. Predictions about the outcome of a projective measurement of the system in the eigenstate are given by $P(n) = \rho_{nn}$. This prediction is the same as if the system was actually prepared in one of the eigenstates with these probabilities, which can be explained by a simple hidden variable model. Moreover, for any general measurement M described by a positive-operator-valued measure (POVM) [67, 113, 116] with operators Ω_m that satisfy the identity relation $\sum_m \Omega_m^\dagger \Omega_m = I$, the probabilities of the measurement M with outcome m are given by $P(m) = \mathrm{Tr}(\Omega_m \rho \Omega_m^\dagger)$ which equal the weighted mean of the probabilities over a classical mixture of states $|n\rangle$,

$$P^{cm}(m) = \sum_n P(n) \mathrm{Tr}\big(\Omega_m \rho_n \Omega_m^\dagger\big), \tag{3.1}$$

where $\rho_n = |n\rangle\langle n|$, and the $P^{cm}(m)$ superscript means "classical mixtures ". If the quantum system is continuously monitored after the measurement M then we have

access to further information which can be represented by the effect matrix $E(t)$ as discussed in the previous chapter [50]. We can constrain the diagonality of this effect matrix by taking advantage of the evolution dynamics and measurement, just like with the density operator. We then have the opportunity to ask (at a later time T) what was the probability of obtaining outcome m in the earlier measurement at time t? When applied to such incoherent mixtures, the Past Quantum State (PQS) theory has been overlooked because it seems to give the same result as the classical mixture interpretation that the system merely populated one of its corresponding eigenstates with a certain probability. The goal of this project is to experimentally test the PQS theory to see if the result is the same as the classical mixture interpretation when it is applied to such classical mixtures. Surprisingly, with further probing on a quantum system, we will see that the predictions for the outcome of some measurement made by the PQS theory is clearly in disagreement with the predictions made by the classical mixture interpretation. This chapter describes the work published in D. Tan et al. Phys. Rev. A **94**, 050102(R)(2016).

3.1 A quantum smoothing example

In the following section, it is helpful to start with a simplified picture to introduce our experiment. Illustrated in Fig. 3.1, we consider a cluster of electron spins at time $t_0 = 0$ which is prepared in a mixed state described by a diagonal density matrix $\rho(t_0) = \left(\begin{smallmatrix} \rho_{00} & 0 \\ 0 & \rho_{11} \end{smallmatrix}\right)$, where spins are either up or down. At time t, we performed a test measurement M after the preparation. The measurement M can be described by the POVM operator $\Omega_\uparrow$ or $\Omega_\downarrow$. Here $\uparrow$ or $\downarrow$ is the outcome of the measurement M. The prediction for the outcome of the measurement described by $\Omega_\uparrow$ or $\Omega_\downarrow$ on the system is $P_\uparrow = \mathrm{Tr}(\Omega_\uparrow \rho(t_0) \Omega_\uparrow^\dagger) = \rho_{00}$ ($P_\downarrow = \mathrm{Tr}(\Omega_\downarrow \rho(t_0) \Omega_\downarrow^\dagger) = \rho_{11}$) which is the same as if the system were actually prepared in one of the eigenstates $|n\rangle (n = \uparrow, \downarrow)$ with these probabilities $P_{\uparrow(\downarrow)}$. It looks like the n had an unknown "true value "which could be revealed by the experiment.

Moreover, we can also measure whether the system is up or down along some axis

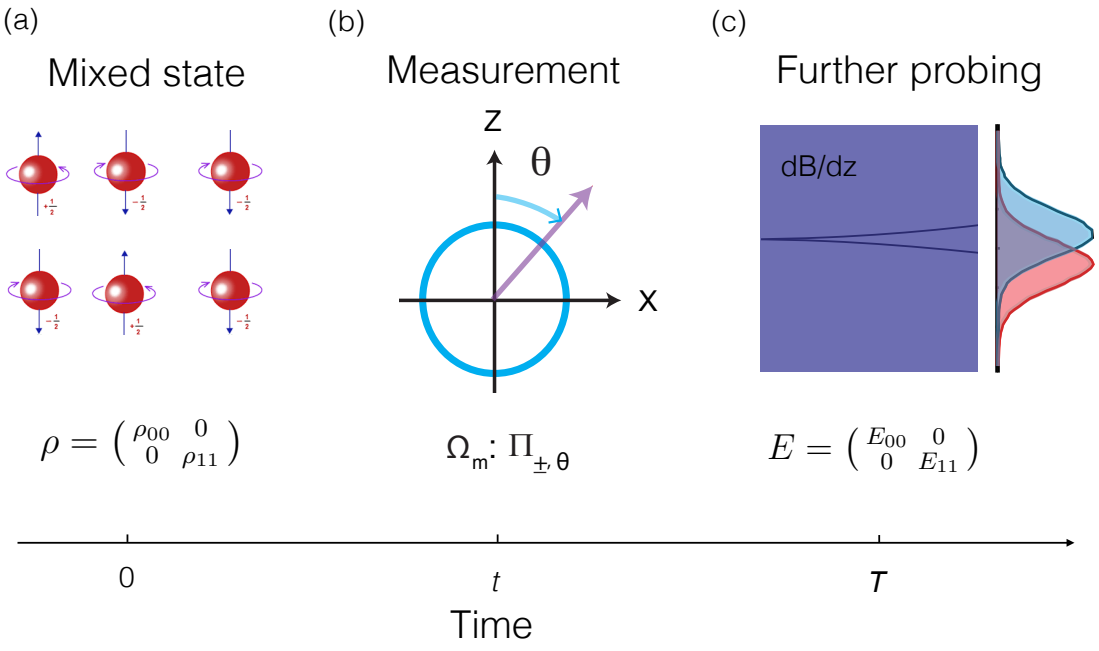

Figure 3.1: A test measurement example to show how we use further probing after the measurement M at time t to refine the prediction for the outcome of the measurement on the system initially prepared in a mixed state at time $t_0 = 0$ in the case of diagonal matrices $\rho(t)$ and $E(t)$. (a) A classical mixture state described by a diagonal density matrix ρ. (b) A measurement is performed at time t. (c) The system is subject to further probing to determine the effect matrix E, e.g. a Stern-Gerlach apparatus.

θ shown in Fig. 3.1 which can be described by the POVM operator $\Pi_{\pm\theta}$ corresponding to finding the spin up or down along axis θ. Then the prediction for the outcome of the measurement $P(\theta, \pm) = \mathrm{Tr}(\Pi_{\pm\theta}\rho(t_0)\Pi^\dagger_{\pm\theta})$ which is equivalent to the weighted probabilities $P^{cm}(\theta, \pm) = \sum_n P(n)\mathrm{Tr}(\Pi_{\pm\theta}|n\rangle\langle n|\Pi^\dagger_{\pm\theta})$ since $\rho(t_0)$ is diagonal in this case, where n is the measurement outcome in the eigenbasis $\{|n\rangle\}$. The prediction $P(\theta, \pm)$ made by the POVM theory is always true while the weighted probability $P^{cm}(\theta, \pm)$ is only true when $\rho(t_0)$ is diagonal. Therefore, we can treat the diagonal $\rho(t_0)$ as a classical mixture. Up to now, we have shown that we cannot rule out a hidden variable model — that the state described by some unknown true state n — based on a diagonal density matrix $\rho(t_0)$ since the predictions made by the quantum mechanics and the hidden variable model (P^{cm}) are the same.

The purpose of this project is to look at further probing to see how it refines the prediction and changes the story of the classical mixture interpretation. After

some measurement M is made at time t, we are able to continuously measure the quantum system to obtain the probability that the spin is up or down which allows us to refine our prediction in hindsight. Where the density matrix $\rho(t)$ records the initial probability of the system, the effect matrix $E(t)$ tells us the probability of the outcome in further probing. The effect matrix $E(t)$ can also be diagonal in this case. The question is whether we we can still treat both diagonal $\rho(t)$ and diagonal $E(t)$ as classical mixtures just like the way we treat a diagonal $\rho(t)$. The answer is "no, we cannot." In the following sections, we will first discuss the theory of the Past Quantum State(PQS) and then show our experimental results.

3.2 The theory predictions made by the PQS theory and the classical mixture interpretation

If the system is subject to further monitoring after the measurement M at time t, in addition to the density matrix $\rho(t)$ which presents the information before time t and predicts the outcome probabilities for the measurement at time t, we also have further information which is represented by the effect matrix $E(t)$. The pair of matrices $(\rho(t), E(t))$ is the so-called Past Quantum State which makes more confident predictions for any such measurement performed at the earlier time t [50]. This prediction based on the PQS is given by,

$$P_P(m) = \frac{\mathrm{Tr}(\Omega_m \rho(t) \Omega_m^\dagger E(t))}{\sum_{m'} \mathrm{Tr}(\Omega_{m'} \rho(t) \Omega_{m'}^\dagger E(t))}. \tag{3.2}$$

The subscript P for *Past* in Eq.(3.2) reflects that we are (at time T or later) retrodicting the probability for the outcome of a measurement at the past time t. The name *quantum smoothing* has been proposed for the retrodiction of properties of the quantum systems [49, 55, 56, 117], derived from the similar term smoothing used for classical stochastic processes.

In this chapter, we describe experimental tests of the PQS theory Eq. (3.2) in the context of of projective measurements. We specifically focus on the case where

the dynamics and the probing of the quantum system, as shown in Fig. 3.2, confine the density matrix $\rho(t)$ and the matrix $E(t)$ to be diagonal in a definite basis $\{|n\rangle\}$. In that case, Eq.(3.2) yields the probability that a measurement at time t found the system in state $|n\rangle$ ($\Omega_n = |n\rangle\langle n|$),

$$P_P(n) = \frac{\rho_{nn}(t)E_{nn}(t)}{\sum_{n'} \rho_{n'n'}(t)E_{n'n'}(t)} \tag{3.3}$$

which is equivalent to the expression obtained in the classical forward-backward analysis [118, 119]. In analogy with the classical mixture interpretation in Eq. (3.1) given by the diagonal density matrix ρ, we might expect that smoothed probabilities $P_P(n)$ would also permit a classical mixture interpretation as if the system did occupy the quantum states $|n\rangle$ with probabilities $P_P(n)$ at time t (the hidden variable model). But the prediction based on such a classical mixture interpretation of the state defined by the pair of diagonal matrices $\rho(t)$ and $E(t)$,

$$P_P^{cm}(m) = \sum_n P_P(n)\mathrm{Tr}\big(\Omega_m|n\rangle\langle n|\Omega_m^\dagger\big), \tag{3.4}$$

generally disagrees with Eq.(3.2) for operators Ω_m which are not diagonal in the same basis as $\rho(t)$ and $E(t)$.

Next we will do a simple calculation with the operators $\Pi_{\pm,\theta}$ using the Eq. (3.2) and Eq. (3.4) for the diagonal density matrices $\rho(t)$ and $E(t)$. For a projective measurement in the σ_z basis in which $\theta = 0$ at time t, the diagonal $\rho(t)$ leads to the prediction $P_\rho(0) = \rho_{00}(t)$, while the pair of diagonal matrices $\big(\rho(t), E(t)\big)$ implies

$$P_P(0) \equiv P_P(+,0) = \frac{\rho_{00}(t)E_{00}(t)}{\rho_{00}(t)E_{00}(t) + \rho_{11}(t)E_{11}(t)}. \tag{3.5}$$

If the values of $P_P(0)$ and $P_P(1)$ ($P_P(1) \equiv P_P(-,0) = 1 - P_P(0)$) could be interpreted as refined populations of a classical mixture of the two qubit states at time t then the projective measurement with the POVM operator $\Pi_{+,\theta}$ would have the weighted

probability based on the Eq. (3.4),

$$P_P^{cm}(+,\theta) = P_P(0)\cos^2\left(\frac{\theta}{2}\right) + P_P(1)\sin^2\left(\frac{\theta}{2}\right), \tag{3.6}$$

However, if we plug the projection operators $\Pi_{\pm\theta}$ for Ω_m into the PQS formalism Eq. (3.2), we have

$$P_P(+,\theta) = \frac{P_\rho(+,\theta)P_E(+,\theta)}{P_\rho(+,\theta)P_E(+,\theta) + P_\rho(-,\theta)P_E(-,\theta)}, \tag{3.7}$$

where $P_\rho(+,\theta)$ is given in (3.8), and we have introduced the formally similar $P_E(+,\theta) = E_{00}\cos^2\left(\frac{\theta}{2}\right) + E_{11}\sin^2\left(\frac{\theta}{2}\right)$ and $P_\rho(-,\theta) = 1 - P_\rho(+,\theta)$, $P_E(-,\theta) = 1 - P_E(+,\theta)$.

In the following sections, we will describe experiments on a superconducting qubit as illustrated in Fig. 3.2. We first prepare the qubit in a mixed state followed by a test measurement. After the test measurement, the system is subject to further probing to obtain the information for $E(t)$. Thus the experiment gives us access to both diagonal matrices $\rho(t)$ and $E(t)$, furthermore, by predicting the outcomes of the test measurement we can get $P(+,\theta)$ and compare Eq. (3.7) and Eq. (3.6). In the next section, we will show that projective test measurements in bases different from the density matrix eigenbasis will confirm Eq. (3.2) while ruling out the classical mixture interpretation leading to Eq. (3.4).

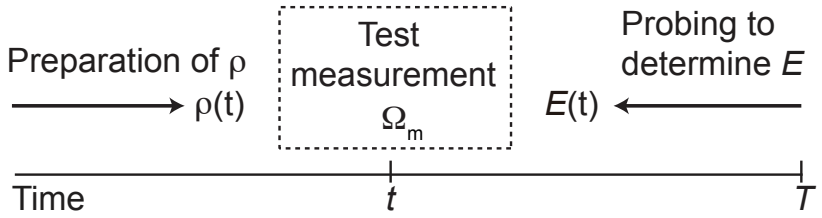

Figure 3.2: Experiment sequence. (1) the system is first prepared in state given by density matrix $\rho(t)$, (2) a test measurement, described by a POVM Ω_m, is conducted at time t, and (3) subsequent probing measurements of the system from time t to T are used to collect further information about the system which is encoded in the matrix $E(t)$.

3.3 Experimental set-up

In this experiment, as illustrated in Fig. 3.3, we employ a superconducting qubit, which is embedded in a three dimensional aluminum cavity [92]. The transmon qubit was fabricated by double angle evaporation of aluminum on high resistivity silicon substrate and is characterized by charging energy $E_C/h = 340$ MHz and Josephson energy $E_J/h = 11.3$ GHz. The charging energy, E_C, is obtained from the anharmonicity of the lowest two qubit levels, and E_J is calculated from the relation $\hbar\omega_q = \sqrt{8E_JE_C} - E_C$. The qubit transition frequency is $\omega_q/2\pi = 5.44888$ GHz. We have obtained the energy decay time $T_1 = 8\ \mu s$ and the Ramsy decay time $T_2^* = 9.5\ \mu s$ using standard measurement techniques [104]. In the experiment, due to the anharmonicity of the transmon qubit, we are able to use the two lowest levels of the transmon to realize a pseudo-spin half system described by a 2×2 density matrix ρ. The cavity is machined from 6061 bulk aluminum with resonant frequency is $\omega_c/2\pi = 6.76208$ GHz, linewidth $\kappa/2\pi = 6.3$ MHz and dispersive coupling rate $\chi/2\pi = -0.8$ MHz. The interaction between the qubit and the cavity is described by an interaction Hamiltonian $H_{\text{int.}} = -\hbar\chi\sigma_z a^\dagger a$, where σ_z (and $\sigma_x,\ \sigma_y$) are Pauli operators, $a^\dagger(a)$ are the creation (annihilation) operators for a photon in the cavity mode. This interaction allows quantum non-demolition (QND) measurements of the qubit in the σ_z basis through probing of the qubit-state-dependent cavity resonance [68]. A microwave tone, which probes the cavity, acquires a qubit-state-dependent phase shift. The signal reflected off the cavity is amplified by a near-quantum-limited Josephson parametric amplifier (JPA) which consists of a 1.5 pF capacitor shunted by a SQUID composed of two Josephson junctions with critical current $I_0 = 1\ \mu A$. The JPA is operated with small flux threading the SQUID loop and pumped by two sidebands that are equally separated from the carrier by 250 MHz which produces 15 dB gain with an instantaneous 3-dB-bandwidth of 80 MHz.

With the experimental set-up as shown in Fig. 3.3 (more detail can be found in Fig. 3.9), we can perform experiments with variable strength measurements on the qubit state characterized by a measurement timescale τ. We use time steps $\delta t \ll \tau$

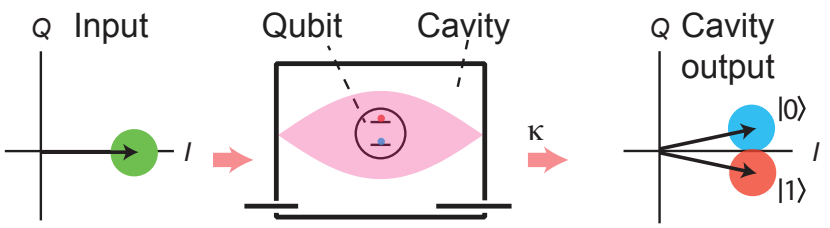

Figure 3.3: Experimental implementation. The dispersive interaction between a superconducting qubit and a cavity results in a qubit-state-dependent phase shift on a weak coherent drive on the cavity. Sufficient drive strength and narrow integration bandwidth result in disjoint measurement distributions for one of the field quadratures, allowing single shot, quantum non-demolition measurements of the qubit in the energy eigenbasis.

in order to execute weak measurements of the qubit state. However, by integrating the weak measurement signal for a time $T \gg \tau$ we can effectively accumulate weak measurements in a projective measurement of the qubit in the σ_z basis. Hence, this measurement architecture can be used for projective measurements in the energy basis, represented by the projection operators $\Omega_m : \Pi_{\pm,z}$. These measurements achieve fidelities in excess of 95%, with the predominant sources of infidelity arising from qubit transitions [84, 120] that occur during the finite duration of the measurement [121–125].

We shall study quantum smoothing in the context of projective measurements with the experiment set-up described above. Whereas the density matrix $\rho(t)$, which depends on the evolution dynamics and measurements performed prior to time t makes predictions about the outcomes of measurements performed at time t, further probing of the qubit allows us to refine our prediction in hindsight.

3.4 Experimental results

In this section, we will first show the experimentally verified predictions made by the diagonal density matrix $\rho(t)$ which means our system is well calibrated and ready for further test experiment. We then describe the experiments with further information represented by the diagonal effect matrix $E(t)$. Finally, with our experimental results,

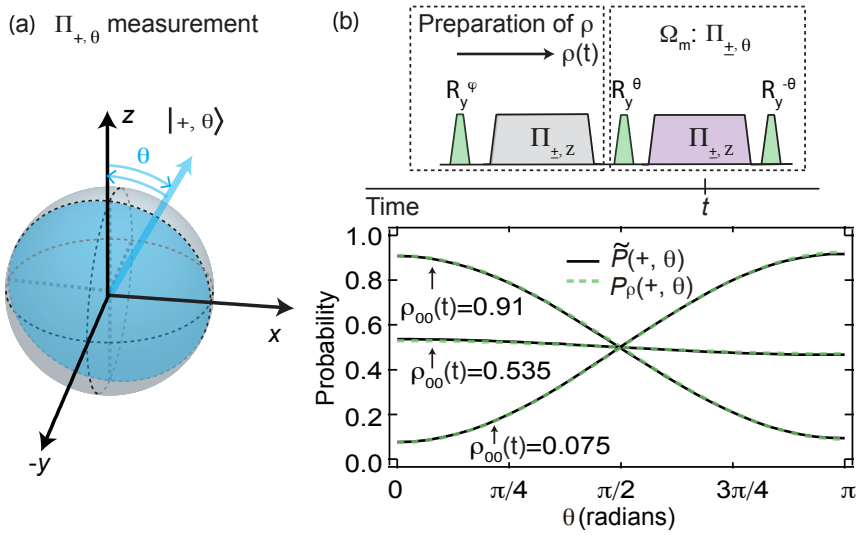

Figure 3.4: Prediction based on diagonal ρ. (a) By combining projective measurements in the energy basis (along z) with rotations about the y axis of the qubit state, projective measurements along an axis that forms an angle θ with the z axis can be realized. (b) Different initial states ρ that are diagonal in the energy basis are prepared by performing an initial rotation and projective measurement. The results of the projective measurement are ignored. We verify that the probability of a positive projective measurement outcome $\tilde{P}(+,\theta)$ is in agreement with the predictions of the initial density matrix $P_\rho(+,\theta)$ for three different initial mixed states characterized by $(\rho_{00}(t) = 0.91,\ 0.535,\ 0.075)$. Over 5×10^4 experimental repetitions are used for each measured $\tilde{P}(+,\theta)$ leading to a statistical uncertainty of order 4×10^{-3}.

we will compare the predictions made by the Past Quantum State theory with the predictions made by the classical mixture interpretation.

3.4.1 The prediction based on diagonal ρ

We have shown the experiment sequence to test our idea on quantum smoothing for the classical mixtures in Figure 3.2. In the following section, we will discuss the experiments in the context of projective measurement in more detail. In experiments, we can make more general projective measurements by combining measurements in the σ_z basis with arbitrary rotations $(R_x^\theta,\ R_y^\theta)$ about the x and y axes of the qubit, where θ is the rotation angle. Our first step is to prepare the qubit initially in a mixed state. To implement this, we apply a qubit rotation pulse R_y^φ followed by a projective measurement $\Pi_{\pm,z}$. The projective measurement collapses the qubit state,

decoheres the system, and effectively prepares the qubit in a diagonal mixed state in the qubit basis eigenstates $|0(1)\rangle \equiv |+(-)z\rangle$. We obtain the value of $\rho_{00}(t)$ and $\rho_{11}(t)$ for an ensemble of experiments. The qubit's initially mixed state described by the density matrix $\rho(t)$ is basically determined by the initial rotation angle φ. In our case, it is also related to the T_1 decay process during the first projective measurement to prepare $\rho(t)$ because the projective measurement time $t = 400$ ns cannot be ignored due to the relatively short T_1 time in this experiment. By considering the T_1 decay process, we can prepare the mixed state with exquisite accuracy using the rotation pulse R_y^{φ} followed by the projective measurement. Furthermore, we can test our experiment in the $|\theta\rangle$ basis immediately after the preparation by using another strong projective measurement (θ measurement) and comparing our experimental results with the theory predictions.

The θ measurement, which is simply a projective measurement along the axis that forms an angle θ with the z axis and azimuthal angle $\phi = 0$, can be realized by the following operations, $\Pi_{\pm,\theta} = R_y^{-\theta}\ \Pi_{\pm,z}\ R_y^{\theta}$ as shown in Figure 3.4(b). The system is first rotated by an angle θ followed by a projective measurement, and then we apply a $-\theta$ pulse to rotate it back. Of course, these θ measurements $\Pi_{\pm,\theta}$ satisfy the properties of the POVMs operators, and we have $\Omega_{\pm,\theta} = \Omega_{\pm,\theta}^{\dagger} \equiv \Pi_{\pm,\theta}$. After plugging the $\Pi_{\pm,\theta}$ into $P(m) = \mathrm{Tr}(\Omega_m \rho \Omega_m^{\dagger})$ for a diagonal density matrix $\rho(t)$, the probability of obtaining the eigenvalue $+1$ (associated with the state $|0\rangle$) from θ measurement is given by,

$$P_{\rho}(+,\theta) = \rho_{00}(t)\cos^2\left(\frac{\theta}{2}\right) + \rho_{11}(t)\sin^2\left(\frac{\theta}{2}\right). \tag{3.8}$$

In the following paragraph, we test the predictions in Eq. (3.8) in our experiment.

The experiment sequence is shown in Figure 3.4(b). After the preparation of the diagonal density matrix $\rho(t)$, we perform a θ measurement for different angles θ to determine $\tilde{P}(+,\theta) \equiv N_+/(N_+ + N_-)$ from the number of positive (negative) eigenvalue results N_+ (N_-). In experiments, as we mentioned in the previous section, the projective measurements $\Pi_{\pm,\theta}$ are subject to infidelities originating predominantly

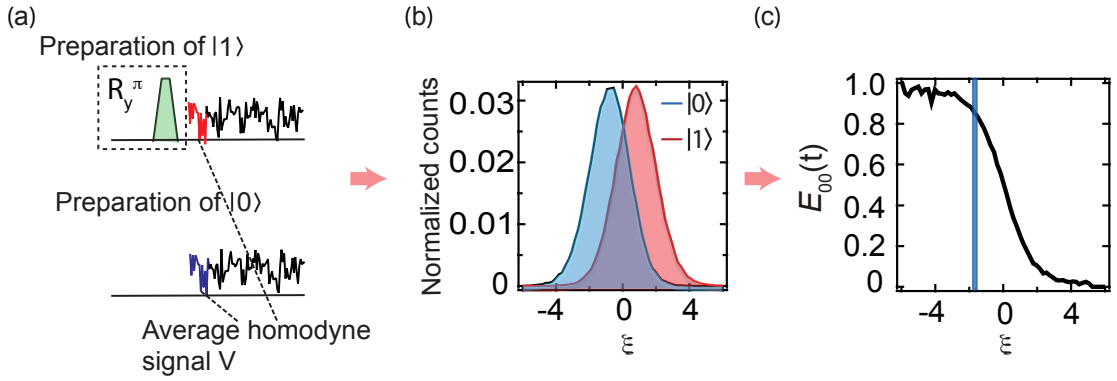

Figure 3.5: Determination of E. (a) Experimental sequence to prepare the qubit in the ground or excited state. (b). Histograms of the integrated 30 ns weak signals ξ for the qubit prepared in the ground (blue) and excited (red) state which are obtained by averaging 30 ns of weak signal immediately after the preparation as shown in (a). (c) The distributions are used to create the map between ξ and $E_{00}(t)$. The finite width of the post-selection window for determination of $E(t)$, shown as the blue vertical line, gives rise to a range of values for the theory predictions.

from T_1 decay during the projective measurement with $t_{\rm m} = 400$ ns. This results in a θ-dependent measurement fidelity that is given by the overlap of the $\Pi_{\pm,\theta}$ eigenstates and the qubit excited state, $\mathcal{F}_\theta = 0.99 - \sin^2(\theta/2)(1 - e^{-t_{\rm m}/T_1})$ and ranges from 0.945 when $\theta = \pi$ to 0.99 when $\theta = 0$. The maximum readout fidelity of 0.99 arises from residual overlap of the measurement distributions. As shown in Figure 3.4(b), the black curve is the theory prediction made by $\rho(t)$ in Eq. (3.8). The green dashed lines represent the experimental data $\tilde{P}(+,\theta)$ which agree well with the theory predictions after taking the measurement fidelity $\mathcal{F}_\theta$ into account. Therefore, we have verified the predictions made by the diagonal density matrix $\rho(t)$, which also means that the system is well calibrated and ready for the next experiment to test the smoothed predictions made by both diagonal $\rho(t)$ and $E(t)$.

3.4.2 The method of determining $E(t)$

The next crucial step of this experiment is to determine the effect matrix $E(t)$ in further probing. After the dispersive interaction, the phase of the coherent probe field depends on the qubit state, and the time-integrated value of the measured Q-

quadrature is Gaussian-distributed with opposite mean values for the states $|0\rangle$ or $|1\rangle$. In the experiment, as illustrated in Figure 3.5(b), we first prepare the qubit in the excited or ground state to obtain the corresponding distributions of the 30 ns of the average weak signal. These distributions can be used to create a map between the effect matrix $E(t)$ and the post-selected signal ξ. In Figure 3.5b, we show the experimentally obtained distributions $P(\xi|0)$ and $P(\xi|1)$, where we have normalized the integrated signal to have mean values ± 1 for the two qubit states. The Gaussian widths are larger for short probing times and become much narrower when the system is probed for longer. This Gaussian width reveals the measurement strength in the experiment. For a given measured signal ξ, we can extract the probabilities $P(\xi|0)$ and $P(\xi|1)$ based on the distributions, i.e., the probability of the measured signal conditioned on the state. Through Bayes' rule, these are precisely the factors multiplying the prior probabilities $\rho_{nn}(t)$ to yield the classical smoothing theory. In this case, we may disregard the effect of qubit decay during the probing since the time for the post-selection is only 30 ns which is much shorter than the decay time T_1. These distributions yield the values of $E_{00}(t)$ and $E_{11}(t)$ in Eqs.(3.2, 3.4),

$$E_{00}(t) = \frac{P(\xi|0)}{P(\xi|1) + P(\xi|0)}, \; E_{11}(t) = \frac{P(\xi|1)}{P(\xi|1) + P(\xi|0)}, \tag{3.9}$$

where we have applied a common normalization factor, leading to $\mathrm{Tr}(E) = 1$. Figure 3.5(c) shows how the inferred normalized value of E_{00}(t) ($E_{11} = 1 - E_{00}$) depends on the measured signal ξ. In our experiment, we post-select 30 ns of weak signal after the θ measurement $\Pi_{\pm,\theta}$, and then we can infer the $E(t)$ using the map in Figure 3.5(c) with the post-selected average weak signal. The continuous probing constitutes a QND measurement of the qubit state, and the accumulated back-action on the qubit's state populations in the forward propagation of $\rho(t)$ [126] amounts to the same factors—which confirms that the evolution of $E(t)$ is indeed equivalent to the evolution of $\rho(t)$.

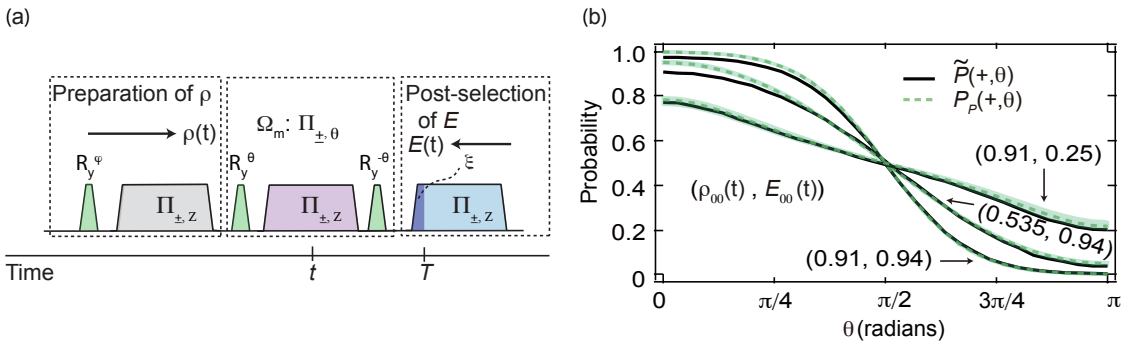

Figure 3.6: Smoothed prediction based on diagonal ρ and E. (a) Experimental sequence and comparison of experiments with the predictions of projective qubit measurement outcomes along θ using both ρ and E for three different mixed states. After the $\Pi_{\pm,\theta}$ measurement, a 30 ns integration of a readout signal is used to determine $E(t)$. (b) The solid lines are the measured probability based on over 5×10^4 experimental iterations for each value of θ, and the dashed lines are the theoretical prediction from Eq. (3.7).

3.4.3 Smoothed prediction based on diagonal $\rho(t)$ and $E(t)$ from the experiment

For the rest of this section, we are going to perform experiments to show how the subsequent continuous probing of the qubit in the σ_z basis yields our smoothed predictions for the outcomes of the projective measurements $\Pi_{\pm,\theta}$. Then we will compare experimental results to the predictions of the PQS and of the classical mixture interpretation. We perform the experiment as shown in in Fig. 3.6(a) to test the predictions made by the Eqs. (3.7, 3.6). In order to obtain the $E(t)$, we subject the system to further probing and then use 30 ns of the post-selected readout signal to extract the corresponding $E(t)$ from the map in the Figure 3.5(c). Therefore E is determined by the averaged signals that were post-selected in a bin based on the Eq. (3.9). We sort these signals into bins of width 0.19 which results an uncertainty of the smoothed probability shown by the faint green curves.

In Figure 3.6(b), we display our experimental results that test the PQS prediction of Eq. (3.7) for three different combinations of $\rho(t)$ and $E(t)$. The black curves are the experimental data, which is the ratio of the number of positive eigenvalues to the total

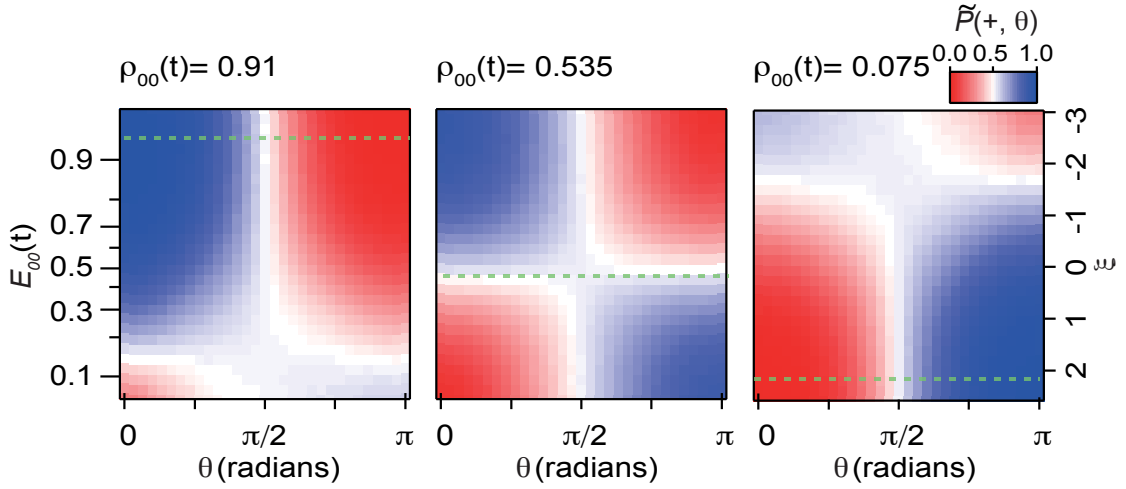

Figure 3.7: The experimentally determined $\tilde{P}(+, \theta)$ as function of θ and $E_{00}(t)$ is shown for three different initial states with $\rho_{00}(t) = \{0.91,\ 0.535, 0.075\}$ (left to right).

number of the post-selected experiments with certain $E(t)$. The experimental data and theoretical predictions (green dashed curves) made by the PQS theory show nice agreement and highlight how information before and after the projective measurement contribute to the smoothed prediction. As we can see from Figure 3.6(b), when $\rho(t)$ and $E(t)$ are similar ($\rho_{00} = 0.91$, $E_{00} = 0.94$), the prediction is more accurate than the prediction based on ρ alone, taking values close to 1 or 0 for some values of θ (compare to Fig. 3.4b). The later probing "confirms"the prediction by $\rho(t)$, and thus enhances the probability of the most likely outcome of the projective measurement. In contrast, if the two disagree ($\rho_{00} = 0.91$, $E_{00} = 0.25$), the smoothed prediction is less biased which is due to later probing that disagrees with the prior state $\rho(t)$. The experimental data have verified the predictions made by the PQS theory, thus showing the correctness of the Eq. (3.2).

Figure 3.7 summarizes our experimental results, showing the measured $\tilde{P}(+, \theta)$ as a function of the angle θ and the post-selected value of $E_{00}(t)$ (the corresponding values of the integrated signal ξ are given on the right hand axis in the figure). Results are shown for three different density matrices $\rho(t)$ prior to the projective measurement along the direction θ. For $\theta = \pi/2$ the smoothed predictions assign

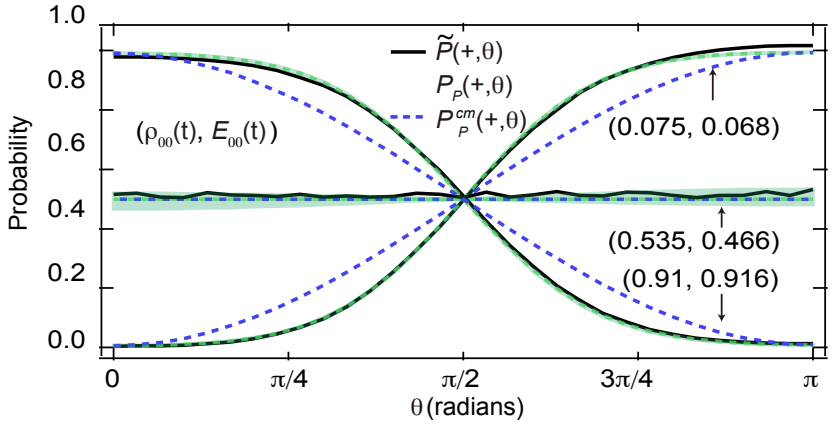

Figure 3.8: Comparison of the $\tilde{P}(+,\theta)$ (solid lines, based on over 5×10^4 experimental iterations with statistical errors of order 10^{-3}) to the smoothed prediction $P_P(+,\theta)$ (green dashed with green bands indicating the theory uncertainty which comes from the finite post-select window for E) and to the prediction based on a classical mixture with the smoothed state occupations, $P_P^{\rm cm}(+,\theta)$ (blue dashed).

unbiased probabilities 0.5 to the outcomes $\pm,\theta$. For any θ and for all three values of $\rho(t)$, a certain value of the probing signal after the projective measurements results in an unbiased smoothed prediction $P_P(+,\theta) = 0.5$. This amounts to an increased uncertainty about the outcome and it happens because the subsequent probing of the system is in disagreement with the prior state $\rho(t)$.

3.4.4 Comparison between the classical mixture interpretation and the PQS theory

In Figure 3.8, we compare the experimental data with the prediction made by the PQS theory and the classical mixture interpretation. The black curves are the experimental data with three different $(\rho_{00}(t), E_{00}(t))$. The green dashed lines are the predictions made by the PQS theory (Eq. (3.2)) which agree well with the experimental data. The blue dashed lines are the predictions made the classical mixture interpretation (Eq. (3.2)), which clearly disagree with the experimental data.

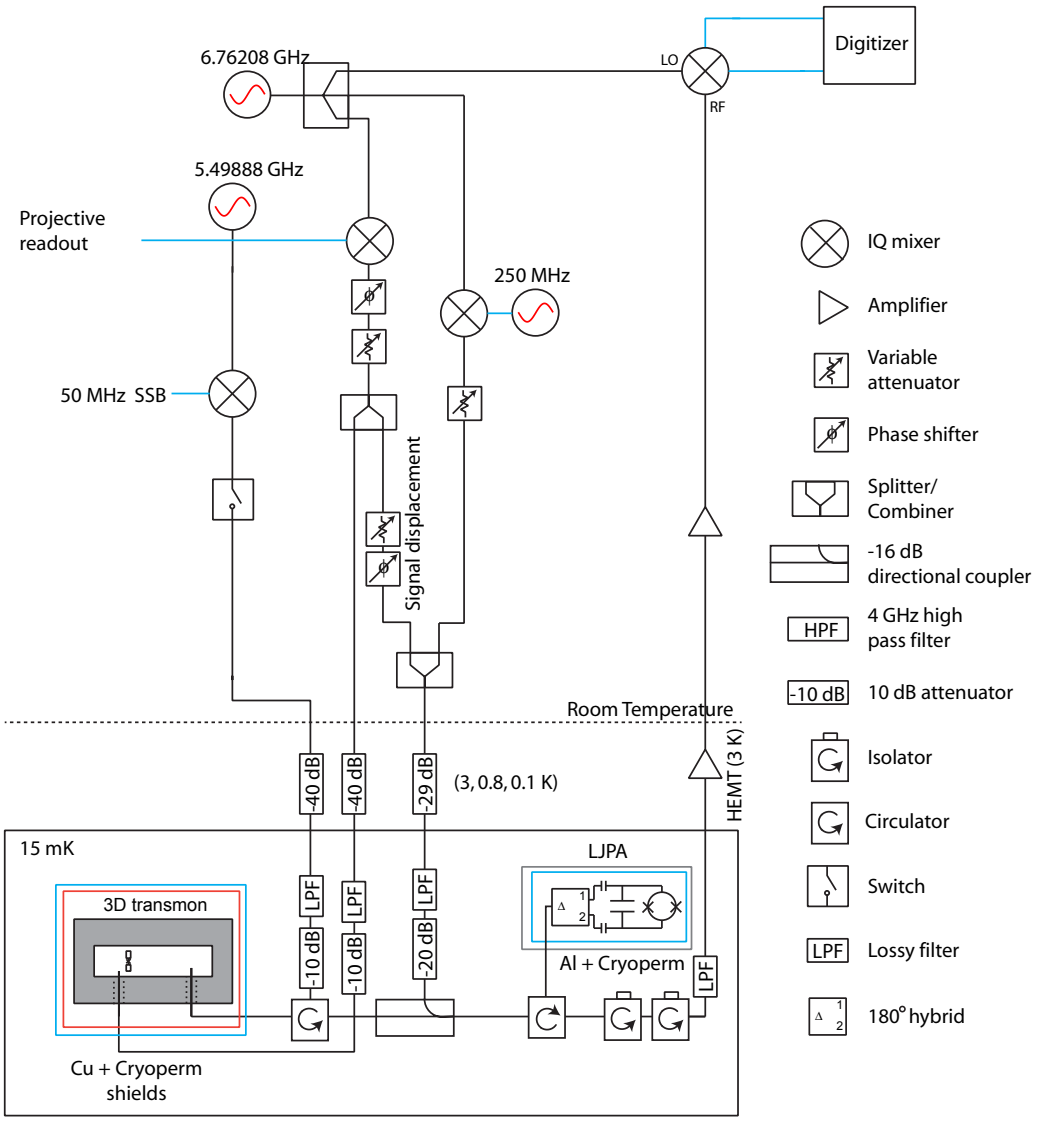

Figure 3.9: Experimental set-up. The qubit drive pulse is generated by standard single side-band (SSB) modulation of microwave tones. Qubit readout, the amplifier pump and the local oscillator for the demodulation are generated by another microwave frequency generator.

3.5 Conclusion

It's interesting to mention that in the classical world a measurement Ω_m at time t has no effect on the state of the system. Further information after the measurement at time t merely assures the measurement outcomes at time t and refines the prediction for the measurement outcomes at that time. However, in quantum mechanics, the quantum system is entangled with the probe and any measurement performed on the quantum system causes back-action on the state of the quantum system. This back-action may populate states that are not diagonal in the eigenbasis $\{|n\rangle\}$ of $\rho(t)$. In this case, The diagonal matrices $\rho(t)$ and $E(t)$ are independent of the specific measurement at time t.

In this chapter, we have presented a description of a quantum system, evolving without developing coherences, and hence, both prior and posterior information about the system are represented by diagonal matrices. While the theory of smoothing yields probabilities in better agreement with predictions for the outcome of measurements in the eigenstate basis, we have shown that these probabilities do not permit a classical mixture interpretation of the (past) quantum state. Our work rules out simple "hidden variable theories" that equate eigenstates of incoherent ensembles with hidden "true" states of the system. Instead of demonstrating an explicit statistical violation of the Bell [127], CSCH [128], or Leggett-Garg [129–133] inequalities, we have simply shown the failure of the simplest preconceived probabilistic classical mixture interpretation of the quantum description [134].

Chapter 4

Predicting the future and retrodicting the past with a superconducting qubit

In quantum measurement, the state of a quantum system, represented by the density matrix $\rho(t)$, undergoes unitary evolution and can be continuously monitored. The evolution of the quantum state in its phase space, which is known as a quantum trajectory, is inferred from the weak measurement signal by employing a stochastic master equation (SME) or a Bayesian update, and can be tomographically verified using strong projective measurements. Thus the density matrix $\rho(t)$ evolves in a stochastic way and can be propagated forward to make predictions for the outcome of some measurement based on the past evolution [113]. The outcomes of the measurement affect the quantum state $\rho(t)$ in the form of small perturbation on the state or even collapse of state which is called measurement back-action. The question is whether there is any effect that the measurement performed at time $t' \in (t, T]$ has on the "state" of the system at time t? The answer is "yes ", since we have more knowledge about the state of the system which also depends on the outcome of the measurement after time t due to the measurement back-action. Furthermore, with this further information which is represented by the effect matrix $E(t)$, we want to ask the questions: what happened regarding the evolution of the system? Does the

future affect the past in the quantum world. That is, can we more accurately describe the state with the past quantum state $\Xi = [\rho(t), E(t)]$ which encapsulates both $\rho(t)$ and $E(t)$?

With these questions in mind, I will first give you a simple classical example with laundry keys to get you into what we are going to discuss. Here is what I will call the the laundry-key finding example: as a graduate student, it is common to share an apartment with a roommate. I personally live with a roommate (Weijian) in an apartment with four rooms. We do laundry every week but we only have one key to the resident laundry room. Quite often, we don't do laundry together and need to run around to look for the key every time. The probability for finding the key in one of the four rooms is $\frac{1}{4}$ which can be considered as the initial state of the key, that is, if asked to guess the location of the key, my roommate, Weijian could assign equal probability to each room. Let's assume that I used the key last week and put it on the table in my bedroom after finishing my laundry. Now my roommate needs the key and so starts to search for it. The probability for finding the key will change conditioned on what he sees since he has more information which can be used to update the state of the key (his state of knowledge about the key). Finally, he will exclude the other three rooms and find the key on the table in my bedroom with unity probability at final time T. Now if asked by me: where do you think I left the key? The point is that the roommate is guessing about things in the past and the purpose of this chapter is to explore questions like this in quantum measurement. Of course, Weijian can always check with me to test where the key is. In this example, this process of update is very common (joint probability) which is very similar to the quantum mechanical measurement back-action. In quantum measurement, the back-action changes the state of the system that we are interested in. With further information, we have more knowledge about the system and learn something later which is so-called hindsight effect. Having found the key at final time T, meaning that he know where it is at this time and it also tells that where it was at time t, which is the past. He could then confidently guess where I left the key at some earlier time. But what if this was a quantum key which existed in a superposition

of several different locations. How would this example of hindsight change? This is the question we would like to answer in this chapter. The following sections describe an experiment to test the idea of a Past Quantum State theory in the context of continuous measurement. The work presented in this chapter is published in D. Tan et al. Phys. Rev. Lett. **114**, 090403 (2015).

4.1 Experimental set-up

The experimental set-up as shown in Figure 4.1 is similar to the experiment in the last chapter but uses a different qubit with transition frequency $\omega_q/2\pi = 4.0033$ GHz and coherence properties, $T_1 = 30$ μs, $T_2^* = 16$ μs. The qubit is dispersively coupled to a wave-guide cavity with resonance frequency $\omega_c/2\pi = 6.9914$ GHz, linewidth $\kappa/2\pi = 9.88$ MHz, and dispersive coupling $\chi/2\pi = -0.425$ MHz. Compared to the previous chapter's experiment, this set-up has smaller χ and larger κ for the purpose of performing weak measurement. A microwave tone that probes the cavity with an average intracavity photon number $\bar{n} = \langle a^\dagger a \rangle$ thus acquires a qubit-state-dependent phase shift. Since $2|\chi| \ll \kappa$, qubit state information is encoded in one quadrature of the reflected microwave signal. We amplify this quadrature of the signal with a near-quantum-limited Josephson parametric amplifier [45]. After further amplification, the measurement signal is demodulated and digitized. In the experiment, the superconducting qubit is subject to continuous monitoring and driven unitary evolution. We can collect data over time and make use of the full measurement record to illustrate the laundry-key finding example in the quantum world. In the following sections, after introducing the method of state update, we will then show how measurements before time t can be used to make predictions about measurements at time t, while measurements after time t can be used to make predictions about past events — retrodictions about— performed before time t. With the capability of tracking single trajectories [110, 135], we will then describe three applications of our experiment using continuous weak measurement. Finally, we will give the conclusion of the project.

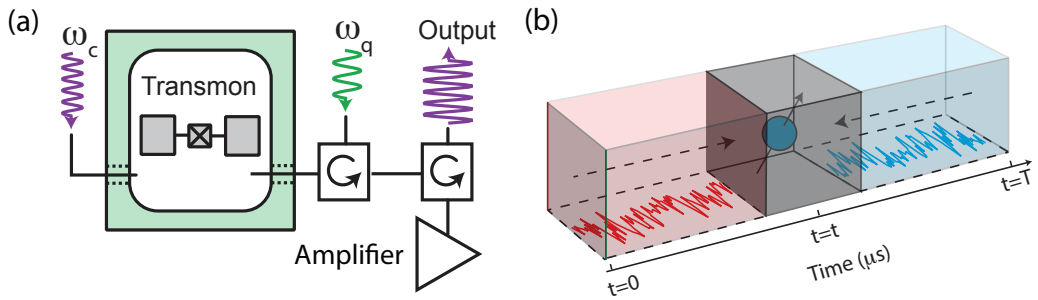

Figure 4.1: Schematic of experimental set-up. (a) Simplified experimental setup consisting of a transmon circuit coupled to a waveguide cavity. The signal transmitting through the cavity acquires a qubit-state-dependent phase shift. (b) By employing the quantum trajectory theory, we can predict the outcome of a measurement based on the information in the past (red curve), and we can also retrodict the measurement outcome using the information in the future (blue curve). With the whole measurement record, we use the PQS theory to make more confident prediction for the outcome of the measurement.

4.2 State update

In this section, we apply Stochastic Master Equation (SME) and Bayesian update methods to the quantum system to show how we update the state conditioned on experimental measurement signal with these techniques.

4.2.1 Stochastic master equation

The dynamics of an open quantum system are well described by the Lindblad master equation (2.41). If the system is subject to a continuous measurement, the evolution of the density matrix $\rho(t)$ conditioned on the measurement outcomes before time t is given by the stochastic master equation [113, 114]:

$$\frac{d}{dt}\rho(t) = \mathcal{L}\rho = -\frac{\mathrm{i}}{\hbar}[\hat{H}, \rho(t)] + \sum_{k=1}^{K} \mathcal{D}[\hat{L}_k]\rho(t) + \sqrt{\eta}(\hat{c}\rho(t) + \rho(t)\hat{c}^\dagger)V(t), \tag{4.1}$$

where η is the quantum efficiency and $V(t)$ is the random measurement signal at time t with mean value $\sqrt{\eta}\mathrm{Tr}((\hat{c} + \hat{c}^\dagger)\rho(t))dt$ and variance $\sigma^2 = dt$. Note this is just the

Lindblad master equation with an additional term incorporating information from measurement.

Next, we are going to apply this equation in our experiment. In our case, the qubit is subject to unitary rotations given by $H_{\mathrm{R}} = \hbar\Omega_R\sigma_y/2$, and continuous probing given by the measurement operator $\hat{c} = \sqrt{k}\sigma_z$, where σ_z is the Pauli spin operator, and $k = 4\chi^2\bar{n}/\kappa = 1/(4\eta\tau)$ parametrizes the measurement strength. Since the system is open, it is subject to dephasing due to the coupling to the environment which can be described by the Lindblad operator $\mathcal{L} = \sqrt{\frac{\gamma}{2}}\sigma_z$. At the same time, the measurement process, which is sensitive to the σ_z also dephases the qubit described by $\mathcal{L} = \hat{c} = \sqrt{k}\sigma_z$ and can be included in the above Lindblad master equation.

By plugging these operators in Eq. (4.1), we can get the following explicit equation for our experiment:

$$\frac{d\rho(t)}{dt} = -\mathrm{i}\frac{\Omega_R}{2}[\sigma_y, \rho(t)] + (k + \frac{\gamma}{2})(\sigma_z\rho(t)\sigma_z - \rho(t)) \\ + 2\eta k(\sigma_z\rho(t) + \rho(t)\sigma_z - 2\mathrm{Tr}(\sigma_z\rho(t))\rho(t))V(t), \quad (4.2)$$

where Ω_R is the Rabi frequency and $V(t)$ is the measurement signal in our experiment which is Gaussian distributed and scaled such that the distributions are centered at $+1$ and -1 for the $|0\rangle$ and $|1\rangle$ state. The first two terms are the standard master equation in Lindblad form, and the third term is the stochastic term that is used to update the qubit state based on the measurement result.

By expanding the Eq. (4.2), we can write the following equations for all the density matrix components:

$$d\rho_{11}(t) = \Omega_R\rho_{01}(t)dt + 2k\eta dt(-2\rho_{11}(t) - 2(1 - \rho_{11}(t))\rho_{11}(t))V(t) - \rho_{11}(t), \quad (4.3)$$

$$d\rho_{01}(t) = -\frac{\Omega_R}{2}(\rho_{11}(t)-\rho_{00}(t))dt-2(k+\gamma/2)\rho_{01}(t)-2k\eta dt\rho_{01}(t)(2-4\rho_{11}(t))V(t)-\rho_{01}(t). \quad (4.4)$$

Therefore, we can use the above stochastic master equation with the continuous weak measurement signal to obtain quantum trajectories and make prediction for the state

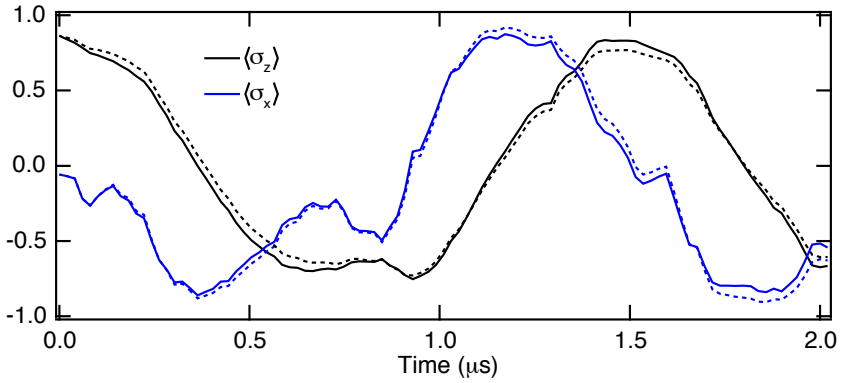

Figure 4.2: Comparison of the quantum trajectory given by $(\langle\sigma_x\rangle, \langle\sigma_z\rangle)$ calculated with Eq. (4.2) (solid) and the Bayesian update procedure Eq. (4.8) and Eq. (4.7) (dashed). The two techniques give very similar results.

of qubit.

4.2.2 Bayesian update

In this subsection, we show that we can also use the Bayesian update method to update the trajectories based on the measurement signal $V(t)$ [113, 126]. In Bayes' theorem, we know that the probability of getting event A given that we know the event B can be express in the following: $P(A|B) = P(B|A)P(A)/P(B)$. In our experiment, the probability of the measurement record $V(t)$ conditioned on the ground $|0\rangle$ or excited state $|1\rangle$ is $P(V(t)|z = \pm 1)$ which can be given by distribution of the measurement signal for the ground and excited state respectively:

$$P(V(t)|z = -1) = \frac{1}{\sqrt{2\pi}a} \exp -\frac{(V(t)+1)^2}{2a^2}, \tag{4.5}$$

$$P(V(t)|z = +1) = \frac{1}{\sqrt{2\pi}a} \exp -\frac{(V(t)-1)^2}{2a^2}. \tag{4.6}$$

The measurement signals are Gaussian distributed and we scale the signal such that the distributions are centered at $+1$ and -1 for the $|0\rangle$ and $|1\rangle$ states respectively. The variance, $a^2 = 1/4k\eta\Delta t$, is related to the measurement strength k, the quantum efficiency η, and the integration time Δt. Therefore, we can apply Baye's rule to calculate the updated density matrix based on the measurement signal $V(t)$. The

following are the components of the density matrix:

$$d\rho_{11}(t) = \Omega_R \rho_{01}(t)dt + \frac{\rho_{11}(t)P(V(t)|z=-1)}{\rho_{00}(t)P(V(t)|z=1) + \rho_{11}(t)P(V(t)|z=-1)} - \rho_{11}(t), \quad (4.7)$$

$$d\rho_{01}(t) = -\frac{\Omega_R}{2}(\rho_{11}(t) - \rho_{00}(t))dt + \rho_{01}(t)\frac{\sqrt{\rho_{00}(t+\delta t)\rho_{11}(t+\delta t)}}{\sqrt{\rho_{00}(t)\rho_{11}(t)}}e^{-\gamma \Delta t} - \rho_{01}(t), \quad (4.8)$$

where γ is the decay rate. In our calculation, we have use the relation $\langle \sigma_u \rangle = \mathrm{Tr}(\rho \sigma_u)$, where $u = x, y, z$. We can use either Bayesian update method or SME to update the qubit state conditioned on the measurement signal. We find that the two methods are almost the same when the continuous measurement is very weak, and give very similar results for the parameters used in this experiment as displayed in Figure 4.2. Figure 4.2 gives a comparison of a single trajectory using the Bayesian update and SME and shows a nice agreement between these two methods. In this project, we choose to use the SME equation to update the state in consistence with the theory of POVMs.

4.2.3 The SME for $E(t)$

The effect matrix $E(t)$ solves a corresponding adjoint equation with a final condition $E_T = \hat{I}/2$ at final time T: [50],

$$\frac{dE}{dt} = \mathrm{i}\frac{\Omega_R}{2}[\sigma_y, E] + (k + \frac{\gamma}{2})(\sigma_z E \sigma_z - E) + 2\eta k(\sigma_z E + E\sigma_z - 2\mathrm{Tr}(\sigma_z E)E)V(t - dt), \quad (4.9)$$

where $dE_t = E_{t-dt} - E_t$, and we can propagate the above equation backward from the final time T to t using the same measurement record $V(t)$ as used for propagating the density matrix $\rho(t)$ in Eq. 4.2. We add a term $-4\eta k \mathrm{Tr}(\sigma_z E)EV(t - dt)$ in the third part of the above equation in order to confine the trace of $E(t)$ to be unity.

4.2.4 Measurement calibration

We use the histograms of the measurement signal for the $|0\rangle$ and $|1\rangle$ states to calibrate the measurement strength which is related to the variance $a^2 = 1/4k\eta\Delta t$ of the histograoms. In this experiment, we have the quantum efficiency $\eta = 0.35$ which is typically limited by losses induced by the microwave components, added noise from the amplifiers, and from environmental decoherence of the qubit. The quantum efficiency can be calculated from the relation $\eta = 1/(2\tau\Gamma)$, where τ is the measurement rate and Γ is the decay rate. For the parameters of our experiment, we have $\tau = 1.2\ \mu$s and $\Gamma/2\pi = 0.19$ MHz.

The quantum efficiency η was measured by fitting the distributions $P(V_t|z = +1)$ and $P(V_t|z = -1)$ to determine $a^2 = 1/4k\eta\Delta t$. The dispersive coupling rate $\chi/2\pi = -0.43$ MHz was determined by using a Ramsey measurement to measure both the ac Stark shift ($2\chi\bar{n}$) and the measurement induced dephasing rate ($\Gamma_m = 8\chi^2\bar{n}/\kappa$ for intracavity photon numbers ranging between $\bar{n} = 0$ and $\bar{n} = 1.3$).

4.3 Experimental results

4.3.1 Prediction

In this section, we describe an experiment to show how we make predictions for the outcome of some measurement which is described by the POVM operator $\Omega_{+x} = (\sigma_x+1)/2$. As illustrated in the experimental sequence in Figure 4.3, after preparation of an initial state, the system is subject to continuous weak measurement and Rabi drive followed by a rotation pulse and a projective measurement. For a single run of the experiment, we use the SME for $\rho(t)$ to propagate the density matrix forward in time from initial state $|+x\rangle$. The probability that the qubit is in $|+x\rangle$ state is given by $P(+x) = \mathrm{Tr}(\Omega_{+x}\rho_t\Omega_{+x}^\dagger)$. Thus we can calculate this probability as a function of the propagating time using Eq. (4.2) to update the state based on the measurement signal, which is shown as the black dashed line in Figure 4.3. We call this trajectory "the target trajectory", $\rho_{target}(t)$. In order to verify that we have tracked the qubit state

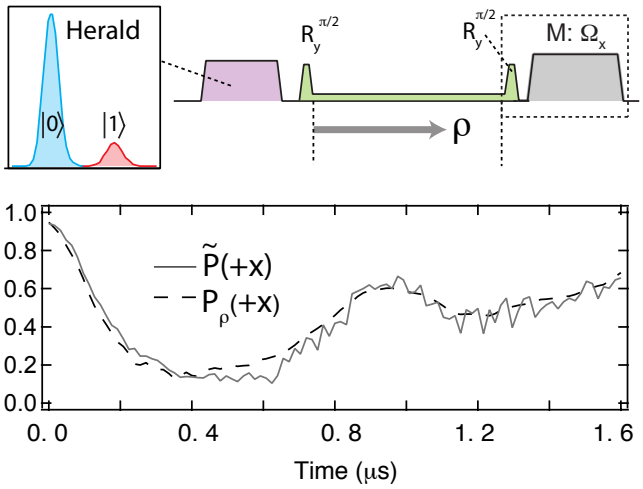

Figure 4.3: Prediction. Our experiment sequence starts with a herald measurement, followed by a rotation to prepare the qubit in the $|+x\rangle$ state. After this preparation, it is subject to continuous measurement and Rabi drive. We can propagate $\rho(t)$ forward in time, which makes accurate predictions about a final measurement M: Ω_x. The dashed line is the prediction based on a single quantum trajectory, and the solid line is the result from projective measurements on an ensemble of experiments that have similar values of $\rho(t)$.

correctly, we perform projective measurements of $\Omega_{\pm x}$ at time t on an ensemble of 3000 experiments that have similar values of $\rho_{target}(t)$ at time t (the target trajectory). Conditioned on this target value of $\rho(t)$, we obtain the corresponding experimental result $\tilde{P}(+x)$ based on the corresponding subset of measurements [110, 135]. We perform this analysis at different times and we observe close agreement between the single quantum trajectory prediction $P(+x)$ and the observed $\tilde{P}(+x)$.

4.3.2 Retrodiction

Using the information in the future to predict what happened in the past is called retrodiction. The experimental sequence is exactly the same as in the prediction section as shown in Figure 4.4, but we now use measurement data to retrodict the outcome of a previously performed measurement. As discussed in Chapter 2, the best prediction for the outcome of a previous measurement Ω_{+x} is given by $P_P(+x) = \frac{\mathrm{Tr}(\Omega_{+x}\rho_0\Omega_{+x}^\dagger E(t))}{\sum_{m=\pm x}\mathrm{Tr}(\Omega_m\rho_0\Omega_m^\dagger E(t))}$ based on the PQS theory. We assume that no measurements

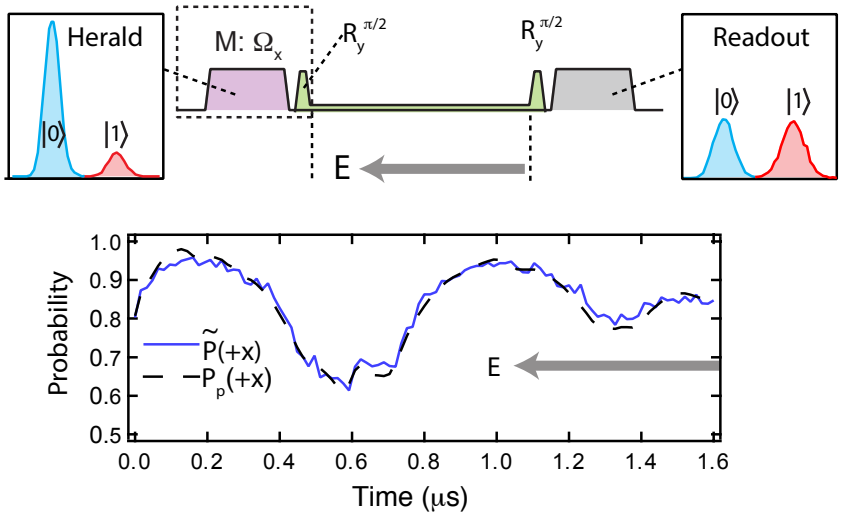

Figure 4.4: Retrodiction for a herald measurement. We propagate $E(t)$ backwards from the final state $E_T = \hat{I}/2$ using Eq.(4.9). For a single measurement record, this yields a retrodiction (shown as a dashed line) for the outcome of the herald measurement. The solid line, which is based on the heralded states that yielded similar values of E_0 confirms the retrodictions based on the single measurement record.

take place beyond the time T, leading to the final condition $E_T = \hat{I}/2$ [50]. If no measurements take place at all before T, for example because $\eta = 0$, Eq.(4.9) yields a solution for $E(t)$ that remains proportional to the identity operator for all times, and $P_P(+x)$ leads to the conventional expression that depends only on ρ_0.

To study retrodictions, we ignore the results of the herald measurements and use $\rho_0 = (P_0 - 1/2)\sigma_x + 1/2$ for the initial state which prepared by the thermal ground state fraction $P_0 = 0.85$. We calculate the retrodicted probability $P_P(+x)$ (Black dashed line in Fig. 4.4) for the outcome of the each herald measurement at $t = 0$ by propagating Eq. (4.9) backward with $E_T = \hat{I}/2$ from time T to $t = 0$. This yields the dashed line in Figure 4.4. To test the retrodictions, we then compare to the results of the measurement that are conditioned on $P_P(+x)$. The solid blue curve is obtained by averaging the outcomes of many herald measurements at time $t = 0$. The retrodiction is tomographically verified by an ensemble of herald experiments at $t = 0$ (Blue solid line in Fig. 4.4) which show nice agreement with the target retrodicted trajectory.

Furthermore, we test the retrodictions for the outcome Ω_z of the measurement M

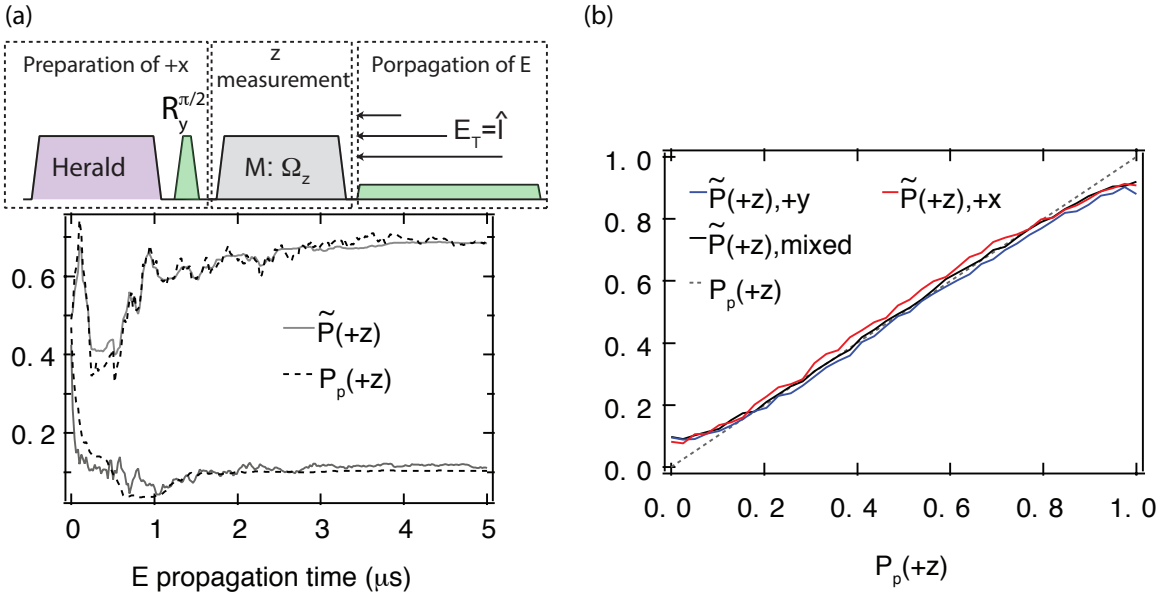

Figure 4.5: Retrodicted trajectories and tomography. (a) To test retrodictions made by $E(t)$ we prepare different states ρ_i and conduct a subsequent projective measurement M. We propagate $E(t)$ backwards from the final state $E_T = \hat{I}/2$ to E_0 for variable periods of time T. This yields a retrodiction (shown as dashed lines for two different experiments) for the outcome of M. The solid line, which is based on an ensemble of experiments that yielded similar values of E_0 confirms the retrodictions based on the single measurement record. (b) We prepare three different initial states ($+x$ in red, $+y$ in blue, mixed state in black), and compare the retrodictions, $P_P(+z)$, based on 5 μs of probing, to the outcomes of measurements M that yielded similar values of E_0.

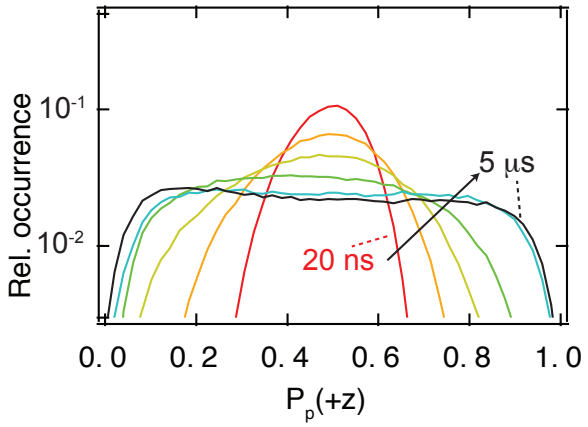

Figure 4.6: Histograms of $P_P(+z)$ for different propagation times. As more of the record is included, the retrodictions become more confident, taking values that are more often near 0 or 1. The arrow shows the E propagation time from 20 ns to $5\mu s$.

performed at time $t = 0$ with the backward propagating $E(t)$ for variable period of time from time T which is illustrated in Figure 4.5. We first prepare the initial state $|+x\rangle$ to test the retrodictions. In this case, $P_P(+z) = \frac{\mathrm{Tr}(\Omega_{+z}\rho_0\Omega_{+z}^\dagger E(t))}{\sum_{m=\pm z}\mathrm{Tr}(\Omega_m\rho_0\Omega_m^\dagger E(t))} = E_{00}(t)/2$. Note that the initial states ρ_0 make ambiguous predictions about the outcome of M, $P(+z) = 1/2$, yet information is available after M and by propagating $E(t)$ for longer times, the retrodiction for the outcome of M becomes more confident. We verify that the retrodictions are correct by averaging the outcomes of 3×10^5 runs of measurements M that corresponded to similar values of $E(t)$ to obtain an experimentally derived probability, $\tilde{P}(+z)$. Figure 4.5(a) displays two sample trajectories for the retrodiction $P_p(+z)$ along with $\tilde{P}(+z)$. These two are in a good agreement which means we have experimentally verified the retrodictions in a single retrodicted trajectories. As more of the further probing is included in the propagation of E, the retrodiction evolves and eventually settles on a fixed value. Figure 4.5(b) displays the results of 2×10^5 experimental tests for three different initial states ρ_0 which shows that the retrodiction $P_p(+z)$ and the tomography validation $\tilde{P}(+z)$ agree with each other for the whole ensemble of the trajectories. The slope of the line is close to unity which means that we tomographically verified all the trajectories. In Figure 4.6, we

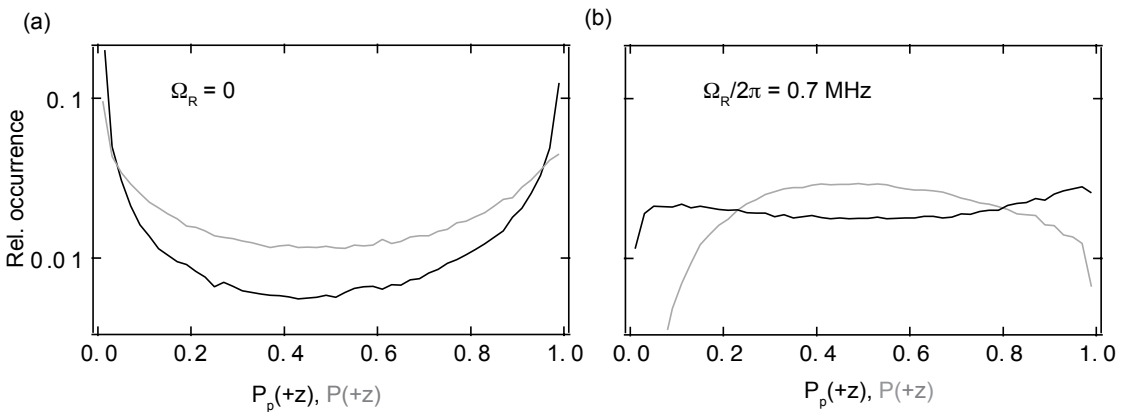

Figure 4.7: The occurrence of different values of $P(+z)$ and $P_p(+z)$ obtained from many iterations of the experiment shown in grey and black respectively. Panel (a) shows the case where $\Omega_R = 0$ and (b) shows the case where $\Omega_R/2\pi = 0.7$ MHz. In both cases, we have shown that the PQS makes more confident predictions with further information for the outcomes of projective measurements since it is more biased to 0 and 1.

also display histograms of the different values $P_p(+z)$ for different propagation times of $E(t)$. As more and more information is included, the retrodiction is more biased towards 0 or 1 in the histogram. These show that as information is included in the propagation of E the retrodictions become more confident.

4.3.3 Smoothed prediction of projective measurements

In this section, we show how we make more confident prediction for a projective measurement with further information represented by $E(t)$ using the PQS theory compared the prediction only made by $\rho(t)$. In Figure 4.7, we display histograms of $P(+z)$ and $P_P(+z)$, representing the predicted and smoothed probability for finding the qubit in its ground state. We observe more occurrences of values of $P_P(+z)$ than of $P(+z)$ near 0 and 1 indicating that the past quantum state makes more confident predictions about the outcome of a projective measurement. When $\Omega_R = 0$ the more confident predictions given by the past quantum state are a consequence of the quantum non-demolition (QND) character of the measurement. Because the effects of the measurements commute and the past quantum state analysis merely accumulates measurements in the intervals (0, t) and (t + Δt, T). However, by setting $\Omega_R \neq 0$,

we break the QND character of the measurement, and it is necessary to propagate ρ and E using their associated stochastic master equations.

4.4 Applications of our experiment

In this section, I will give three applications of our experiment in the context of continuous weak measurement by employing the PQS theory and the quantum trajectory theory. First, the PQS theory can be used to retrodict the measurement outcome in the past using the future information which might be useful for state preparation and readout. Second, we observe weak values in the continuous weak measurement in our experiment. Third, our experiment is a good platform to study time symmetry.

4.4.1 State preparation and readout fidelity

The first application of our experiment is to improve the state preparation and readout fidelity. The experimental sequence is shown in Figure 4.8: we first use a herald measurement to prepare the initial state, and then immediately perform a strong projective measurement M. After the measurement, the qubit is subject to continuous weak measurement and Rabi drive. Due to the thermal population, spurious transitions or other reasons, the preparation fidelity is finite. In our case, we have a preparation fidelity of 96% for $-z$ and 97% for $+z$, resulting in imperfect state preparation. Here we use Eq.(4.9) to propagate $E(t)$ backward from T with the continuous measurement record to make retrodiction for the measurement M to test the state preparation. In Figure 4.8 we show the retrodictions that are made for initial states that are prepared in $+z$ and $-z$. The majority of the retrodictions give values $P_P(+z)$ near 0 or 1, yet some give retrodictions for the initial state between 0 and 1 and these retrodictions are verified by examining the outcomes of measurements M that yielded similar values of E_0. In Figure 4.8, we can see that the PQS "knows" when the error occurs. Therefore, we might use the PQS theory to improve the fidelity for the state preparation and readout.

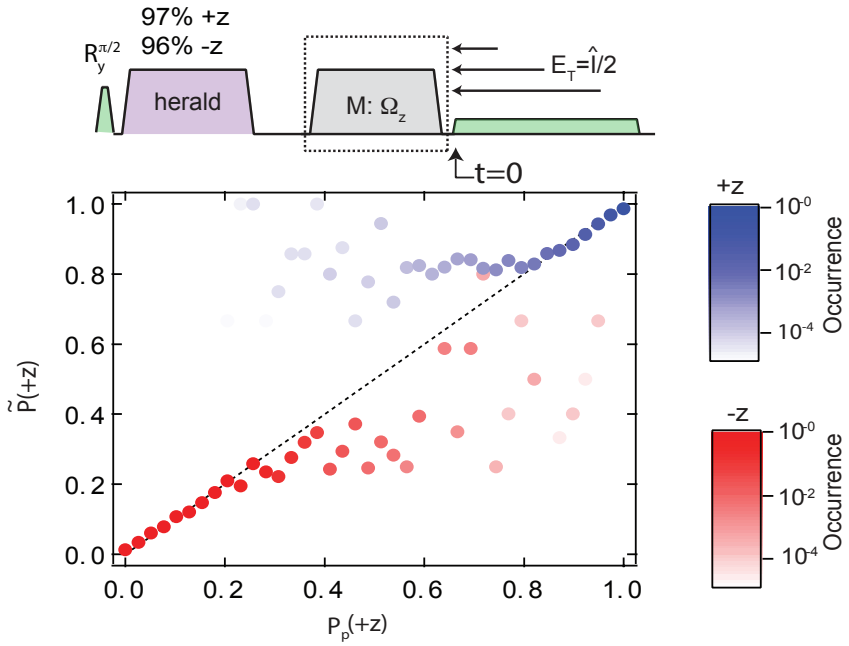

Figure 4.8: Retrodiction for initial states ρ_0. We prepare different initial states $\mathrm{Tr}(\rho\sigma_z) = \pm 1$ with a herald measurement, however the finite measurement fidelity 96% for $-z$ and 97% for $+z$ results in imperfect state preparation. These fidelities are incorporated into ρ_0, and thus the retrodiction for measurement M. The blue and red markers represent the retrodictions for the ground and excited state respectively.

4.4.2 Weak values

In previous sections, we have shown that we can make predictions for the measurement outcome based on ρ, and the retrodictions based on E. We now illustrate the application of ρ and E to create a smoothed prediction based on both ρ and E for the outcome of a POVM measurement. The POVM measurement that we consider here is associated with the measurement signal between t and $t + \Delta t$ is given by the measurement operators [113, 114],

$$\Omega_V = \left(2\pi a^2\right)^{-1/4} e^{(-(V-\sigma_z)^2/4a^2)} \tag{4.10}$$

where $1/4a^2 = k\eta\Delta t$. The POVM operators Ω_V satisfy $\int \Omega_V^\dagger \Omega_V dV = I$. The probability of the measurement yielding a value V can be given by $P(V) = \mathrm{Tr}(\Omega_V \rho_t \Omega_V^\dagger)$ if we treat ρ_t as a constant during the short time Δt. The probability is the sum of two Gaussian distributions with variance a^2 centered at $+1$ and -1 and weighted by the populations ρ_{00} and ρ_{11} of the two qubit states. In this experiment, the system is also subject to probing and Rabi drive after t. We now test the smoothed predictions for the outcome of the measurement Ω_V based on the information before and after the measurement Ω_V. The probability for the measurement Ω_V conditioned on the density matrix ρ_t and the matrix E_t using the PQS theory can be expressed in terms of their matrix elements,

$$\begin{aligned} P_p(V) \propto & \rho_{00}E_{00}e^{(-(V-1)^2/2a^2)} + \rho_{11}E_{11}e^{(-(V+1)^2/2a^2)} \\ & + (\rho_{10}E_{01} + \rho_{01}E_{10})e^{(-(V^2+1)/2a^2)}. \end{aligned} \tag{4.11}$$

The predicted mean value is simply $\langle V \rangle_p = \int P_p(V) V dV$. After plugging $P_p(V)$ (Eq. (4.11)) into $\langle V \rangle_p$ and normalizing it, we have:

$$\langle V \rangle_p = \frac{(\rho_{00}E_{00} - \rho_{11}E_{11})}{(\rho_{00}E_{00} + \rho_{11}E_{11} + \exp(-\frac{1}{8a^2})(\rho_{10}E_{01} + \rho_{01}E_{10})}. \tag{4.12}$$

Here we note that if the measurement is strong, a is small, and the coherence con-

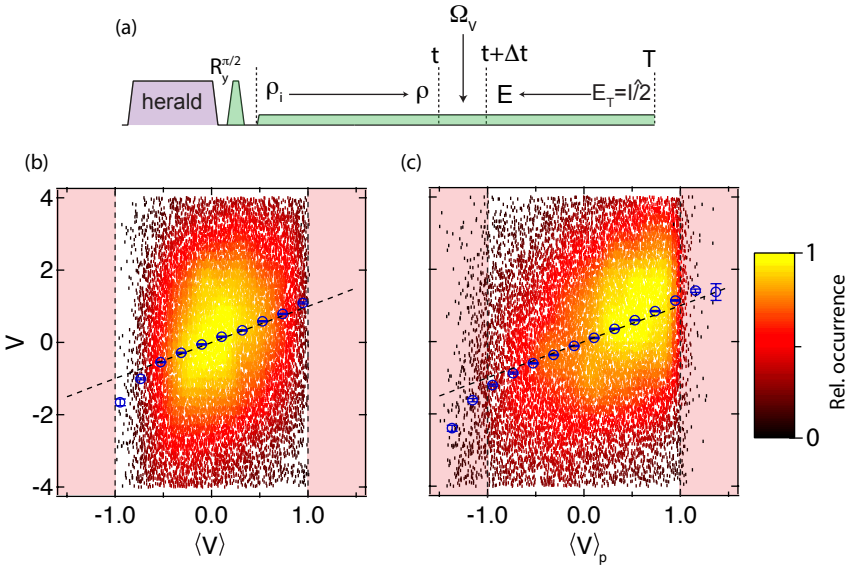

Figure 4.9: Conventional and past quantum state predictions for the measurement Ω_V conducted at time t. (a) The qubit is first initialized along $+x$ and then subject to continuous measurement and Rabi drive. Each experiment yields a value V resulting from the Ω_V measurement. (b,c) The results are dominated by noise, but their conditional average (open circles) is in agreement with the expected mean value given by the dashed line. Panel (b) show the conventional predictions based on ρ while panel (c) shows the PQS predictions based on ρ and E. Note that the prediction based on ρ and E, $\langle V\rangle_p$ makes predictions for the mean value that fall outside of the spectral range of the qubit observable (in the pink region).

tribution proportional to the off-diagonal elements of ρ and E is cancelled in the denominator. The populations of ρ are then effectively modified by the populations of E as suggested by the Aharonov-Bergmann-Lebowitz rule and in agreement with a classical Bayesian argument. In contrast, when the measurement is weak, a single measurement is dominated by noise and reveals only little information (and causes infinitesimal back action). This is the situation that leads to so-called weak values.

Weak values occur in situations with post-selections, if the measurement signal is proportional to an observable $\hat{A}$, and the system is initialized in $|\psi_i\rangle$ and post-selected in state $|\psi_f\rangle$, the mean signal is given by [54, 136],

$$\langle \hat{A}_w \rangle = Re[\frac{\langle \psi_f | \hat{A} | \psi_i \rangle}{\langle \psi_f | \psi_i \rangle}], \tag{4.13}$$

this expectation value conditioned on both initial and final states may differ dramatically from the usual expectation value $\langle \psi_i | \hat{A} | \psi_i \rangle$.

In Figure 4.9, we display results of our experiments that test the predictions of Eq. (4.12). For many iterations of the experiment we choose a measurement time interval, $\Delta t = 180$ ns that is short enough that the effect of the continuous Rabi drive is nearly negligible in the time interval $(t, t + \Delta t)$. Based on 800 ns of probing before, and before *and* after the measurement interval, we calculate $P(V)$ and $P_p(V)$ for the result of the measurement. In Fig. 4.9, we show that both the conventional and the past quantum state formalism yield agrement between the predicted mean value and the measured values. The measured results are noisy, and we plot the data with the predicted average value along the horizontal axes, and the measured values along the vertical axes. The mean value of the measurement results are in good agreement with both the conventional and the past quantum state prediction.

Conventionlly, we have $\langle V \rangle = \langle \sigma_z \rangle$ which never exceeds 1, however, a fraction of the experiments based on both $\rho(t)$ and E lead to the smoothed predictions which sometimes go outside of the boundary and given values $|\langle V \rangle_p| > 1$ [135]. Such anomalous weak values in connection with Eq.(4.13) have been typically identified with the intentional post selection of final states with a very small overlap with the initial state.

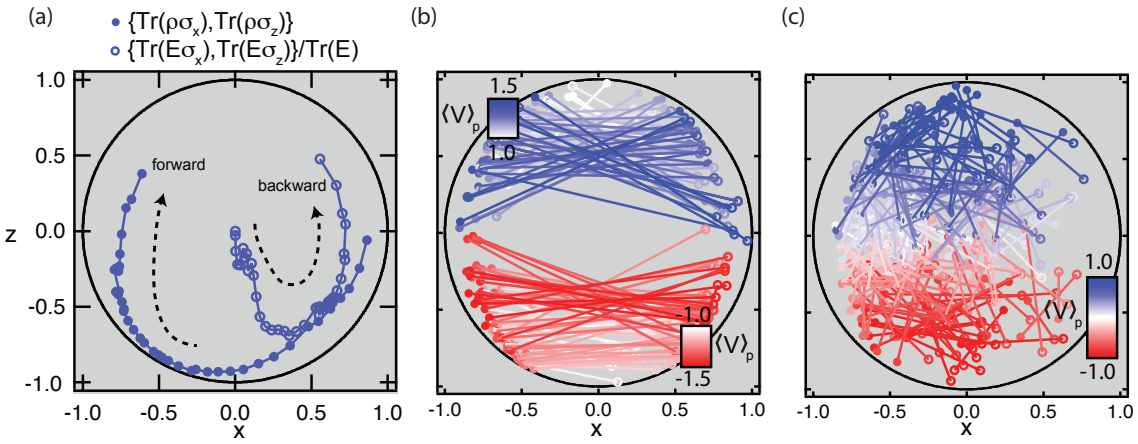

Figure 4.10: Bloch vector representation of the matrix elements of ρ and E. (a) The matrix elements, $\{\mathrm{Tr}(\rho\sigma_x), \mathrm{Tr}(\rho\sigma_z)\}$ (closed circles) and $\frac{1}{\mathrm{Tr}(E)}\{\mathrm{Tr}(E\sigma_x), \mathrm{Tr}(E\sigma_z)\}$ (open circles), are obtained from single trajectories by propagating ρ forward in time and E backward in time. For each iteration of the experiment, a line joins the coordinates. The closed circles represent the state of the system at time t based on ρ_t, and the open circles represent the corresponding quantity based on $E_{t+\Delta t}$. (b) Matrix elements that yield anomalous ($|\langle V\rangle_p| > 1$) predictions. The color indicates the value of $\langle V\rangle_p$ for each pair of states. (c) displays some of the the matrix elements that yield normal predictions ($|\langle V\rangle_p| \leq 1$).

Surprisingly, continuous probing leads to similar effects [135]. In Figure 4.10 we examine the states that lead to different weak value predictions. We represent pairs of ρ and E as connected points on the Bloch sphere, given by $\{\mathrm{Tr}(\rho\sigma_x), \mathrm{Tr}(\rho\sigma_z)\}$, and $\frac{1}{\mathrm{Tr}(E)}\{\mathrm{Tr}(E\sigma_x), \mathrm{Tr}(E\sigma_z)\}$. Indeed, predictions outside the spectral range of the operator are accompanied by near orthogonality of states associated with the matrices ρ_t and E_t. In agreement with the pure state case, large weak values of σ_z do not occur when ρ_t or E_t are close to the σ_z eigenstates, but rather when they are close to opposite σ_x eigenstates, which have near vanishing $\langle\sigma_z\rangle$.

4.5 Conclusion

In this chapter, we have introduced the quantum trajectory theory to calculate the quantum state of a superconducting qubit based on the measurement record of continuous measurements. We showed how we propagate the density matrix $\rho(t)$ forward

in time to make prediction for the outcome of measurements. We have also demonstrated a quantum hindsight effect, where probing of a quantum system modifies and improves the predictions about measurements already performed in the past in the both the continuous weak measurement and projective measurement. When the quantum system is subject to continuous probing and unitary rotations, these predictions are non-trivial, but they can be accounted for by the density matrix and an effect matrix, which assign probabilities to general measurements at any time based on the earlier and later acquisiton of information about the system. These advances may be used to improve the state preparation and readout fidelity for quantum systems and increase their potential for use as probes of time-dependent interactions and parameter estimation [49, 55, 117, 137–140]. With our experimental techniques, we also have access to study weak values and time symmetry problems which might be crucial to understanding foundations in quantum mechanics [130, 141].

Chapter 5

Signal-state correlations in a superconducting qubit

In this chapter, we employ the same dispersive experimental set-up as in Chapter 4 in order to again use weak, continuous measurement to only obtain partial information about the state of the qubit without collapsing it (please refer to the Chapter 4 section 1 to see the details of the experiment which includes the experiment set-up and other experiment parameters). We further explore the evolution of the system due to the back-action, e.g. studying some of the characteristic properties of this system such as time symmetry of the pre- and post-selected average measurement signals, and correlation between the qubit state and measurement signals. It is well known that projective measurements collapse the qubit to one of its eigenstates, suggesting the direction of time. However, in the weak continuous measurement, the process of measurement does not necessarily clearly indicate an arrow of time. In this experiment, we use continuous weak measurement to examine the aspect of time symmetry in a superconducting qubit without collapsing the qubit state during the measurement. Moreover, we observed the temporal correlation between qubit state and measurement signals in this system which is crucial in developing quantum optics and revealing quantum effects [130, 131, 134, 142–144]. Some of the results seem surprising but we will give our careful explanation on them in the following sections. The results discussed in this chapter have been published in N. Foroozani

et al. Phys. Rev. Lett. **116**, 110401 (2016).

5.1 Pre-selected average of the measurement signals and trajectories

In this section, we are going to first briefly revisit the theory of POVMs and then present the experiment's result showing that the damped Rabi oscillation of the pre-selected average signal is due to the dephasing of the qubit state.

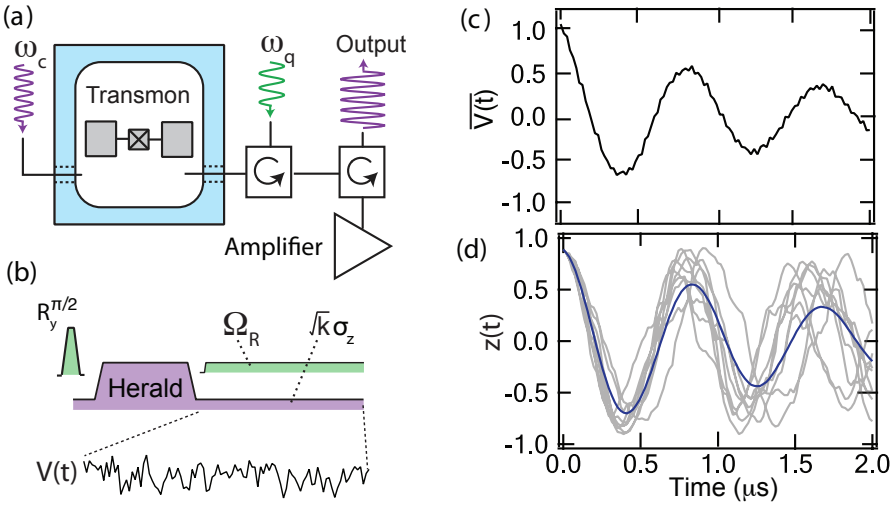

Figure 5.1: Preselected average signals and trajectories. (a) Experimental setup: A transmon qubit is dispersively coupled to a 3D cavity, and the signal reflected from the cavity is amplified by a quantum-limited Josephson Amplifier. (b) Experimental sequences and parameters: the qubit is subjected to continuous measurement and Rabi driven with a Rabi frequency $\Omega_R/2\pi = 1.16$ MHz after its heralded preparation in $+z$ or $-z$. The probe is given by the measurement operator $\sqrt{k}\sigma_z$, where $k = 4\chi^2\bar{n}/\kappa$, parametrizes the measurement strength ($k/2\pi = 95$ kHz) and $\eta = 0.35$ is the quantum measurement efficiency. (c) Pre-selected average measurement signals are caculated by averaging many run of the experiment trace $V(t)$ with the same initial state $+z$. (d) Quantum trajectories starting in the $+z$ state (gray lines) and their mean value (blue line), which is in agreement with the mean signal shown in the upper panel.

The weak and strong measurements of this experiment can both be described by the POVM operator Ω_V which satisfies $\int \Omega_V^\dagger \Omega_V dV = I$, as discussed in the last

chapter [61, 113, 114].

$$\Omega_V = (2\pi a^2)^{-1/4} e^{-(V-\sigma_z)^2/4a^2}. \tag{5.1}$$

Based on the theory of POVMs, the probability for the measurement outcome at time t associated with a homodyne voltage V is given by $P(V_t) = \mathrm{Tr}(\Omega_V \rho_t \Omega_V^\dagger)$. After plugging the density matrix into the above expression, we obtain the probability for the measurement outcome which is the sum of two Gaussians centered at $V = \pm 1$ and weighted by the density matrix components ρ_t^{00} and ρ_t^{11}. From the Eq. (5.1), we know that the variance a^2 determines the strength of the measurements. For example, we can perform a strong projective measurement by decreasing a^2 to the extent that the measurement outcome unambiguously belongs to one of the two disjoint Gaussian distributions. On the other hand, if we have large variance a^2, $P(V)$ can be approximated by a single Gaussian distribution centered at the expectation value of σ_z, $P(V) \simeq (2\pi a^2)^{-1/2} e^{-(V-\langle\sigma_z\rangle)^2/2a^2}$. Therefore, for the weak measurement, the measurement signal V provides a noisy estimate of $\langle\sigma_z\rangle$.

Next, we describe an experiment which is illustrated by the experimental sequence in Fig. 5.1(b), to obtain the pre-selected average homodyne signals. We first prepare the qubit in a superposition $|+x\rangle$ state by applying a $\pi/2$ pulse along the y axis and then perfom a projective measurement $\Omega_{\pm z}$ to herald the qubit in the ground state $+z$ as initial state (We can also prepare other initial states simply by applying a rotation pulse following with or without projective measurement). After the initial state preparation, the qubit is subject to Rabi drive given by $H_\mathrm{R} = \hbar\Omega_R\sigma_y/2$, where $\Omega_R/2\pi = 1.16$ MHz is the Rabi frequency, and continuous weak measurements given by the operators Ω_V.

In Fig. 5.1(c), we display the pre-selected average signal which is obtained by averaging many runs of the signal trace $V(t)$ with the same initial state $+z$. We can see that the average signal $\overline{V}(t)$ undergoes damped Rabi oscillations which correspond to the gradual dephasing of the qubit due to the measurement interaction.

We can also calculate single trajectories by solving the stochastic master equation

for the density matrix $\rho(t)$ (in Chapter 4, Section 2) with the measurement signal $V(t)$ and then obtain the qubit expectation value, $z_i(t) = \mathrm{Tr}(\rho_i(t)\sigma_z)$ [61, 113]. Note that these trajectories start at the same initial state $+z$ for the purpose of comparison with the pre-selected average signals. In Fig. 5.1(d), we show an ensemble of trajectories with the same initial state but dephasing in this ensemble. If we average many runs of these trajectories, we also get the damped Rabi oscillations. This confirms that the damping of the pre-selected average measurement signal is due to dephasing of the ensemble trajectories (the qubit state).

5.2 Post-selected and weighted average of the measurement signals

In this section, we first show the post-selected average signal exhibits an oscillatory signal that is damped *backwards* in time [145]. Then we will show the post-selected average signal agrees well with the weighted average signal based on the density matrix $\rho(t)$ at final time T. At the end of this section, we will give a simple explanation on why these two agree with each other.

Here we perform an experiment illustrated by the experimental sequence in Fig. 5.2. We simply use a projective measurement to readout the qubit state at the end of the experiment and select the $+z$ state. In Fig. 5.2(a), the black curve is the post-selected average of the measurement signals conditioned on the post-selected state $+z$ at the final time $t = T$, which exhibits an oscillatory signal that is damped *backwards* in time [146]. At this point, you may find that the post-selected average signal is the time reverse of the pre-selected average signal shown in Fig. 5.1(c), which exhibits the same full contrast at the final time $t = T$ as the pre-selected average signal at $t = 0$.

In the previous section, we learned that the the pre-selected average signal can be recovered by average many runs of the trajectories starting from the same pre-selected state. For the post-selected average signal, we also want to see if it can be recovered from the trajectories. We consider a sample of the trajectories $z_i(t)$,

which are propagated forward by employing the stochastic master equation of the last chapter. In this case, we consider the ensemble that has a roughly equal number of the trajectories which are initially detected in the $+z$ and $-z$ states since the post-selected signal $\overline{V}_{\rm PS}(t) = 0$ at time $t = 0$. As shown in Fig. 5.2(b) immediately prior to the post-selection, the trajectories end in different values of $z_i(T)$ in a range from $+1$ to -1 , and thus it may be hard to understand why the post-selected average measurement signal (black curve in Fig. 5.2(a)) exhibits full contrast oscillations at the end of the sequence because we cannot recover the black curve by averaging this ensemble of trajectories. However, we will show that the same behavior can be also obtained by weighting the measurement signal with $\rho_i(T)$ at the final time T.

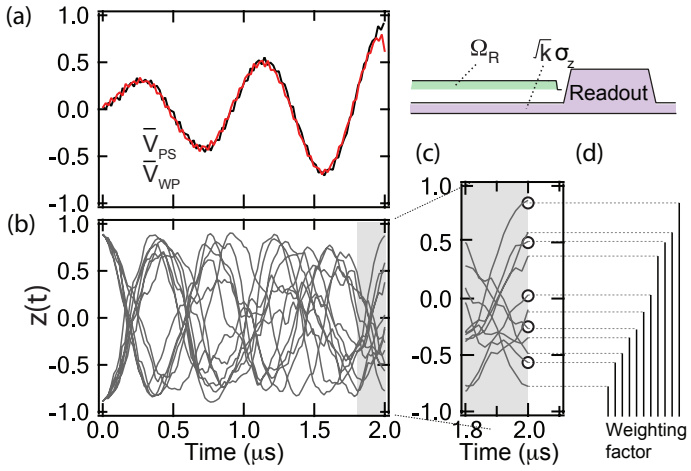

Figure 5.2: Weighted and post-selected average signals. (a) The post-selected average measurement signals (black curve) and the weighted average measurement signal (red curve) show the Rabi oscillations damp backward in time from the final time T. (b) The quantum trajectories that are used to recover the weighted averages in (a) are shown as $z_i(t)$ which are obtained by propagating the stochastic master equation forward in time from the initial states $+z$ and $-z$ with the same quantities. (c) The magnified view of the last time segment shows that the trajectories populate the qubit eigenstates very differently. Trajectories that are post-selected in the $+z$ state are indicated with the open circles. The measurement signals V_i corresponding to this sub-ensemble form the average $\overline{V}_{\rm PS}$. (d) The vertical bars indicate the relative weighting factor that used to calculate $\overline{V}_{\rm WP}$.

We have shown that we can propagate the density matrix $\rho(t)$ forward by using the stochastic master equation with the measurement signals to obtain single trajectories which are display in Fig. 5.2(b). For every run of the experiment, we have one signal trace which can be used to infer the $\rho_i(t)$ of the time dependent conditioned density

matrix of the qubit. Therefore, we can use the the probability $P(i,+z) = \rho_i^{00}(T)$ of being in the ground state at final time T to weight its corresponding signal trace $V_i(t)$. We have the following formula for calculating the weighted signals,

$$\overline{V}_{\mathrm{WP}} = \frac{\sum_i \rho_i^{00}(T) V_i(t)}{\sum_i \rho_i^{00}(T)}. \tag{5.2}$$

In Fig. 5.2(d), we display the weighting factors using the vertical bars which provides the information on the relative contribution of each of the signals to the average. The weighted average is the red curve shown in Fig. 5.2(a) which agrees well with the post-selected average signals (Black curve in Fig. 5.2(a)).

In order to carefully explain the equivalence between the post-selected and the weighted average signals, we note that the post-selected average value can be written in the following formula,

$$\overline{V}_{\mathrm{PS}} = \frac{\sum_i n_i V_i(t)}{\sum_i n_i}, \tag{5.3}$$

where $n_i = 0, 1$ represents the state of the post-selection being excited and ground respectively for the i^{th} measurement signal trace of the ensemble. By comparing the Eq. (5.2) and Eq. (5.3), we can learn that the equivalence can be achieved for large numbers of the measurement signal traces in the ensemble since $\sum_i n_i V_i(t)$ and $\sum_i n_i$ approaches $\sum_i \rho_i^{00}(T) V_i(t)$ and $\sum_i \rho_i^{00}(T)$ respectively for this large limit. Therefore, we have $\overline{V}_{WP} = \overline{V}_{PS}$ which can be understood by the fact that the individual trajectories can faithfully predict the probability of the post-selected state.

5.3 Symmetry between pre- and post-selected average of the measurement signals

The symmetry between pre- and post-selected averaging is interesting because the continuous measurement and the projective measurement should substantially alter the dynamics. To explain this symmetry, we need to consider the joint probability $P(V_t, \pm z_T)$ for the measurement outcome with signal V_t at time t and a projective

measurement on $\pm z_T$ at final time T since the pre- and post-selected average signal can be obtained from the integration $\int V P(V_t, \pm z_T) dV$. This joint probability can be expressed as the product of the probability for the first measurement outcome $P(V_t)$ and the conditional probability $P(\pm z_T | V_t)$,

$$P(V_t, \pm z_T) = P(V_t) \cdot \mathrm{Tr}\{e^{L(T-t)}[\frac{\Omega_V \rho \Omega_V^\dagger}{P(V_t)}] | \pm z\rangle\langle \pm z|\}, \tag{5.4}$$

where ρ represents the state prior to the weak measurement of V_t, $\Omega_V \rho \Omega_V^\dagger / P(V_t)$ yields the normalized state conditioned on the outcome V_t, and $e^{L(T-t)}$ denotes the linear propagator from time t to T of the density matrix according to the determinstic master equation for ρ.

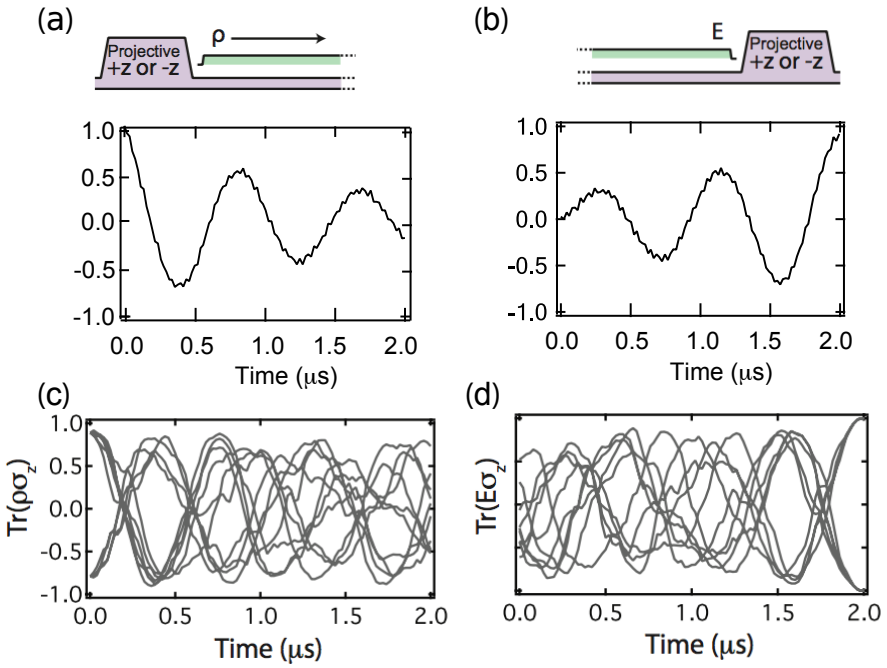

Figure 5.3: Time symmetry in quantum measurement. (a, b) The pre- and post-selected average measurement signals initially in the ground state (black curves). (c, d) Trajectories that are pre- and post-selected in the $+z$ and $-z$ states.

In this case, we can express the evolution from time t to T given by deterministic master equation as a Kraus map, $e^{L(T-t)}[\rho] = \sum_\alpha K_\alpha \rho K_\alpha^\dagger$, with operators satisfying $\sum_\alpha K_\alpha^\dagger K_\alpha = I$ [147, 148]. Using the cyclic properties of the trace, we can move the

Kraus operators K_α to the right hand side of the expression (5.4), and obtain this expression,

$$P(V_t, \pm z_T) \;=\; \mathrm{Tr}\{\Omega_V \rho(t) \Omega_V^\dagger \sum_\alpha K_\alpha^\dagger |\pm z\rangle\langle \pm z| K_\alpha\} \;=\; \mathrm{Tr}[\Omega_V \rho(t) \Omega_V^\dagger E(t)], \quad (5.5)$$

where we define $E(t) = \sum_\alpha K_\alpha^\dagger |\pm z\rangle\langle \pm z| K_\alpha\}$. In our calculation, we do not need the explicit form for the Kraus operators since $E(t)$ can be obtained by solving the following master equation backwards in time with a final state $E(T) = |\pm z\rangle\langle \pm z|$ from T to t.

$$\frac{dE}{d(-t)} = \frac{-1}{i\hbar}[H_R, E] + k(\sigma_z E \sigma_z - E), \quad (5.6)$$

To obtain the pre- or post-selected average signal, we can set $E(t) = I$ or $\rho(t) = I$ in the Eq. (5.5) and then plug the $P(V_t, \pm z_T)$ into the integration $\int V P(V_t, \pm z_T) dV$. For example, to calculate the pre-selected average signal, if we do not condition on the final projective measurement then we simply set $E(t) = I$ in the Eq. (5.5), and obtain the usual prediction, $\overline{V} = \langle \sigma_z \rangle = \rho^{00}(t) - \rho^{11}(t)$. On the other hand, if we post-select the state in the ground state and set $\rho(t) = I$ the Eq. (5.5) then we obtain the predicted measurement signal for post-selection $\overline{V}_{\mathrm{PS}} = E^{00}(t) - E^{11}(t)$.

In Fig. 5.3, the sequence shows how the qubit is prepared in the ground state $+z$ and then followed by continuous weak measurement and Rabi drive. We simply average the weak signal from many runs of the experiment. As expected, we can see the damped Rabi oscillation. We can track the evolution of the quantum state by calculating the trajectory for a density matrix. For separate iterations of the experiment, the trajectories behave differently. If we post-select the qubit state in ground $+z$ state and average the weak signal, then we see the Rabi oscillations decay backwards in time. We can also consider the evolution of backwards propagated trajectories, given by the matrix E. Thus from the pre- and post-selected average signal or the forward and backward trajectories, these results give identical heralded predictions for the average measurement signal explain the time symmetry of the pre- and post-selected average signal.

5.4 The temporal correlation between the measurement signal and qubit state

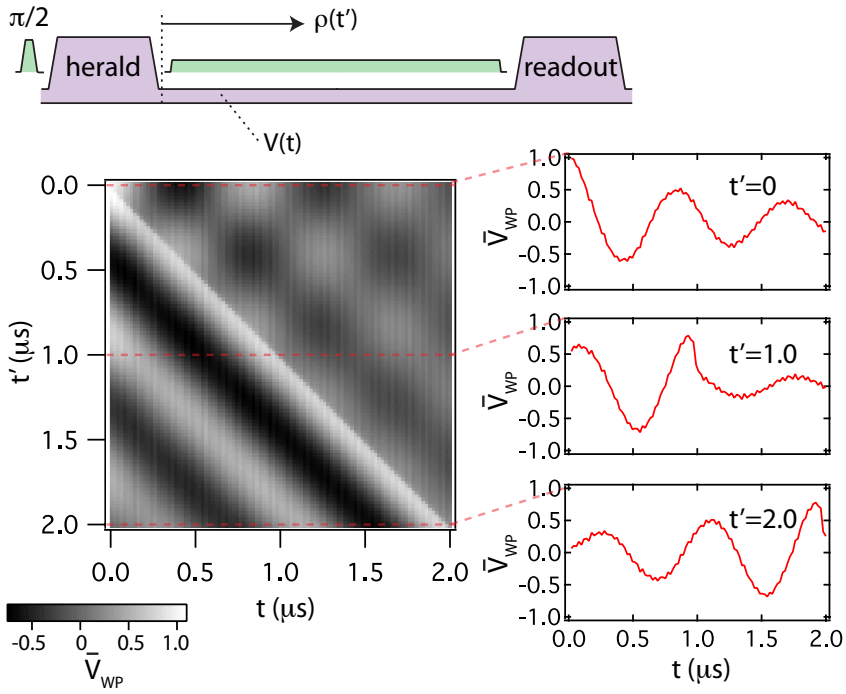

Figure 5.4: Two-time correlation function between the measurement signal $V_i(t)$ and the inferred qubit density matrix element $\rho_i^{00}(t')$. The top show the experiment sequence we run to obtain the measurement signal $V_i(t)$. The red curves in the side panels show the correlations as function of t for $t' = 0, 1\mu s, 2\mu s$ which are the cuts indicated in the 2D graph.

In the previous section, we showed that the predictions for the post-selected or weighted averages can reflect the correlation between the qubit observables at different times and believe such correlations are important in the quantum physics [149–152]. To further study the temporal correlations between the measurement signals and the inferred qubit density matrix, we modify the Eq. (5.2) by incorporating a dummy time t' to get the two time correlation function,

$$\overline{V}_{WP}(t,t') = \frac{\sum_i \rho_i^{00}(t')V_i(t)}{\sum_i \rho_i^{00}(t')}. \tag{5.7}$$

The above expression is an average over all the runs of the experimental measurement signal $V_i(t)$ at time t which is weighted by the qubit state $\rho_i^{00}(t')$ at time t' . In Fig. 5.4, we display the temporal correlation function between the measured signal and the qubit state for both t and t'. The 2D graph shows $\overline{V}_{WP}(t,t')$ as a function of t between 0 and T for values of t' ($t' \in [0, 2\mu s]$). In this graph, we can see the weighted average signals show very different behavior in two regions. This difference in the two regions suggests a different correlation regime before and after t'. The reason for these different behaviors is that $V_i(t)$ is the sum of a term proportional to $\langle\sigma_z\rangle$ and a white noise term $W(t)$. When $t < t'$, the noise term $W(t)$ contributes the state update based on the SME thus it affects all later values of $\rho_i^{00}(t')$. For $t > t'$, $W(t)$ is uncorrelated with the earlier state $\rho_i^{00}(t')$ due to its stochastic nature, and hence it averages to zero in the sum over i in Eq. (5.7).

For $t < t'$, we can obtain $\overline{V}_{WP}(t,t')$ by averaging many runs of the signal trace by post-selecting the final state for the corresponding ensemble of different post-selection times $T = t'$. Since $\overline{V}_{\rm PS} = \overline{V}_{\rm WP}$ for large number of the measurement signal trace with post-selection in the ensemble, using the Eq. (5.5), we can also calculate this average signal even without any post-selection performed at time t' simply by propagating $E(t)$ backwards from the state $|+z\rangle\langle+z|$ at time t'.

We may utilize a different method to calculate $\overline{V}_{WP}(t,t')$ by using the equalities: $\rho_i^{00}(t') = (\langle\sigma_z(t')\rangle_i+1)/2$, and $V(t') = \langle\sigma_z(t')\rangle+W(t')$, where $W(t')$ has zero mean and is uncorrelated with all previous quantities due to its stochastic property. Therefore, we can write an alternative expression for $\overline{V}_{WP}(t,t')$ for $t < t'$,

$$\overline{V}_{\rm WP}(t,t') = \frac{\overline{V_i(t)V_i(t')} + \overline{V_i(t)}}{\overline{V(t')} + 1}. \tag{5.8}$$

Note that the different expressions for $\overline{V}_{\rm WP}$ are not identical but for large ensembles of measurement records they are the same.

For $t > t'$, the correlation function may be written $\overline{V}_{WP}(t,t') = \frac{\sum_i \rho_i^{00}(t')(2\rho_i^{00}(t)-1)}{\sum_i \rho_i^{00}(t')}$ by plugging the equalities $V(t') = \langle\sigma_z(t')\rangle + W(t') = (2\rho_i^{00}(t) - 1)$ which is correct for large ensembles of experiments. These correlations do not obey any simple deter-

ministic equation, and we have to use the stochastic master equation to calculate the density matrix $\rho^{00}(t)$ and to determine $\overline{\rho^{00}(t')\rho^{00}(t)}$.

5.5 Conclusion

In summary, we observe the time symmetry between the pre- and post-selected average signal and show that this symmetry is due to the forward and backward evolution for $\rho(t)$ and $E(t)$ without time direction in quantum measurement. We study the correlation between the signal and the qubit state and observe two different correlation region where different correlations owing to how noise is incorporated into state update. Our analysis may have application in the precision metrology and parameter estimation with weak measurement and continuous probing [153–155].

Chapter 6

Homodyne detection of post-selected decay

If we excite a quantum system, it will decay to a lower energy state. The process by which a quantum system in an excited state undergoes a transition to a lower energy state is called spontaneous emission [156, 157]. In this process, the probability that the quantum system stays in the excited state at time t is represented by exponential behavior $P(e) = \exp(-\gamma t)$, where γ is the decay rate. Evolution in quantum dynamics is a remarkable phenomena because the mere act of observing changes how the system evolves [158, 159]. For example, if the decay is detected using a photo detector which is sensitive to the energy quanta of the system, the evolution of the quantum system conditioned on the detected photons takes the form of quantum jumps [160]. The exponential behavior can be recovered by averaging the quantum jumps from many runs of the experiment as shown in dashed curve in Figure 6.1(b). If the decay is measured using a detector (Josephson Parametric Amplifier) which is sensitive to the amplitude of the emission field, the state of the quantum system will evolve stochastically in a continuous manner and will diffuse from the excited state to the ground state as shown in Figure 6.1(c) [158]. The state of the emitter is described by stochastic quantum trajectories which are inferred from the random measurement outcome of the detection. In this case we can also recover the exponential behavior by averaging over an ensemble of the stochastic trajectories which is the dashed curve

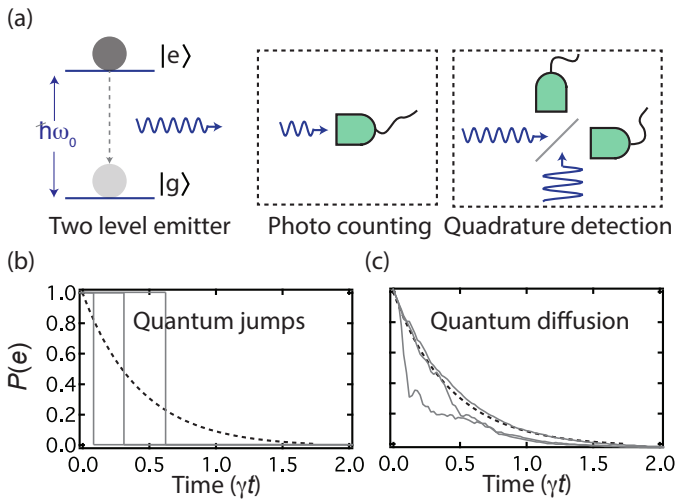

Figure 6.1: Conditional dynamics of radiative decay. (a) The florescence from a two-level emitter radiating at frequency ω_0 can be detected using either photo or quadrature (homodyne) detection. (b) The exponential decay is obtained by averaging detected quantum jumps to the ground state. (c) The exponential decay can be also recovered by averaging many diffusive quantum trajectories.

in Figure 6.1(c). In our experiment, we use homodyne detection by employing the Josephson parametric amplifier (JPA) to monitor the radiative decay of a superconducting qubit which diffuses to the ground state when prepared in an excited state. Using the quantum trajectory theory and PQS theory we can study pre- and post-selected effects. In the following, a simple classical example will illustrate the purpose of this project (how the post-selection affects the decay), and then show we map this example to the quantum world. The results in the chapter are published in D. Tan et. al. Phys. Rev. A **96**. 022104 (2017).

Let's assume that you walked into a room and turned on the light on Monday. The light of the room was working well and you went home at the end of the day, leaving the light on. On Friday, you go into the room and find the light is burned out. The question is what is the probability that the light was burned out on Tuesday (or Wednesday or Thursday) given that you knew that light was working on Monday and on Friday you know it's not working? At this point, you may see that the state of the light (ON or OFF) on Friday matters a lot. If the light is burning, you know the light was working the whole time, but when it is burned out you don't know for sure which

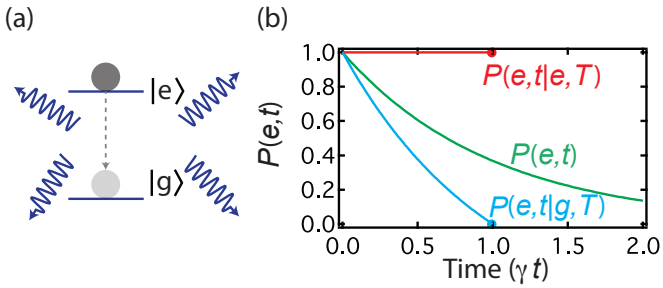

Figure 6.2: Modification of exponential decay with known final states. (a) We consider a two-level system decaying with a rate γ. (b), If the system is initialized in the excited state $|e\rangle$ at $t = 0$, the probability to find the system in the excited state independent of any later information is given by $P(e, t|e, 0) = \exp(-\gamma t)$. However, later knowledge of the state at a final time T alters the excited state probability. The red curve shows $P(e, t|e, T)$ and the blue curve shows $P(e, t|g, T)$ for $T = 1/\gamma$.

day it burned out. This example illustrates how the further knowledge (the state of the light on Friday) affects your knowledge about the state of the system in the past (the state of light between Tuesday and Thursday). This is the kind of guessing game we want to play on the quantum system undergoing radiative decay. The quantum system in this case is called quantum emitter. The question is if we have an emitter in the excited state at time $t = 0$ and we find it in the ground state at later time T, what is the probability that we would find in the excited state previously? How does this depend on the final condition and on the initial condition?

We can answer the questions by employing conditional probabilities [161]. Let's write $P(\alpha, t; g, T)$ as the joint probability that the initially excited system is in state $|\alpha\rangle = |e\rangle$ or $|g\rangle$ at time t and in the ground state at a final time T. We can also write these joint probabilities in terms of the conditional probabilities [161], which are given by $P(e, t; g, T) = P(e, t)P(g, T|e, t) = e^{-\gamma t}(1 - e^{-\gamma(T-t)})$, and $P(g, t; g, T) = P(g, t)P(g, T|g, t) = (1 - e^{-\gamma t}) \times 1$. Based on these joint probabilities, we can obtain the excited state probability at time t which is conditioned on the initial excited state at time $t = 0$ and final ground state at time T from the ratio of the above two joint probabilities,

$$P(e, t|g, T) = \frac{e^{-\gamma t}(1 - e^{-\gamma(T-t)})}{e^{-\gamma t}(1 - e^{-\gamma(T-t)}) + (1 - e^{-\gamma t})}. \tag{6.1}$$

This expression answers the question that we asked in previous paragraphs: how we can make a better guess as to when the light-bulb burned out. The results of the Eq. (6.1) are shown in Figure 6.2(b): the red curve represents the probability that the emitter is in the excited state at time t when found in the excited state at a final time T. In this case the probability is always 1 which makes sense because the emitter should be always in the excited state given that it is still in the excited at later time T. This is the case when the light bulb is still burning on Friday so we know it was always burning on Tuesday through Thursday. The green curve shows the normal exponential decay without any knowledge about the emitter state at time T. The blue curve shows the probability that the emitter is in the excited state at time t when found in the ground state at a final time T which interpolates smoothly between unity at $t = 0$ and zero at $t = T$. Figure 6.2 shows that the probability at time t is significantly modified with further knowledge after time t. Note that the excited state survival probability (6.1) reflects the retrodictions we can make about the system state, i.e., the measurement at time T does not impose the effect of a physical interaction with the system at time t; it updates our present knowledge about it.

In the following sections, we first describe the experimental toolkit. We then present our experimental and theoretical results. Finally, we will present our experimental and theoretical results before discussing its implications.

6.1 Experimental toolkit

In this section, we introduce the experimental set-up, and then show how we calibrate the measurement signals. We also give a detailed description of how this experiment makes particular use of high fidelity post-selection measurements.

6.1.1 Experimental set-up

Our experiment is comprised of an effective two level system which is realized by employing a transmon superconducting qubit in resonance with a 3D aluminum cavity

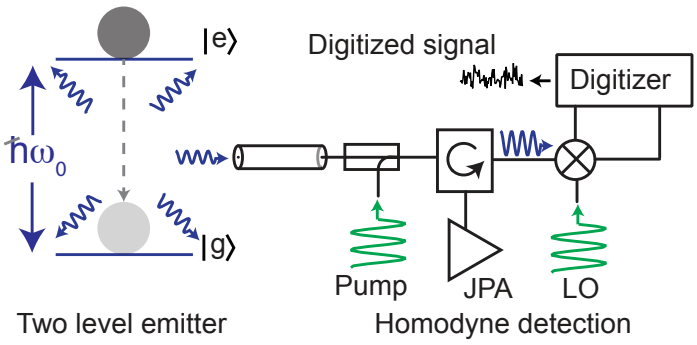

Figure 6.3: Experimental set-up. The florescence from a two-level emitter radiating at frequency ω_0 can be detected using homodyne detection.

[82]. We use the lowest transition as the effective two level system with resonant frequency $\omega_0/2\pi = 6.541$GHz. The effective two level system behaves as a quantum emitter when it is initially prepared in the excited state $|e\rangle$. The emitter is directly connected to a 50 Ω transmission line which results in a Purcell-enhanced radiative decay rate $\gamma = 1.628\ \mu s^{-1}$ [156]. We measure the coherence properties of the emitter using standard techniques and find $T_1 = 614$ ns, $T_2^* = 800$ ns. The interaction Hamiltonian is $H_{\text{int}} \propto (a^\dagger\sigma_- + a\sigma_+)$ which describes the interaction between the emitter and the transmission line, where $a^\dagger(a)$ is the creation (annihilation) operator for a photon in the transmission line, and $\sigma_+(\sigma_-)$ is the pseudo-spin raising (lowering) operator. The outgoing signal which contains the qubit decay information through the transmission line is further amplified by a near-quantum-limited JPA. We use the JPA to perform homodyne detection of the resonance fluorescence from the excited $|e\rangle$ to ground state $|g\rangle$ transition. The homodyne signal is then demodulated and digitized as shown in Figure 6.3. In this experiment, the homodyne measurement signal is proportional to the amplitude of a specific field quadrature, $a^\dagger e^{i\phi} + ae^{-i\phi}$, and due to the interaction Hamiltonian, the measurement results correspond to the emitter dipole $\sigma_- e^{i\phi} + \sigma_+ e^{-i\phi}$. By setting the homodyne phase $\phi = 0$, the resulting homodyne signal is proportional to the $\text{Re}[\sigma_-] = \sigma_x$ [158].

If we prepare the emitter in the ground $|g\rangle$ or excited state $|e\rangle$ and then average 20 ns of the homodyne signal after preparation, the distribution of these homodyne

signals for the ground $|g\rangle$ or excited state $|e\rangle$ overlap with each other and thus cannot be distinguished. This is expected since the homodyne signal is only proportional to σ_x. However, we can calibrate our measurement homodyne signal by applying

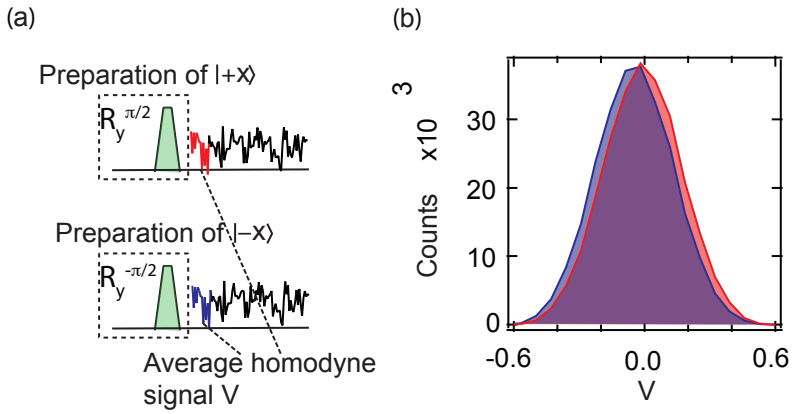

Figure 6.4: Calibration of homodyne signal. (a) Experimental sequences to prepare the emitter in the $|+x\rangle$ and $|-x\rangle$ state. (b) Histograms of the homodyne signal for the $|+x\rangle$ state (red) and $|-x\rangle$ state (blue).

a $R_y^{\frac{\pi}{2}}(R_y^{-\frac{\pi}{2}})$ pulse to prepare the emitter in $|+x\rangle$ or $|-x\rangle$ which is illustrated in Figure 6.4(a). We then average 20 ns of homodyne signal immediately after the state preparation and repeat the experiment 5×10^5 times. This allows us to obtain the distributions for the $|+x\rangle$ and $|-x\rangle$ states. We scale the measurement homodyne signal such that the variance $\sigma^2 = \gamma dt$, where the time step $dt = 20$ ns. Note that this scaling yields a dimensionless signal V, whereas under other conventions have units of $\sqrt{\text{time}}$ [58, 162]. In Figure 6.4(b), we show two histograms with Gaussian distribution centered at $\pm\sqrt{\eta}\gamma dt$ and separated by $\Delta V = 2\sqrt{\eta}\gamma dt$. Hence we can obtain the quantum efficiency of this experiment set-up $\eta = 0.3$ from the above histograms.

6.1.2 High fidelity post-selection measurements

In our typical experiment setup, we can achieve readout out fidelity up to 99% for the ground state and 95% for the excited state. But in this experiment, we would like to obtain the post-selection fidelity as high as possible and have as many successful

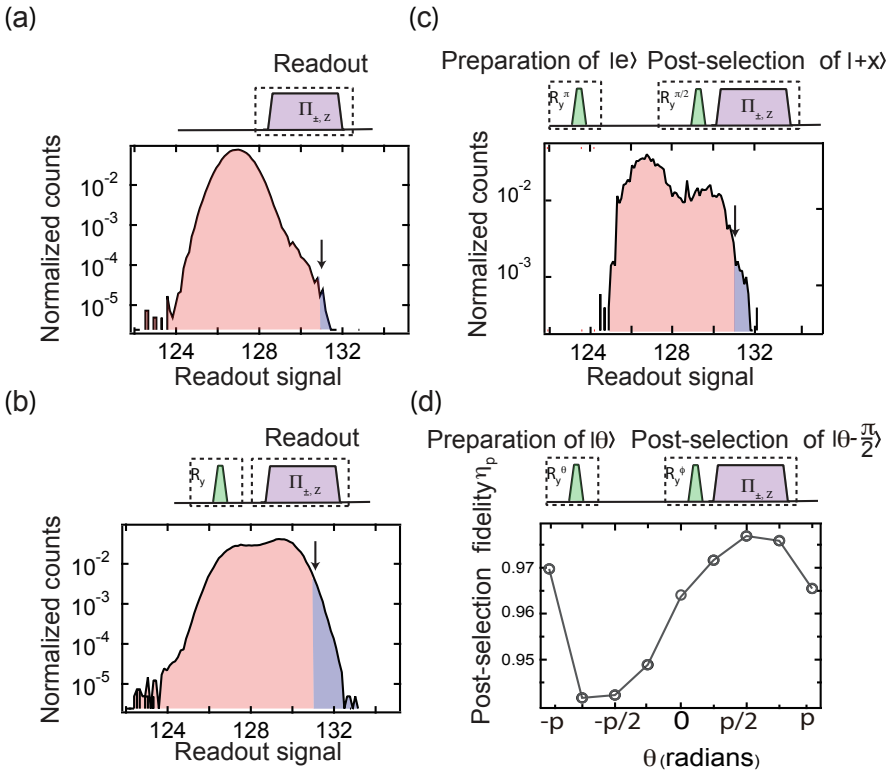

Figure 6.5: Post-selection fidelity. (a) Histogram of the readout when the emitter is in the ground state. The blue region indicates the number of error detections. (b) When the emitter is prepared in the excited state, more post-selections are successful. The histograms in (a) and (b) can be used to determine the post-selection error in our experiment. (c) Histogram of readout when the emitter is prepared in the excited state and post-selected in the $|+x\rangle$ state. (d) The post-selection fidelity for each pair of pre- and post-states ($|\theta\rangle$, $|\theta - \frac{\pi}{2}\rangle$).

runs of post-selection as possible. Because the successful post-selection experiments happen rarely, the data from error post-selection experimental runs can contaminate the measurement results which will give the wrong results. We introduce our method of obtaining high fidelity post-selections by adjusting the readout power to the extent that minimizes the error occurrence while maintaining a modest success rate (ensuring we have modest number of successful post-selection runs). Here we define the post-selection fidelity as the fraction of correct post-selections from the total number of the post-selection experiment runs. In the calibration experiments, we first test the post-selection error rate by preparing the qubit in the ground state followed by a readout measurement. We choose an appropriate threshold with optimal read-

out power (shown as the arrows in Fig. 6.5), to maximize the post-selection fidelity while maintaining a reasonable number of post-selection occurrences. As shown in the histogram of Fig. 6.5(a), we found 2 error occurrences out of 5000 runs of the experiment for the ground state preparation. If we prepare the qubit in the excited state, we have 314 occurrences from the same number of runs with the same threshold. At this point, from these numbers we know the post-selection error rate is below 1% (2/314). Similarly, we can use this post-selection technique for other states by applying a qubit rotation before the readout pulse.

Although the post-selection error rate is below 1% as discussed above, when the post-selection success rate is in the order of 10^{-6}, these relatively low post-selection errors will contaminate the experimental results. This limits our capability to choose the combination of the pre- and post-selected states for our experiments. Here we make our experimental result reliable by choosing certain pre- and post-selected states: ($|\theta\rangle$, $|\theta - \frac{\pi}{2}\rangle$). In this situation, we have achieve the kind of post-selections where the success rate (the ratio of successful runs to total experiment runs), greatly outweighs the error rate. As illustrated in Fig. 6.5(d), the post-selection fidelity for different pre- and post-selected states varies for different θ (mainly due to T_1 decay and calibration of the preparation pulses). In order to obtain the post-selection fidelity as a function of θ, we conduct the experimental sequence showing in Fig. 6.5(d); we first apply a θ pulse to prepare the qubit in the $|\theta\rangle$ state in the x-z plane of the Bloch sphere, after 0.5 μs probing of the qubit evolution we then post-select the $|\theta - \frac{\pi}{2}\rangle$ state by applying a corresponding rotation R_y^{ϕ} and a projective measurement $\Pi_{\pm,z}$. The post-selection fidelity is calculated from the ratio of the correct occurrences to the total trials (which is the difference between the total post-selection occurrence and the error rate $\times$ the number of trials).

6.2 Experimental results

In this section, we show the main experimental results. We first show the probabilities for the excited state are significantly altered with post-selection. We then observe

the anomalous weak values from pre- and post-selection during spontaneous emission. Finally, we will present the evolution of the emitter by employing the Stochastic Master Equation (SME) and the analysis of the deterministic decay curves.

6.2.1 Retrodiction of excited state population

In this section, let's first revisit the PQS theory and SMEs in the case of spontaneous emission, and then we will show how the post-selections alter the probability for the qubit being in the excited state at time t.

As we have already learned in previous chapters, the probabilities for the outcomes of a general measurement M_m conditioned on both ρ_t and E_t, is given by [50]:

$$P_p(m,t) = \frac{\mathrm{Tr}(M_m \rho_t M_m^\dagger E_t)}{\sum_n \mathrm{Tr}(M_n \rho_t M_n^\dagger E_t)}. \tag{6.2}$$

Therefore, it is obvious that we need to know ρ_t and E_t to calculate the probabilities $P_p(m,t)$. We can obtain ρ_t and E_t in two cases: when the quantum system is monitored or un-monitored.

The evolution of the density matrix of an un-observed, decaying two-level quantum system is governed by the deterministic Lindbald master equation,

$$d\rho_t = \gamma \mathcal{D}[\sigma_-]\rho_t dt, \tag{6.3}$$

where $d\rho_t = \rho_t - \rho_{t-dt}$, and $\mathcal{D}[\sigma_-]\rho_t = \sigma_-\rho_t\sigma_+ - \frac{1}{2}\{\sigma_+\sigma_-, \rho_t\}$ is the superoperator for $\sigma_- = (\sigma_x + i\sigma_y)/2$ which describes the decay of the emitter by transferring energy to its surroundings.

The solution of the Eq. (6.3) is given by

$$\begin{aligned} \rho_t^{ee} &= \rho_0^{ee} e^{-\gamma t} \\ \rho_t^{ge} &= \rho_0^{ge} e^{-\frac{\gamma}{2} t} \\ \rho_t^{gg} &= 1 - \rho_0^{ee} e^{-\gamma t}, \end{aligned} \tag{6.4}$$

where $\rho_0 = |\psi_i\rangle\langle\psi_i|$ is the initial state at $t = 0$.

If the emitter is monitored by Homodyne detection with efficiency η, the measurement signal $V = \sqrt{\eta}\gamma \mathrm{Tr}[\sigma_x \rho_t]dt + \sqrt{\gamma}dW_t$ varies according to the σ_x expectation value of the current state ρ_t of the system. The evolution of the monitored quantum emitter is conditioned on the measurement signal and can be described by the stochastic master equation (SME) [113],

$$d\rho_t = \gamma dt \mathcal{D}[\sigma_-]\rho_t + \sqrt{\eta}\left(V - \sqrt{\eta}\gamma \mathrm{Tr}[\sigma_x \rho_t]dt\right)\mathcal{H}[\sigma_-]\rho_t, \tag{6.5}$$

where $\mathcal{H}[\sigma_-]\rho_t = \sigma_-\rho_t + \rho_t\sigma_+ - \mathrm{Tr}[(\sigma_- + \sigma_+)\rho_t]\rho_t$ is the jump superoperator. The second term in the above master equation counts for the stochastic measurement back-action. Similarly, for the effect matrix E_t, when the system is un-monitored, we have the deterministic master equation which describes the backward evolution of E_t from a final time T to t,

$$dE_t = \gamma dt \mathcal{D}^\dagger[\sigma_-]E_t, \tag{6.6}$$

where $dE_t = E_{t-dt} - E_t$. The solution of the Eq. (6.6) is given by

$$\begin{aligned} E_t^{gg} &= E_T^{gg}, \\ E_t^{ge} &= E_T^{ge} e^{-\frac{\gamma}{2}(T-t)}, \\ E_t^{ee} &= E_T^{gg} + (E_T^{ee} - E_T^{gg})e^{-\gamma(T-t)}, \end{aligned} \tag{6.7}$$

where $E_T = |\psi_f\rangle\langle\psi_f|$ is the final state at time T.

If the system is monitored, the effect matrix E_t at time t conditioned on the homodyne signal collected after t can be described by an adjoint counterpart of the Eq. (6.5). The SME for E_t is given by,

$$dE_t = \gamma dt \mathcal{D}^\dagger[\sigma_-]E_t + \sqrt{\eta}\left(V - \sqrt{\eta}\gamma \mathrm{Tr}[\sigma_x E_t]dt\right)\mathcal{H}[\sigma_+]E_t, \tag{6.8}$$

where $\mathcal{D}^\dagger[\sigma_-]E_t = \sigma_+ E_t \sigma_- - \frac{1}{2}\{\sigma_+\sigma_-, E_t\}$. Therefore, we can propagate the above equation backwards from a final time T. Note that Eq. (6.8) does not conserve trace, but this won't affect the value of $P_p(m,t)$ when we use its solution in Eq. (6.8) since Eq. (6.2) itself is normalized.

After obtaining ρ_t and E_t in the un-monitored or monitored case, we show how we calculate the probabilities for the excited state $P_p(e,t)$ at single quantum trajectory level in these cases.

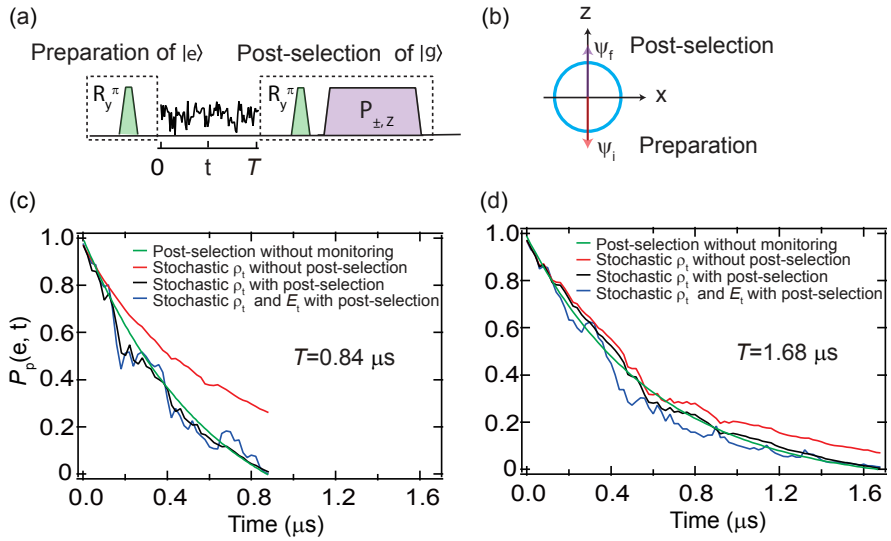

Figure 6.6: Modification of the probability for the excited state by post-selection. (a) Experimental sequence prepares the emitter in the excited state and the homodyne signal is record for a time T followed by a post-selection of the ground state. (b) Bloch representation of the pre-selection of the qubit state $|\psi_i\rangle = |e\rangle$ and post-selection in $|\psi_f\rangle = |g\rangle$. (c, d), The probability of the emitter in the excited state as a function of time for different ground state post-selection times T. The curves in (c, d) are the probability post-selected at time $T = 0.88$ μs and 1.68 μs respectively. The red curves display the probability $P(e,t)$ based only on the density matrix ρ_t calculated from Eq. (6.5) without post-selection. The black curves assume no monitoring after time t by using the deterministic E_t of Eq. (6.13) in Eq. (6.2) to include post-selection. The green curves are the the results without any monitoring. The blue curves are calculated from Eqn. (6.2) where by using the stochastic effect matrix E_t which is determined by Eq. (6.8) we include monitoring for the full duration and post-selection.

In Fig. 6.6(a), we examine the predictions for measuring the qubit in the excited state at a time t given by Eq. (6.2) if the ground state is post-selected at a time T. We first apply a π rotation to prepare the qubit in the excited state and then continuously monitor the evolution for a period of time T. Finally, as described in the last section we apply a high fidelity projective measurement to post-select the ground state using a rotation pulse R_y^π followed by a strong projective measurement. The quantum trajectories, conditioned on the pre- and post-selection as well as on

the homodyne measurement signal, are inferred via Eqs. (6.5, 6.8) by propagating ρ_t forward and E_t backwards to the time t with $\rho_0 = |e\rangle\langle e|$ and $E_T = |g\rangle\langle g|$. We can also calculate the un-monitored, deterministic trajectories with Eqs. (6.4, 6.6). The probability for finding the qubit in the excited state by a projective measurement at time t is $P_p(e,t) = \rho_t^{ee} E_t^{ee}/(\rho_t^{gg} E_t^{gg} + \rho_t^{ee} E_t^{ee})$, which is based on Eq. (6.2) with the POVMs $M_{\pm z} = (\sigma_z \pm 1)/2$. In Fig. 6.6c,d, we display $P_p(e,t)$ for two different post-selection times $T = \{0.88,\ 1.68\}$ μs. We present several different decay curves that incorporate successively more information in the excited state probability. The red curves show how the probability evolves given only the stochastic evolution of ρ_t and neglecting the result of the post-selection, and the green curves indicate the excited state probability based only on the initial preparation and final post-selection without monitoring (as indicated in Fig. 6.2). The black curve indicates the probability based on the stochastic evolution of ρ_t and the final post-selection. Finally, the blue curve represents the most complete prediction for the excited state probability, incorporating both the stochastic evolution of ρ_t and E_t both conditioned on the measurement signal. By including further probing results we get a clearer picture of how spontaneous emission causes a qubit to decay from the excited state to the ground state and we see that the probabilities for an excited state detection in the past is significantly altered when further probing results are incorporated into the prediction.

6.2.2 Retrodiction of the homodyne signal with pre- and post-selection

In this section, we first introduce the theory-predicted average homodye signal using the theory of POVM. Then we describe an experiment to get the average homodyne signal with pre- and post-selections. We find that the theory and experimental results are in good agreement.

The POVM operator associated with the homodyne signal V is given by [113, 114]

$$M_V = \left(\frac{1}{2\pi\gamma dt}\right)^{\frac{1}{4}} \mathrm{e}^{\frac{-V^2}{4\gamma dt}} \left(1 - \frac{\gamma dt}{2}\sigma_+\sigma_- + \sqrt{\eta}\gamma\sigma_- V\right), \tag{6.9}$$

which satisfies $\int M_V^\dagger M_V dV = I$. The probability for the measurement M_V is

$$\begin{aligned} P(V) &= \mathrm{Tr}(M_V \rho_t M_V^\dagger) \\ &= \frac{1}{\sqrt{2\pi\gamma dt}} \exp\left(\frac{-V^2}{2\gamma dt}\right)(1 + \sqrt{\eta}\gamma\langle\sigma_x\rangle V) \\ &\simeq \frac{1}{\sqrt{2\pi\gamma dt}} \exp\left(-\frac{(V - \sqrt{\eta}\gamma\langle\sigma_x\rangle dt)^2}{2\gamma dt}\right), \end{aligned} \tag{6.10}$$

which can be used to calculate the average value, $\overline{V} = \int V P(V) dV = \sqrt{\eta}\gamma\langle\sigma_x\rangle dt$ conditioned only on ρ_t.

Based on the Eq. (6.2), the probability for the measurement signal V conditioned on both ρ_t and E_t can be expressed by

$$P_p(V,t) = \frac{\mathrm{Tr}(M_V \rho_t M_V^\dagger E_t)}{\int dV' \mathrm{Tr}(M_{V'} \rho_t M_{V'}^\dagger E_t)}. \tag{6.11}$$

From this equation we can express the retrodicted mean value $\overline{V}_p(t) = \int V P_p(V,t) dV$ of the homodyne signal by the matrix elements of ρ_t and E_t with pre- and post-selection,

$$\overline{V}_p(t) = \frac{2\sqrt{\eta}\gamma dt(E_t^{gg}\rho_t^{eg} + \rho_t^{ee}E_t^{ge})}{\mathrm{Tr}(\rho_t E_t)} \tag{6.12}$$

Given these theoretical predictions $\overline{V}(t)$ and $\overline{V}_p(t)$, we now describe experiments to verify the theory. We first verify the theoretical average homodyne signal $\overline{V}(t)$ without post-selection. The experimental sequence is illustrated in Figure 6.7a. We use a rotation pulse R_y^θ to prepare the emitter in a state $|\theta\rangle = \cos\frac{\theta}{2}|g\rangle + \sin\frac{\theta}{2}|e\rangle$, and then obtain the average homodyne signal, $\widetilde{V}$, right after the preparation pulse by integrating 60 ns of homodyne signal. The solid lines and dots in Figure 6.7(b) show our experimental results for $\widetilde{V}$ as a function of the preparation pulse rotation angle θ. We can see that the $\widetilde{V}$ oscillates as a function of θ and reaches a maximum

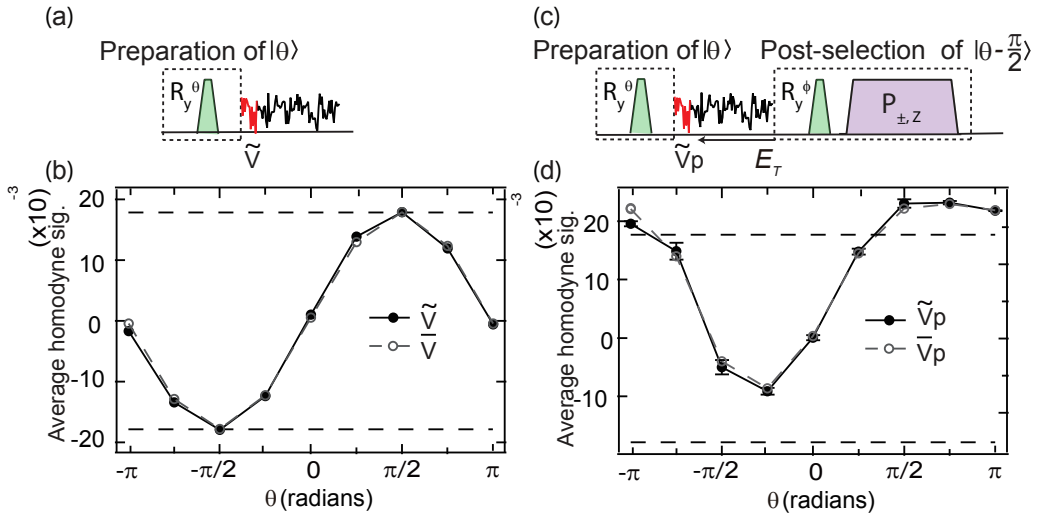

Figure 6.7: Average homodyne signal. (a) The experimental sequence prepares the emitter in a state $|\theta\rangle$ and 60 ns of homodyne signal is integrated to obtain $\widetilde{V}$. (b) Average homodyne signal based on only ρ. The solid line with solid dots is the measured mean homodyne signal without post-selection. The dashed line with hollow dots is the theory-predicted mean value $\overline{V}$. More than 5×10^6 experimental repetitions are used for each $\widetilde{V}$, leading to a statistical uncertainty of order 4×10^{-4}. (c) The experimental sequence prepares the emitter in the state $|\theta\rangle$ and post-selects it in the state $|\theta-\frac{\pi}{2}\rangle$. (d) Average homodyne signal based on ρ and E. The solid line with solid dots is the measured mean homodyne signal for each pair of pre- and post-selected states ($|\theta\rangle$, $|\theta - \frac{\pi}{2}\rangle$). The dashed line with hollow dots is the theory predicted mean value $\overline{V}_p$ as calculated in Eq. (6.12). More than 3×10^4 experimental repetitions are used for each $\widetilde{V}_p$, leading to a statistical uncertainty of order 5.7×10^{-3}. The error bars indicate the standard deviation associated with the drift in the experimental setup from three repetitions of the experiment.

(minimum) at $\theta = \frac{\pi}{2}$ ($\theta = -\frac{\pi}{2}$) as expected [158]. The dashed line with hollow dots is the theoretical predicted average signal $\overline{V}$ which is in good agreement with the experimental results $\widetilde{V}$ which means the experiment is well calibrated. The average homodyne signals $\widetilde{V}$ without post-selection are confined in the region between the dashed horizontal lines $\pm\sqrt{\eta}\gamma dt$ and never exceed this broundary.

Second, we test the theory prediction for the mean signal with post-selection, $\overline{V}_p$. We performed the experimental sequence illustrated in Figure 6.7(c). At time $t = 0$ we prepare the qubit in state $|\theta\rangle$, then collect 0.5 μs of homodyne signal and finally perform a rotation R_y^ϕ followed by a projective measurement to post-select

the state $|\theta - \frac{\pi}{2}\rangle$. We choose these pre- and post-selected states in order to have as many successful post-selected events as possible. The average, post-selected signal $\widetilde{V}_p$ is obtained by averaging 60 ns of homodyne signal right after the initial state preparation pulse from the experimental runs which successfully pre-select state $|\theta\rangle$ and post-select state $|\theta-\frac{\pi}{2}\rangle$. Note that ideally we could obtain the average $\widetilde{V}_p$ by post-selecting state $|\theta - \frac{\pi}{2}\rangle$ immediately after the 60 ns signal integration, but transient behavior associated with the rotations and readout can contaminate the result. This is the reason that we continuously monitor the emitter and record the homodyne signal for 0.5 μs. In this experiment, we consider the average homodyne signal over many experimental runs with the same pre- and post-selected states. Thus we can consider the master equations for ρ_t and E_t without monitoring as shown in Eqs. (6.4, 6.6) and propagate the these equation for E_t backwards to obtain the $\widetilde{V}_p$ using the Eq. (6.12).

In this experiment, we prepare the emitter in the state $|\theta\rangle = \cos(\frac{\theta}{2})|g\rangle + \sin(\frac{\theta}{2})|e\rangle$ at $t = 0$ and post-select it in the state $|\theta - \frac{\pi}{2}\rangle = \cos(\frac{\theta-\frac{\pi}{2}}{2})|g\rangle + \sin(\frac{\theta-\frac{\pi}{2}}{2})|e\rangle$ at $t = T$. Ideally, we have the density matrix $\rho_{t=0}(\theta) = |\theta\rangle\langle\theta|$ and the effect matrix $E_{t=T}(\theta) = |\theta - \frac{\pi}{2}\rangle\langle\theta - \frac{\pi}{2}|$. However, due to the finite post-selection fidelity η_p as shown in Figure 6.5(d), the effect matrix E_T at time T for calculating $\overline{V_p}$ needs to be corrected as follows,

$$\begin{cases} E_T^{gg}(\theta) = (1-\eta_p)\cos^2\left(\frac{\theta-\frac{\pi}{2}-\pi}{2}\right) + \eta_p\cos^2\left(\frac{\theta-\frac{\pi}{2}}{2}\right) \\ E_T^{ge}(\theta) = \frac{1}{2}(1-\eta_p)\sin\left(\theta-\frac{\pi}{2}-\pi\right) + \frac{1}{2}\eta_p\sin\left(\theta-\frac{\pi}{2}\right) \\ E_T^{ee}(\theta) = (1-\eta_p)\sin^2\left(\frac{\theta-\frac{\pi}{2}-\pi}{2}\right) + \eta_p\sin^2\left(\frac{\theta-\frac{\pi}{2}}{2}\right), \end{cases} \tag{6.13}$$

In Figure 6.7(d), after correcting for the post-selection fidelity, it is shown that the experimental results $\widetilde{V}_p$ (solid line with solid dots) agree well with the theory prediction $\overline{V}_p$ (dashed line with hollow dots), which is calculated from Eqs. (6.12, 6.4, 6.6). Moreover, at these places $\theta = \{-\pi, \frac{\pi}{2}, \frac{3\pi}{4}, \pi\}$ we oberve the average homodyne signal $|\widetilde{V}_p|$ exceeds the traditionally allowed maximal value $\sqrt{\eta}\gamma dt$ which are the so-called weak values due to the low overlap between the pre- and post-selected states.

6.3 Quantum trajectories

In this section, we use homodyne detection to continuously monitor the emitter. Since the emitter interacts with the noise environment, the outcome of the detection is random and follows a Gaussian distribution. The state of the emitter, which is conditioned on the noise detection signal, evolves stochastically. In this section, we use the SME method to infer the quantum trajectories of the emitter with pre- and post-selection.

6.3.1 Quantum trajectories based on ρ_t

With these relations $x_\rho = \mathrm{Tr}(\sigma_x \rho_t)$ and $z_\rho = \mathrm{Tr}(\sigma_z \rho_t)$, the SME for the density matrix ρ_t (Eq. (6.5)) can be written to the following equations for the Bloch vector components [163],

$$\begin{aligned} dx_\rho &= -\frac{\gamma}{2} x_\rho dt + \sqrt{\eta}(1 - z_\rho - x_\rho^2)(V - \sqrt{\eta}\gamma x_\rho dt) \\ dz_\rho &= \gamma(1 - z_\rho)dt - \sqrt{\eta}(1 - z_\rho)x_\rho(V - \sqrt{\eta}\gamma x_\rho dt). \end{aligned} \tag{6.14}$$

We describe the following experiment to obtain the quantum trajectories conditioned on the homodyne signal V which are given by the Eq. (6.14). The experimental sequence is illustrated in Fig. 6.8(a), we prepare the emitter in the initial state $|\psi_i\rangle$ (pre-selection), then record homodyne signal for 1.68 μs and finally use a rotation pulse and projective measurement to post-select the emitter in a final state $|\psi_f\rangle$ (post-selection) using a high fidelity projective measurement as discussed in section 6.1.2. We show trajectories based on ρ_t as $(\langle\sigma_x\rangle, \langle\sigma_z\rangle)$ on the x-z plane of the Bloch sphere for different initial states. We use red, green, cyan, and blue colors to represent different evolution time intervals $[0.42n,\ 0.42(n{+}1)]$ μs, $(n = 0, 1, 2, 3)$ of the quantum trajectories. As in the Fig. 6.8, the trajectories diffuse through the Bloch sphere from a pre-selected state to ground state, confined within the Bloch sphere due to finite quantum efficiency. The black solid line is a single quantum trajectory which evolves in the Bloch sphere. The blue dashed lines show that the trajectories fall into different

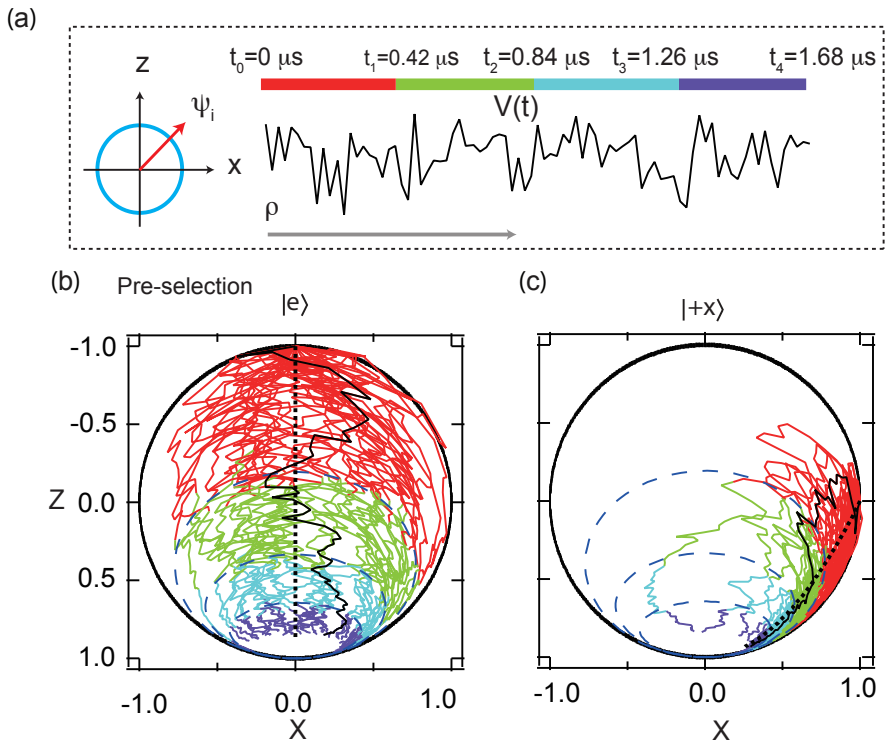

Figure 6.8: Quantum trajectories for pre-selected states. (a), We prepare the qubit in state $|\psi_i\rangle$, and allow the qubit to evolve for 1.68 μs. With the pre-selected state, we propagate the SME forward in time to obtain the quantum trajectories. (b, c, d), Quantum trajectories for different pre-selected states. Note that the Bloch sphere is upside down to put the excited state on top which is slightly more intuitive for our discussion of decay. The black dashed lines show how the unmonitored emitter would evolve deterministically from state $|\psi_i\rangle$ to ground state. The black solid lines represent a single trajectory of the emitter which diffuses stochastically in the Bloch sphere. The blue dashed ellipses illustrate that all the stochastically evolving trajectories are confined to a deterministic region in the Bloch sphere at any given time.

deterministic curves for different evolution times [58, 158].

6.3.2 Quantum trajectories based on E_t

In the previous section, we introduced the SME (6.8) for the effect matrix E_t. Here we also introduce a Bloch sphere representation to illustrate the conditional evolution of the effect matrix E. Since the term $\mathcal{D}^\dagger[\sigma_-]E_t$ in the SME (6.8) is not trace-preserving, an extra term $\gamma dt\mathrm{Tr}(\mathcal{D}^\dagger[\sigma_-]E_t) = \gamma dt\mathrm{Tr}(\sigma_z E_t)$ is added to get the normalized SME

for E_t,

$$dE_t = \gamma dt \mathcal{D}^{\dagger}[\sigma_-]E_t - \gamma dt \mathrm{Tr}[\sigma_z E_t]E_t + \sqrt{\eta}\,(V - \sqrt{\eta}\gamma \mathrm{Tr}[\sigma_x E_t]dt)\,\mathcal{H}[\sigma_+]E_t. \quad (6.15)$$

With the above SME and relations $x_E = \mathrm{Tr}(\sigma_x E_t)$ and $z_E = \mathrm{Tr}(\sigma_z E_t)$, we obtain stochastic master equations of E_t in the form of Bloch components,

$$\begin{aligned} dx_E &= -\frac{\gamma}{2} x_E \left[1 + 2z_E + \eta(1 + z_E - x_E^2)\right] dt + \sqrt{\eta}(1 + z_E - x_E^2)V \\ dz_E &= -\gamma(z_E + z_E^2 - \eta(1 + z_E)x_E^2)dt - \sqrt{\eta}(z_E + 1)x_E V, \end{aligned} \quad (6.16)$$

We conduct experiments with the same sequence in Fig. 6.9a to infer the backwards trajectories based on the above Eq. (6.16). As displayed in the Fig. 6.9(a), we post-select a final state $|\psi_f\rangle$ at the end of the experiment and then we propagate the Eqs (6.16) backwards for 1.68 μs starting with $E_T = |\psi_f\rangle\langle\psi_f|$. The backwards trajectories — which we call retrodicted trajectories — are displayed in the Fig. 6.9, which diffuse backwards in time through the Bloch sphere from the post-selected state. Interestingly, these backwards trajectories are also confined to different determinisitic curves at different times.

6.3.3 Quantum trajectories based on ρ_t and E_t

In previous sections, we have calculated the Bloch components based on ρ_t or E_t which are just the expectation values of the Pauli operators, $u_v(t) = \mathrm{Tr}(\sigma_u v)$ for $u = x, y, z; v = \rho_t, E_t$. These expectation values equal the weighted mean value of their eigenvalues, e.g., $\langle\sigma_u\rangle_v = v^{gg} \cdot 1 + v^{ee} \cdot (-1) = P_v(\sigma_u = +1, t) - P_v(\sigma_u = -1, t)$. Here we want to know how to calculate the Bloch components based on both ρ_t and E_t. The probability for the measurement outcome M_u conditioned on both ρ_t and E_t is given by the Past Quantum State formalism — Eq. (6.2). Similarly, we can obtain the Bloch vector components conditioned on both ρ_t and E_t by adapting the expression of the weighted mean values of the corresponding eigenvalues of the observables,

$$\langle\sigma_u\rangle_p = P_p(\sigma_u = +1, t) - P_p(\sigma_u = -1, t), \quad (6.17)$$

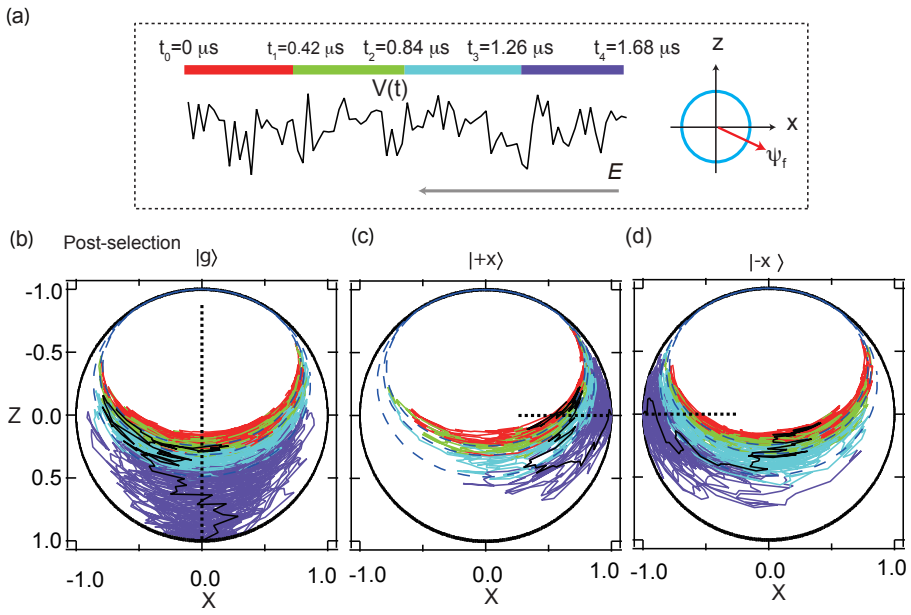

Figure 6.9: Retrodicted trajectories for different post-selected states. (a) The qubit evolves for 1.68 μs and then is post-selected in a final state $|\psi_f\rangle$. (b, c, d) These quantum trajectories are calculated by propagating the stochastic master equations for E_t backwards in time. The trajectories diffuse to the post-selected states and are also confined to a deterministic region in the Bloch sphere at any given time.

here p stands for the Past Quantum state which means the expectation values are conditioned on both ρ and E in this case. We obtain all the Bloch components using Eq. (6.2) and Eq. (6.17) conditioned on the Past Quantum State,

$$\begin{aligned}
\langle\sigma_x\rangle_p &= \frac{x_\rho + x_E}{1 + x_\rho x_E}, \\
\langle\sigma_y\rangle_p &= \frac{y_\rho + y_E}{1 + y_\rho y_E}, \\
\langle\sigma_z\rangle_p &= \frac{z_\rho + z_E}{1 + z_\rho z_E}.
\end{aligned} \tag{6.18}$$

We call the above time-dependent Bloch components smoothed trajectories in connection with our discussion of smoothing in Fig. 1.3. In order to calculate the smoothed trajectories, we propagate the Eq. 6.14 forward in time to obtain the solutions for u_ρ, and propagate the Eq. (6.16) backwards in time to get the solutions for u_E. We use the equation Eq. (6.18) with these solutions from the Eq. (6.14) and Eq. (6.16)

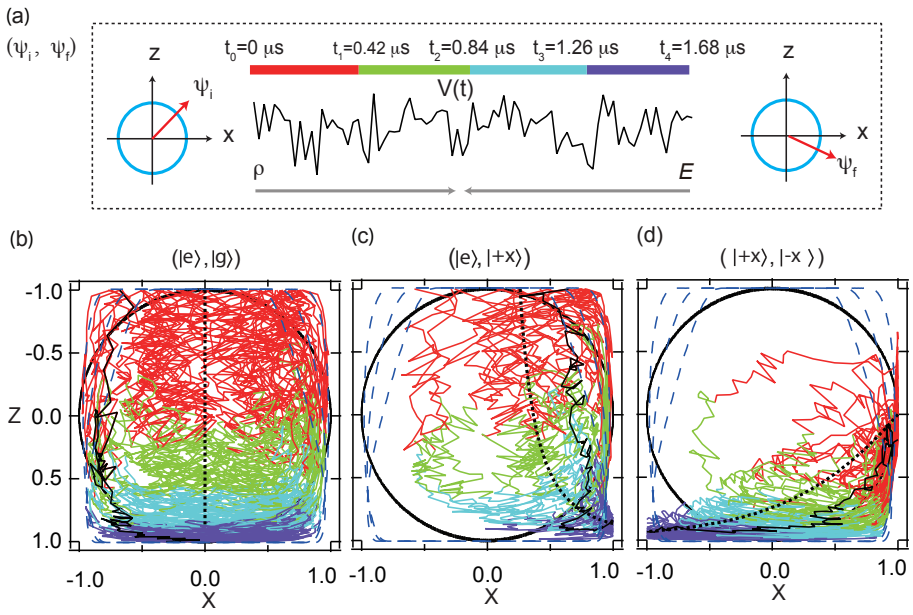

Figure 6.10: Smoothed trajectories for pre- and post-selected states. (a) The qubit is pre-selected the qubit in state $|\psi_i\rangle$, and then evolves for 1.68 μs, finally post-selected in the state $|\psi_f\rangle$. (b, c, d) Smoothed trajectories calculated by the stochastic master equations for different pre- and post-selected states.

to obtain the smoothed trajectories with pre- and post-selected states.

The smoothed trajectories, which are displayed in in Fig. 6.10(b-d), diffuse through the state space. Unlike the trajectories conditioned only on ρ_t or E_t, the retrodiction trajectories clearly have values that are outside of the Bloch sphere instead of in the Bloch sphere. We can understand the results in the following way: in our experiment, the qubit decays almost to the ground state after 1.68 μs. So the probability for the ground state at the end of the sequence with the post-selection is close to unity. If we post-select the qubit in the $+x$ state, the outcome of a final measurement of σ_x would be $+1$ but still need to yield the same results of the prediction for the ground state at that time with $\sigma_z = 1$. In this case, we can have $\sigma_x = 1$ and $\sigma_z = 1$ at the same time. The result seems surprising since the reader may think that it violates the Heisenberg's uncertainty since we cannot measure accurately both σ_x and σ_z at the same time. The fact is that the Heisenberg's uncertainty applies to the prediction for the future measurements, while in these smoothed trajectories we consider the

combination of the prediction and retrodiction of observables and then plug σ_x and σ_z into Eq. (6.18) after calculating σ_x and σ_z conditioned on ρ_t or E_t separately. The Eq. (6.18) is non-linear, so the smoothed predictions are different from the prediction of some spin measurement along an axis between the x and z axes which simply follow from the projection of the Bloch vector along those directions.

6.3.4 Deterministic ellipses for ρ_t and E_t

The theory work in this section was done in close collaboration with our collaborators in Aarhus University. In this section, we show the analysis of how we obtain the deterministic curves. In the following, we first derive the expression of ellipses for the density matrix ρ_t, and then we derive a similar expression of ellipses for the E_t. Finally, we combine the deterministic curves for ρ_t and E_t to obtain the restricted regions for the retrodiction trajectories.

For the density matrix ρ_t, we want to obtain a function $\alpha(x_\rho, z_\rho)$ of the stochastically evolving Bloch components. Moreover, the equation of motion is expected to be deterministic for the Bloch components. Next, we will derive such a function and show that the equation describes an ellipse (deterministic curve) in $x-z$ plane. For a generic function, the equation of motion is derived from the stochastic Bloch equations (6.14),

$$\begin{aligned} d\alpha = &\frac{\partial\alpha}{\partial x_\rho}dx_\rho + \frac{\partial\alpha}{\partial z_\rho}dz_\rho + \\ &+ \frac{1}{2}\left[\frac{\partial^2\alpha}{\partial x_\rho^2}(dx_\rho)^2 + \frac{\partial^2\alpha}{\partial z_\rho^2}(dz_\rho)^2 + 2\frac{\partial^2\alpha}{\partial x_\rho \partial z_\rho}dx_\rho dz_\rho\right], \end{aligned} \tag{6.19}$$

where the second derivatives are due to Itô's formula and accounts for the fact that formally the Wiener increment is defined by the properties $\mathbb{E}[dW_t] = 0$ and $dW_t^2 = dt$ [164], such that when squared the noise terms in Eq. (6.14) yield contributions of the same order in dt as the deterministic terms. The deterministic evolution of $\alpha(x_\rho, z_\rho)$ at different times requires that all terms proportional to dW_t in $d\alpha$ cancel with each other. Therefore, after plugging the Eq. (6.14) in Eq. (6.19) we obtain the following

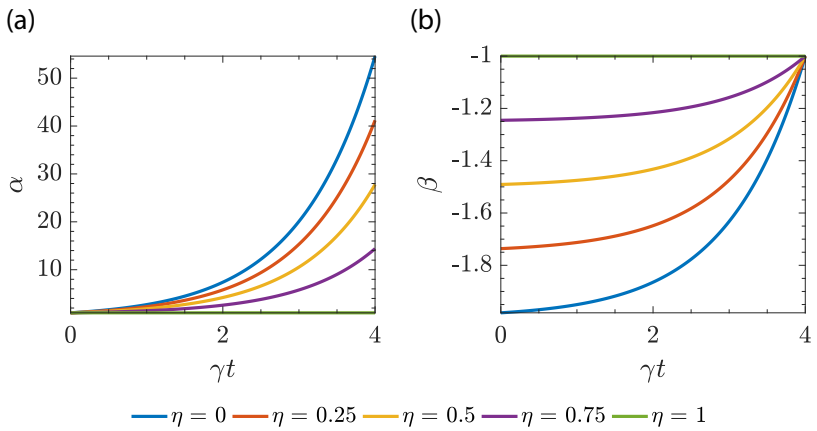

Figure 6.11: Time evolution of functions parametrizing determinstic ellipses. (a) Time evolution given by Eqn. (6.22) of the function $\alpha(x_\rho, z_\rho)$ parametrizing the deterministic ellipse (6.21) in the Bloch sphere on which a decaying spin subject to homodyne detection is confined. (b) Time evolution Eqn. (6.26) of the function $\beta(x_E, z_E)$ for a similar ellipse (6.24) pertaining to the effect matrix and assuming post-selection at time $T = 4\gamma^{-1}$ in a pure state.

form of $\alpha(x_\rho, z_\rho)$,

$$\alpha(x_\rho, z_\rho) = \frac{2}{1 - z_\rho} - \frac{x_\rho^2}{(1 - z_\rho)^2}, \tag{6.20}$$

which can be also expressed in the following form by recombining terms

$$\alpha^2(1 - z_\rho - 1/\alpha)^2 + \alpha x_\rho^2 = 1. \tag{6.21}$$

The above expression has the form of the equation for the ellipse which is centred at $(x, z) = (0, 1-1/\alpha)$ and with major axis $1/\sqrt{\alpha}$ (x_ρ-direction) and minor axis $1/\alpha$ (z_ρ-direction). The ellipse equation tells us that the Bloch components fall into different ellipses curve at different times for all the trajectories conditioned on ρ_t. These ellipse curves are the blue dashed lines which are shown in Fig. 6.8, Fig. 6.9, and Fig. 6.10. To calculate the deterministic curves at different times, we can plug Eq. (6.20) into the right hand side of (6.19) and get the function $\alpha(x_\rho, z_\rho)$ as a function of time which

characterizes the time evolution of the deterministic curves,

$$\alpha(t) = \eta + [\alpha(t=0) - \eta]\mathrm{e}^{\gamma t}, \tag{6.22}$$

where η is the quantum efficiency, γ is the decay rate and $\alpha(t=0)$ follows from (6.20) with the initial Bloch components at time $t = 0$. Eq. (6.20) shows that in the case of pure states $\alpha_0 = 1$ at $t = 0$ so that the ellipses become circles — the full Bloch sphere. In Fig. 6.11(a), we plot the time evolution of $\alpha(t)$ for different values of the quantum efficiency η. The parameter $\alpha(t)$ increases as the increasing t, and hence the center z-coordinate of ellipse increases with a rate γ which is in agreement with the decay of the qubit. In this figure, we can also see that the $\alpha(t)$ at some specific time decreases with increasing quantum efficiency η which means the axes of the ellipse (inverse to $\alpha(t)$) reduces faster for smaller values of the quantum efficiency. Therefore, the qubit is more likely in a variety of mixed states which clearly means the loss of information associated with the non-perfect monitoring. As time increases, the axes of the ellipse reduce and the qubit decays to the ground state.

Similarly, for the effect matrix E_t, we first define a generic function $\beta(x_E, z_E)$ of the Bloch components in (6.16), and then we want to obtain a form of this function which can describe the deterministic evolution for the backwards trajectories conditioned on E_t. The equation of motion for $\beta(x_E, z_E)$ can be obtained after plugging the stochastic Bloch equations (6.16) into Eq. (6.19) just like we did for $\alpha(x_\rho, z_\rho)$, and again requiring all terms proportional to dW_t cancel with each other,

$$\beta(x_E, z_E) = -\frac{2}{z_E + 1} + \frac{x_E^2}{(z_E + 1)^2}. \tag{6.23}$$

Rewriting the above equation we have,

$$1 = \beta^2(z_E + 1 + 1/\beta)^2 - \beta(x_E^2 + y_E^2), \tag{6.24}$$

Similar to the Eq. (6.21), this is again an ellipse equation which is centred at $(x, z) = (0, -(1 + 1/\beta))$ and with major axis $1/\sqrt{-\beta}$ (x_E-direction) and minor axis $1/\beta$ (z_E-

direction). The time evolution of $\beta(x_E, z_E)$ also satisfies the following differential equation,

$$\frac{d\beta}{dt} = \gamma(-\beta + \eta - 2). \tag{6.25}$$

The above equation must be solved backwards in time from the post-selected value at a final time T with $\beta(t = T)$. The solution of the above equation $\beta(x_E, z_E)$ is given by

$$\beta(t) = \eta - 2 + [\beta(T) - \eta + 2]\mathrm{e}^{\gamma(t-T)}. \tag{6.26}$$

From the Eq. (6.23), we know that for any pure post-selected state we have $\beta(t = T) = -1$ and the ellipse is also the full Bloch sphere. In Fig. 6.11(b), we plot the time evolution of β for a final post-selection in a pure state at time $T = 4\gamma^{-1}$ for different quantum efficiency η. The results is similar to what we have in the case of the density matrix: lower quantum efficiency results a faster backwards decay of the ellipse towards a fully mixed effect matrix.

With both deterministic ellipses for ρ and E, we can obtain the restricted area for the retrodicted expectation values of the Bloch components by combining the two ellipses which gives an area in the $((\sigma_x)_p, (\sigma_z)_p)$-plane (Blue dashed curves in Fig. 6.10) from all possible combinations of the points on the two ellipses.

6.3.5 Distribution of Bloch components

In Fig. 6.12, we plot the distributions of the Bloch components x and z for quantum trajectories at different times in order to further study the evolution dynamics of the trajectories. The figure shows histograms of the x and z Bloch components for the trajectories based on ρ, E and (ρ and E) for different pre and post-selections (the three columns in Fig. 6.12) that were studied. The feature from the distribution agrees very well with evolutions of the trajectories in Fig. 6.8, Fig. 6.9, and Fig. 6.10, e.g., for the trajectories based on the density matrix ρ_t, the distributions are getting

close to the $x = 0, z = 1$ (ground state) as the increasing decay time. For the effect matrix E_t, the distributions of the components go towards to the post-selected states $x = 0, 1, -1, z = 1, 0, 0$ respectively. Moreover, we can see that the distributions for the retrodiction trajectories based on both ρ and E are more biased toward the $x, z = \pm 1$ compared to the distributions only based on ρ_t or E_t. This result means that we can make more confident predictions for the outcome of spin component measurements in the past with more information after the measurement.

6.4 Conclusion

In this chapter, we use homodyne detection to continuously monitor the state of a quantum emitter. We first give an analysis showing that the probability for the excited state is modified by the post-selection by applying the Past Quantum State formalism. In the case of spontaneous emission, we experimentally observe the emergence of the weak values by pre- and post-selection and theoretically verify the experiment results. The weak values are due to the small overlap between the pre- and post-selected states and have been shown to offer metrological advantages [165–167]. We study the evolution of the emitter state by employing the stochastic master equation. We find that the the evolution of these trajectories based on ρ_t, E_t and (ρ_t and E_t) is stochastic, but are restricted to deterministic regions in the Bloch sphere.

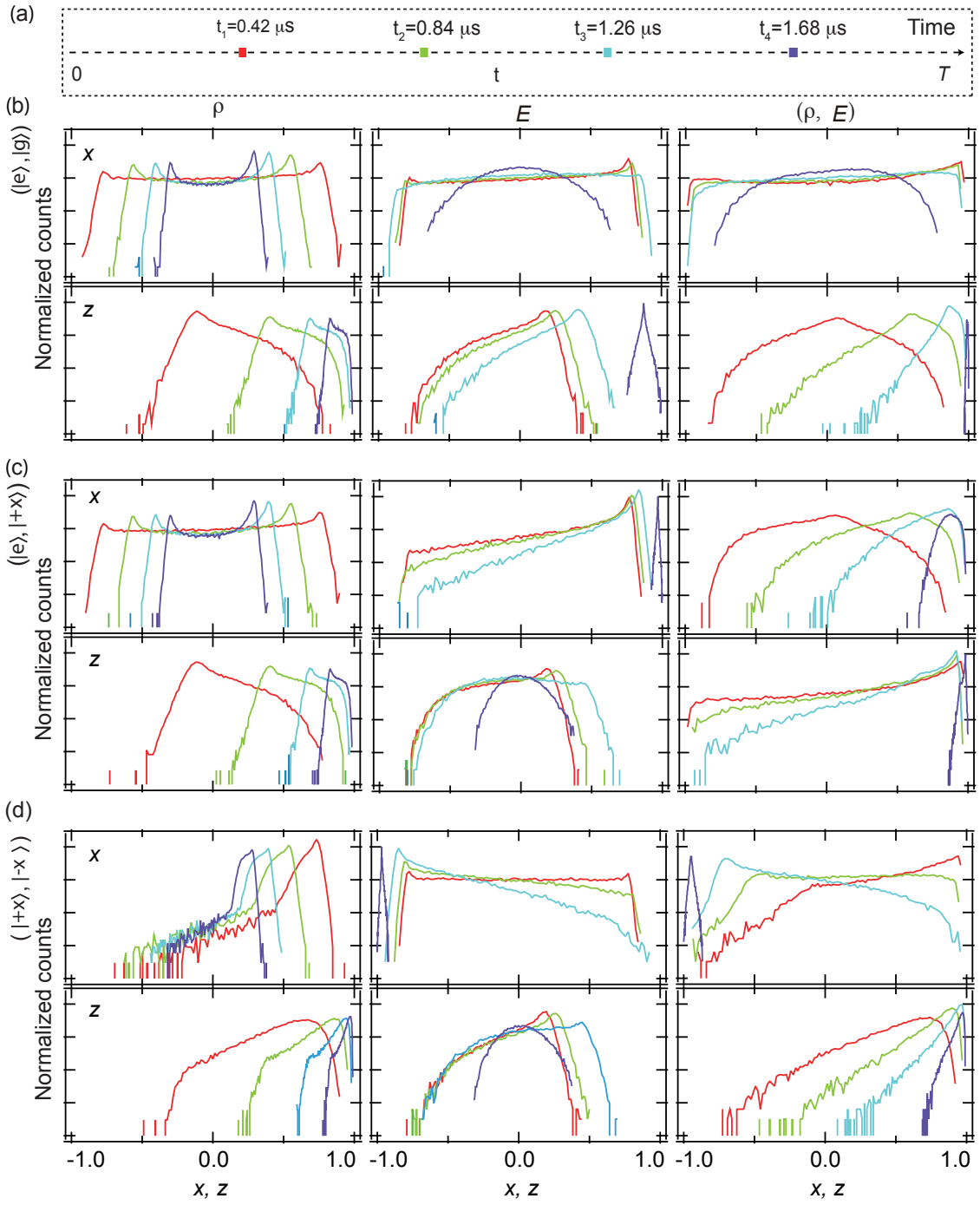

Figure 6.12: Distribution of Bloch components at different times. (a) Time axis showing that at times $t = \{0.42,\ 0.84,\ 1.26,\ 1.68\}\mu$s, we calculate the distributions of x and z components. (b, c, d) Distribution of Bloch components x and z on a logarithmic scale based on ρ, E and (ρ and E) respectively for pre- and post- selected states ($|\psi_i\rangle$, $|\psi_f\rangle$) at different times depicted by corresponding colors in Fig. 6.12(a).

Chapter 7

Conclusions and outlook

7.1 Conclusions

In the work of this thesis, we have verified the past quantum state theory in the context of strong projective measurement and weak measurement by employing a superconducting qubit. With the technique of quantum state tracking, we have demonstrated that the Past Quantum State can make more confident predictions for measurement results, which would be useful for parameter estimations. By applying the Past Quantum State theory, we observed some interesting pre- and post-selected effects of a quantum system such as weak values which is definitely helpful in understanding the foundations of quantum mechanics.

7.2 Tomography for E

One possible future work to do is to tomographically reconstruct the past quantum state using experimental data. Let's first briefly review the Past Quantum State theory to refresh our mind. The state of a quantum system at time t can be described by the density matrix $\rho(t)$ which represents our knowledge of the system at that time. The probability for the outcome m of some measurement Ω_m can be given by the expression $P(m) = Tr(\Omega_m \rho \Omega_m^\dagger)$ as we have discussed before. In our experiment, we can experimentally reconstruct the density matrix $\rho(t)$ from the measurement

data using the method of quantum state tomography which can be simply realized by rotation pulses followed by a projective measurement. Depending on how much knowledge we have about a quantum system, we can give a more complete description of a quantum system by a past quantum state (ρ, E) using both information before and after the measurement at time t, where E represents our knowledge of the system after time t. Then the probability for the measurement outcome is expressed by $P_p(m) = \frac{\mathrm{Tr}(\Omega_m \rho \Omega_m^\dagger E)}{\sum_n \mathrm{Tr}(\Omega_n \rho \Omega_n^\dagger E)}$. As we demonstrated in Chapter 4, the past quantum state can even make more confident predictions for the measurement outcomes. The question thereby is how can we tomographically reconstruct the past quantum state from the measurements carried out at time t?

If we want to reconstruct both ρ and E, we have to determine what is the pre-selected state ρ at time t, and what is the post-selected state E that is used to post-select the experimental runs in which the measurement data are obtained. If we use a Hermitian Ω_m, the probability $P_p(m)$ are invariant under the exchange of ρ and E. Thus even if we can obtain the density matrix ρ and effect matrix E with large set of experimental operators Ω_m, we still cannot distinguish these ρ and E. To solve this issue, we may have to borrow the non-Hermitian measurement operators and make composite, consecutive measurement at time t.

Our theory collaborator Professor Klaus Mølmer in Aarhus University proposed that we can realize such measurement operators in mutually unbiased bases (MUB). Two orthonormal bases of a Hilbert space are said to be mutually unbiased (MU) if the transition probabilities from each state in one basis to all states of the other basis are the same irrespective of which pair of states is chosen. That means we need two orthogonal bases $|m_{(j)}\rangle$ ($j = 1, 2$) for an $N-dimensional$ Hilbert space which safisfy $|\langle n(1)|m(2)\rangle| = 1/\sqrt{N}$ for all n, m. We can construct a two-parameter set of general POVM measurement with the expression $\Omega_{m,n}^{(j)} = (|n^{(j+1)}\rangle\langle n^{(j+1)}|)(|m^{(j)}\rangle\langle m^{(j)}|) = |n^{(j+1)}\rangle\langle m^{(j)}|/\sqrt{N}$ which satisfies $\sum_{m,n}(\Omega_{m,n}^{(j)})^\dagger(\Omega_{m,n}^{(j)}) = I$. The probability for a measurement outcome (m, n) based on the past quantum state is given by

$$P_p(m, n; j) = \frac{\langle m^{(j)}|\rho|m^{(j)}\rangle\langle n^{(j+1)}|E|n^{(j+1)}\rangle}{\sum_{m',n'}\langle m'^{(j)}|\rho|m'^{(j)}\rangle\langle n'^{(j+1)}|E|n'^{(j+1)}\rangle} \tag{7.1}$$

From the above equation, if E is normalized to have unit trace, we have the following relations:

$$\begin{aligned} \alpha_j(m) &\equiv \textstyle\sum_n P_p(m,n;j) = \langle m^{(j)}|\rho|m^{(j)}\rangle, \\ \beta_{j+1}(n) &\equiv \textstyle\sum_m P_p(m,n;j) = \langle n^{(j+1)}|E|n^{(j+1)}\rangle. \end{aligned} \tag{7.2}$$

Based on the derivations above, we know that the MUB property ensures that the effect matrix E from post-selection is not correlated with the density matrix ρ. Therefore, we can use the above two separate sets of probabilities $\alpha_j(m)$ and $\beta_{j+1}(n)$ to tomographically reconstruct the density matrix ρ and the effect matrix E in the normal tomography as we did before.

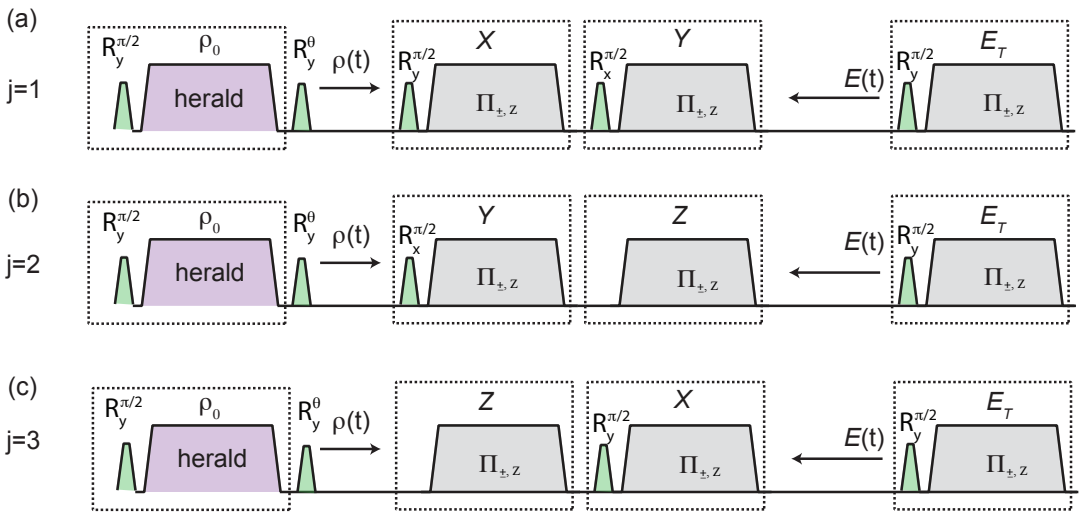

Figure 7.1: Experimental sequences for Past Quantum state tomography. (a, b, c) Different experiment sequences for different basis j. The qubit is first prepared in a initial state ρ_0. Then we apply a unitary rotation R_y^θ and weakly measure it which causes the qubit dephasing. Later on, the qubit is subject sequential measurements (X, Y), (Y, Z) and (Z, X) to realize the MUB. After these measurements, the qubit is again subjected to weak measurement for some amount of time. Finally, the qubit is rotated by a $\pi/2$ pulse along y followed by a projective measurement to determine E_T.

In the experiment, we can first prepare initial state to be either ground or excited state by a $\pi/2$ rotation pulse along the y axis followed by a strong projective mea-

surement. We then apply a unitary rotation R_y^θ to the qubit . After that, the qubit is subject to probing which causes the qubit to dephase. Second, we then perform some sequential measurements as illustrated in Fig. 7.1 and we can get the measurement outcomes m, n for different j. Finally, we determine the value of the effect matrix E_T simply by a rotation pulse followed by a projective measurement. E can be propagated backwards in time as we did in Chapter 4. We run the experiment many times and then calculate $\alpha_j(m)$ and $\beta_{j+1}(n)$ based on the occurrence of different value of m and n for different j. Thus we can construct ρ and E from the data and compare with the matrices we calculate by propagating the ρ forward and E backward with different initial ρ_0 and E_T.

Bibliography

[1] M. H. Devoret and R. J. Schoelkopf. Superconducting Circuits for Quantum Information: An Outlook. *Science*, 339(6124):1169–1174, 2013.

[2] Justin Dressel, Mehul Malik, Filippo M. Miatto, Andrew N. Jordan, and Robert W. Boyd. Colloquium. *Rev. Mod. Phys.*, 86:307–316, Mar 2014.

[3] M. H. Devoret. *in Quantum Fluctuations (Les Houches Session LXIII), edited by S. Reynaud, E. Giacobino, and J. Zinn-Justin*. Cambridge University Press, 1997.

[4] Chad Rigetti, Jay M. Gambetta, Stefano Poletto, B. L. T. Plourde, Jerry M. Chow, A. D. Córcoles, John A. Smolin, Seth T. Merkel, J. R. Rozen, George A. Keefe, Mary B. Rothwell, Mark B. Ketchen, and M. Steffen. Superconducting qubit in a waveguide cavity with a coherence time approaching 0.1 ms. *Phys. Rev. B*, 86:100506, Sep 2012.

[5] Oliver Dial, Douglas T McClure, Stefano Poletto, G A Keefe, Mary Beth Rothwell, Jay M Gambetta, David W Abraham, Jerry M Chow, and Matthias Steffen. Bulk and surface loss in superconducting transmon qubits. *Superconductor Science and Technology*, 29(4):044001, 2016.

[6] Y. Nakamura, Yu. A. Pashkin, and J. S. Tsai. Coherent control of macroscopic quantum states in a single-Cooper-pair box. *Nature*, 398, 1999.

[7] David P. DiVincenzo. Quantum Computation. *Science*, 270(5234):255–261, 1995.

[8] Iulia Buluta and Franco Nori. Quantum Simulators. *Science*, 326(5949):108–111, 2009.

[9] Max Hofheinz, Benjamin Huard, and Fabien Portier. Foreword. *Comptes Rendus Physique*, 17(7):679 – 683, 2016. Quantum microwaves / Micro-ondes quantiques.

[10] S. Weinreb, M. W. Pospieszalski, and R. Norrod. Cryogenic, HEMT, low-noise receivers for 1.3 to 43 GHz range. In *1988., IEEE MTT-S International Microwave Symposium Digest*, pages 945–948 vol.2, 1988.

[11] B. Yurke, L. R. Corruccini, P. G. Kaminsky, L. W. Rupp, A. D. Smith, A. H. Silver, R. W. Simon, and E. A. Whittaker. Observation of parametric amplification and deamplification in a Josephson parametric amplifier. *Phys. Rev. A*, 39:2519–2533, Mar 1989.

[12] B. Yurke, M. L. Roukes, R. Movshovich, and A. N. Pargellis. A lownoise seriesarray Josephson junction parametric amplifier. *Applied Physics Letters*, 69(20):3078–3080, 1996.

[13] E. M. Levenson-Falk, R. Vijay, and I. Siddiqi. Nonlinear microwave response of aluminum weak-link Josephson oscillators. *Applied Physics Letters*, 98(12):123115, 2011.

[14] M. Hatridge, R. Vijay, D. H. Slichter, John Clarke, and I. Siddiqi. Dispersive magnetometry with a quantum limited SQUID parametric amplifier. *Phys. Rev. B*, 83:134501, Apr 2011.

[15] Kevin O'Brien, Chris Macklin, Irfan Siddiqi, and Xiang Zhang. Resonant Phase Matching of Josephson Junction Traveling Wave Parametric Amplifiers. *Phys. Rev. Lett.*, 113:157001, Oct 2014.

[16] C. Macklin, K. O'Brien, D. Hover, M. E. Schwartz, V. Bolkhovsky, X. Zhang, W. D. Oliver, and I. Siddiqi. A near–quantum-limited Josephson traveling-wave parametric amplifier. 350(6258):307–310, 2015.

[17] M. A. Castellanos-Beltran, K. D. Irwin, G. C. Hilton, L. R. Vale, and K. W. Lehnert. Amplification and squeezing of quantum noise with a tunable Josephson metamaterial. *Nat Phys*, 4:929–931, 2008.

[18] T. C. White, J. Y. Mutus, I.-C. Hoi, R. Barends, B. Campbell, Yu Chen, Z. Chen, B. Chiaro, A. Dunsworth, E. Jeffrey, J. Kelly, A. Megrant, C. Neill, P. J. J. O'Malley, P. Roushan, D. Sank, A. Vainsencher, J. Wenner, S. Chaudhuri, J. Gao, and John M. Martinis. Traveling wave parametric amplifier with Josephson junctions using minimal resonator phase matching. *Applied Physics Letters*, 106(24):242601, 2015.

[19] J. Y. Mutus, T. C. White, R. Barends, Yu Chen, Z. Chen, B. Chiaro, A. Dunsworth, E. Jeffrey, J. Kelly, A. Megrant, C. Neill, P. J. J. O'Malley, P. Roushan, D. Sank, A. Vainsencher, J. Wenner, K. M. Sundqvist, A. N. Cleland, and John M. Martinis. Strong environmental coupling in a Josephson parametric amplifier. *Applied Physics Letters*, 104(26):263513, 2014.

[20] K. W. Murch, S. J. Weber, K. M. Beck, E. Ginossar, and I. Siddiqi. Reduction of the radiative decay of atomic coherence in squeezed vacuum. *Nature*, 499(7456):62–65, 07 2013.

[21] K. W. Murch, S. J. Weber, K. M. Beck, E. Ginossar, and I. Siddiqi. Reduction of the radiative decay of atomic coherence in squeezed vacuum. *Nature*, 499(7456):62–65, 07 2013.

[22] T. Walter, P. Kurpiers, S. Gasparinetti, P. Magnard, A. Potoc**c**nik, Y. Salathé, M. Pechal, M. Mondal, M. Oppliger, C. Eichler, and A. Wallraff. Rapid High-Fidelity Single-Shot Dispersive Readout of Superconducting Qubits. *Phys. Rev. Applied*, 7:054020, May 2017.

[23] Richard P. Feynman, Robert Leighton, and Matthew Sands. *The Feynman Lectures on Physics, Desktop Edition Volume III*. Online, 2013.

[24] L. DiCarlo, J. M. Chow, J. M. Gambetta, Lev S. Bishop, B. R. Johnson, D. I. Schuster, J. Majer, A. Blais, L. Frunzio, S. M. Girvin, and R. J. Schoelkopf. Demonstration of two-qubit algorithms with a superconducting quantum processor. *Nature*, 460(7252):240–244, 07 2009.

[25] T. D. Ladd, F. Jelezko, R. Laflamme, Y. Nakamura, C. Monroe, and J. L. O/'Brien.

[26] Jiangfeng Du, Nanyang Xu, Xinhua Peng, Pengfei Wang, Sanfeng Wu, and Dawei Lu. NMR Implementation of a Molecular Hydrogen Quantum Simulation with Adiabatic State Preparation. *Phys. Rev. Lett.*, 104:030502, Jan 2010.

[27] Erik Lucero, R. Barends, Y. Chen, J. Kelly, M. Mariantoni, A. Megrant, P. O'Malley, D. Sank, A. Vainsencher, J. Wenner, T. White, Y. Yin, A. N. Cleland, and John M. Martinis. Computing prime factors with a Josephson phase qubit quantum processor. *Nat Phys*, 8(10):719–723, 10 2012.

[28] Steven J. Weber, Gabriel O. Samach, David Hover, Simon Gustavsson, David K. Kim, Alexander Melville, Danna Rosenberg, Adam P. Sears, Fei Yan, Jonilyn L. Yoder, William D. Oliver, and Andrew J. Kerman. Coherent Coupled Qubits for Quantum Annealing. *Phys. Rev. Applied*, 8:014004, Jul 2017.

[29] Xiao-Qi Zhou, Pruet Kalasuwan, Timothy C. Ralph, and Jeremy L. O'Brien. Calculating unknown eigenvalues with a quantum algorithm. *Nat Photon*, 7(3):223–228, 03 2013.

[30] Y. P. Zhong, D. Xu, P. Wang, C. Song, Q. J. Guo, W. X. Liu, K. Xu, B. X. Xia, C.-Y. Lu, Siyuan Han, Jian-Wei Pan, and H. Wang. Emulating Anyonic Fractional Statistical Behavior in a Superconducting Quantum Circuit. *Phys. Rev. Lett.*, 117:110501, Sep 2016.

[31] M. Reagor et. al. Demonstration of universal parametric entangling gates on a multi-Qubit Lattice. *arXiv:1706.06570*, 2017.

[32] Michel H. devoret and John M. Martinis. Implementing Qubits with Superconducting Integrated Circuits. *Quantum Information Processing*, 3(1):163–203, Oct 2004.

[33] Iulia Buluta, Sahel Ashhab, and Franco Nori. Natural and artificial atoms for quantum computation. *Reports on Progress in Physics*, 74(10):104401, 2011.

[34] Y. Nakamura, Yu. A. Pashkin, and J. S. Tsai. Rabi Oscillations in a Josephson-Junction Charge Two-Level System. *Phys. Rev. Lett.*, 87:246601, Nov 2001.

[35] Jonathan R. Friedman, Vijay Patel, W. Chen, S. K. Tolpygo, and J. E. Lukens. Quantum superposition of distinct macroscopic states. *Nature*, 406(6791):43–46, 07 2000.

[36] John M. Martinis, Michel H. Devoret, and John Clarke. Energy-Level Quantization in the Zero-Voltage State of a Current-Biased Josephson Junction. *Phys. Rev. Lett.*, 55:1543–1546, Oct 1985.

[37] John M. Martinis, S. Nam, J. Aumentado, and C. Urbina. Rabi Oscillations in a Large Josephson-Junction Qubit. *Phys. Rev. Lett.*, 89:117901, Aug 2002.

[38] Hanhee Paik, D. I. Schuster, Lev S. Bishop, G. Kirchmair, G. Catelani, A. P. Sears, B. R. Johnson, M. J. Reagor, L. Frunzio, L. I. Glazman, S. M. Girvin, M. H. Devoret, and R. J. Schoelkopf. Observation of High Coherence in Josephson Junction Qubits Measured in a Three-Dimensional Circuit QED Architecture. *Phys. Rev. Lett.*, 107:240501, Dec 2011.

[39] Immanuel Bloch. Quantum coherence and entanglement with ultracold atoms in optical lattices. *Nature*, 453(7198):1016–1022, 06 2008.

[40] Rainer Blatt and David Wineland. Entangled states of trapped atomic ions. *Nature*, 453(7198):1008–1015, 06 2008.

[41] M. V. Gurudev Dutt, L. Childress, L. Jiang, E. Togan, J. Maze, F. Jelezko, A. S. Zibrov, P. R. Hemmer, and M. D. Lukin. Quantum Register Based on Individual Electronic and Nuclear Spin Qubits in Diamond. *Science*, 316(5829):1312–1316, 2007.

[42] Ronald Hanson and David D. Awschalom. Coherent manipulation of single spins in semiconductors. *Nature*, 453(7198):1043–1049, 06 2008.

[43] Pieter Kok, W. J. Munro, Kae Nemoto, T. C. Ralph, Jonathan P. Dowling, and G. J. Milburn. Linear optical quantum computing with photonic qubits. *Rev. Mod. Phys.*, 79:135–174, Jan 2007.

[44] C. Barthel, D. J. Reilly, C. M. Marcus, M. P. Hanson, and A. C. Gossard. Rapid Single-Shot Measurement of a Singlet-Triplet Qubit. *Phys. Rev. Lett.*, 103:160503, Oct 2009.

[45] M. Hatridge, R. Vijay, D. H. Slichter, John Clarke, and I. Siddiqi. Dispersive magnetometry with a quantum limited SQUID parametric amplifier. *Phys. Rev. B*, 83:134501, Apr 2011.

[46] R. Vijay, D. H. Slichter, and I. Siddiqi. Observation of Quantum Jumps in a Superconducting Artificial Atom. *Phys. Rev. Lett.*, 106:110502, Mar 2011.

[47] A. Yariv. *Quantum electronics*. Woodbury, 1988.

[48] R. Vijay, M. H. Devoret, and I. Siddiqi. Invited Review Article: The Josephson bifurcation amplifier. *Review of Scientific Instruments*, 80(11):111101, 2009.

[49] Mankei Tsang. Optimal waveform estimation for classical and quantum systems via time-symmetric smoothing. *Phys. Rev. A*, 80:033840, Sep 2009.

[50] Søren Gammelmark, Brian Julsgaard, and Klaus Mølmer. Past Quantum States of a Monitored System. *Phys. Rev. Lett.*, 111:160401, Oct 2013.

[51] Y. Aharonov, S. Popescu, and J. Tollaksen. A time-symmetric formulation of quantum mechanics. *Physics Today*, 63:27, 2010.

[52] Y. Aharonov, S. Popescu, and J. Tollaksen. Time-symmetric quantum mechanics questioned and defended. *Physics Today*, 64:62, 2011.

[53] Y. Aharonov, S. Popescu, and J. Tollaksen. Consistent treatments of quantum mechanics. *Physics Today*, 64:9, 2011.

[54] Yakir Aharonov, David Z. Albert, and Lev Vaidman. How the result of a measurement of a component of the spin of a spin-1/2 particle can turn out to be 100. *Phys. Rev. Lett.*, 60:1351–1354, Apr 1988.

[55] Mankei Tsang. Time-Symmetric Quantum Theory of Smoothing. *Phys. Rev. Lett.*, 102:250403, Jun 2009.

[56] Ivonne Guevara and Howard Wiseman. Quantum State Smoothing. *Phys. Rev. Lett.*, 115:180407, Oct 2015.

[57] R. Vijay, C. Macklin, D. H. Slichter, S. J. Weber, K. W. Murch, R. Naik, A. N. Korotkov, and I. Siddiqi. Stabilizing Rabi oscillations in a superconducting qubit using quantum feedback. *Nature*, 490(7418):77–80, 10 2012.

[58] P. Campagne-Ibarcq, S. Jezouin, N. Cottet, P. Six, L. Bretheau, F. Mallet, A. Sarlette, P. Rouchon, and B. Huard. Using Spontaneous Emission of a Qubit as a Resource for Feedback Control. *Phys. Rev. Lett.*, 117:060502, Aug 2016.

[59] M. Naghiloo, D. Tan, P. M. Harrington, J. J. Alonso, E. Lutz, A. Romito, and K. W. Murch. Thermodynamics along individual trajectories of a quantum bit. *arXiv:1703.05885v1*, 2017.

[60] D. Tan, M. Naghiloo, K. Mølmer, and K. W. Murch. Quantum smoothing for classical mixtures. *Phys. Rev. A*, 94:050102, Nov 2016.

[61] D. Tan, S. J. Weber, I. Siddiqi, K. Mølmer, and K. W. Murch. Prediction and Retrodiction for a Continuously Monitored Superconducting Qubit. *Phys. Rev. Lett.*, 114:090403, Mar 2015.

[62] N. Foroozani, M. Naghiloo, D. Tan, K. Mølmer, and K. W. Murch. Correlations of the Time Dependent Signal and the State of a Continuously Monitored Quantum System. *Phys. Rev. Lett.*, 116:110401, Mar 2016.

[63] D. Tan, N. Foroozani, M. Naghiloo, A. H. Kiilerich, K. Mølmer, and K. W. Murch. Homodyne monitoring of postselected decay. *Phys. Rev. A*, 96:022104, Aug 2017.

[64] David J. Griffiths. *Introduction to Quantum Mechanics, 2nd Edition*. Pearson, 2005.

[65] J. J. Sakurai. *Modern Quantum Mechanics*. Addison-Wesley Publishing Company, Inc., 1994.

[66] M. Born. On Quantum Mechanics. *Z. Physik*, 26:379, 1924.

[67] K. Jacobs. *Quantum Measurement Theory*. Cambridge University Press, 2014.

[68] V. B. Braginsky and F. Y. Khalili. *Quantum Measurement*. Cambridge University Press, 1992.

[69] Yakir Aharonov, Peter G. Bergmann, and Joel L. Lebowitz. Time Symmetry in the Quantum Process of Measurement. *Phys. Rev.*, 134:B1410–B1416, Jun 1964.

[70] Satosi Watanabe. Symmetry of Physical Laws. Part III. Prediction and Retrodiction. *Rev. Mod. Phys.*, 27:179–186, Apr 1955.

[71] L. Vaidman. Past of a quantum particle. *Phys. Rev. A*, 87:052104, May 2013.

[72] Simon E. Nigg, Hanhee Paik, Brian Vlastakis, Gerhard Kirchmair, S. Shankar, Luigi Frunzio, M. H. Devoret, R. J. Schoelkopf, and S. M. Girvin. Black-Box Superconducting Circuit Quantization. *Phys. Rev. Lett.*, 108:240502, Jun 2012.

[73] Uri Vool and Michel H. Devoret. Introduction to Quantum Electromagnetic Circuits. *arXiv:1610.03438*, 2016.

[74] H. Goldstein. *Classical Mechanics, 2nd edition*. Addison-Wesley Publishing Company, Inc., 1980.

[75] B.D. Josephson. Possible new effects in superconductive tunnelling. *Physics Letters*, 1(7):251 – 253, 1962.

[76] William D. Oliver. *Quantum Information Procssing: Lecture Notes of the 44th IFF Spring School 2013, Ed: David P. DiVincenzo*. Juelich, 2013.

[77] J. Clarke and A. I. Braginski. *The SQUID Handbook*. Wiley, Weinheim, 2004.

[78] C. C. Gerry and P. L. Knight. *Introductory Quantum Optics*. Cambridge University Press, 2005.

[79] Nathan K.Langford. Circuit QED—Lecture Notes. *arXiv:1310.1897v1*, 2013.

[80] Yu. A. Pashkin, O. Astafiev, T. Yamamoto, Y. Nakamura, and J. S. Tsai. Josephson charge qubits: a brief review. *Quantum Information Processing*, 8(2):55–80, Jun 2009.

[81] J. M. Martinis M. H. Devoret, A. Wallraff. Superconducting Qubits: A Short Review. *arXiv:0411174*, 2004.

[82] Jens Koch, Terri M. Yu, Jay Gambetta, A. A. Houck, D. I. Schuster, J. Majer, Alexandre Blais, M. H. Devoret, S. M. Girvin, and R. J. Schoelkopf. Charge-insensitive qubit design derived from the Cooper pair box. *Phys. Rev. A*, 76:042319, Oct 2007.

[83] Marcus P. da Silva Chad Rigetti Nicolas Didier, Eyob A. Sete. Analytical modeling of parametrically-modulated transmon qubits. *arXiv:1706.06566*, 2013.

[84] Daniel Sank, Zijun Chen, Mostafa Khezri, J. Kelly, R. Barends, B. Campbell, Y. Chen, B. Chiaro, A. Dunsworth, A. Fowler, E. Jeffrey, E. Lucero, A. Megrant, J. Mutus, M. Neeley, C. Neill, P. J. J. O'Malley, C. Quintana, P. Roushan, A. Vainsencher, T. White, J. Wenner, Alexander N. Korotkov, and John M. Martinis. Measurement-Induced State Transitions in a Superconducting Qubit: Beyond the Rotating Wave Approximation. *Phys. Rev. Lett.*, 117:190503, Nov 2016.

[85] Fei Yan, Simon Gustavsson, Archana Kamal, Jeffrey Birenbaum, Adam P Sears, David Hover, Ted J. Gudmundsen, Danna Rosenberg, Gabriel Samach, S Weber, Jonilyn L. Yoder, Terry P. Orlando, John Clarke, Andrew J. Kerman, and William D. Oliver. The flux qubit revisited to enhance coherence and reproducibility. 7:12964 EP –, 11 2016.

[86] Dirk Englund, Andrei Faraon, Ilya Fushman, Nick Stoltz, Pierre Petroff, and Jelena Vuckovic. Controlling cavity reflectivity with a single quantum dot. *Nature*, 450(7171):857–861, 12 2007.

[87] Yves Colombe, Tilo Steinmetz, Guilhem Dubois, Felix Linke, David Hunger, and Jakob Reichel. Strong atom-field coupling for Bose-Einstein condensates in an optical cavity on a chip. *Nature*, 450(7167):272–276, 11 2007.

[88] J. Q. You and Franco Nori. Atomic physics and quantum optics using superconducting circuits. *Nature*, 474(7353):589–597, 06 2011.

[89] Mika A. Sillanpaa, Jae I. Park, and Raymond W. Simmonds. Coherent quantum state storage and transfer between two phase qubits via a resonant cavity. *Nature*, 449(7161):438–442, 09 2007.

[90] J. Majer, J. M. Chow, J. M. Gambetta, Jens Koch, B. R. Johnson, J. A. Schreier, L. Frunzio, D. I. Schuster, A. A. Houck, A. Wallraff, A. Blais, M. H.

Devoret, S. M. Girvin, and R. J. Schoelkopf. Coupling superconducting qubits via a cavity bus. *Nature*, 449(7161):443–447, 09 2007.

[91] S. Haroche and J.-M. Raimond. *Exploring the Quantum: Atoms, Cavities, and Photons*. OUP Oxford, 2006.

[92] Hanhee Paik, D. I. Schuster, Lev S. Bishop, G. Kirchmair, G. Catelani, A. P. Sears, B. R. Johnson, M. J. Reagor, L. Frunzio, L. I. Glazman, S. M. Girvin, M. H. Devoret, and R. J. Schoelkopf. Observation of High Coherence in Josephson Junction Qubits Measured in a Three-Dimensional Circuit QED Architecture. *Phys. Rev. Lett.*, 107:240501, Dec 2011.

[93] Alexandre Blais, Ren-Shou Huang, Andreas Wallraff, S. M. Girvin, and R. J. Schoelkopf. Cavity quantum electrodynamics for superconducting electrical circuits: An architecture for quantum computation. *Phys. Rev. A*, 69:062320, Jun 2004.

[94] J. Q. You and Franco Nori. Quantum information processing with superconducting qubits in a microwave field. *Phys. Rev. B*, 68:064509, Aug 2003.

[95] Bruce W. Shore and Peter L. Knight. The Jaynes-Cummings Model. *Journal of Modern Optics*, 40(7):1195–1238, 1993.

[96] E. T. Jaynes and F. W. Cummings. Comparison of quantum and semiclassical radiation theories with application to the beam maser. *Proceedings of the IEEE*, 51(1):89–109, Jan 1963.

[97] D. I. Schuster. *Circuit Quantum electrodynamics*. Yale University, 2007.

[98] Yu-xi Liu, L. F. Wei, and Franco Nori. Measuring the quality factor of a microwave cavity using superconducting qubit devices. *Phys. Rev. A*, 72:033818, Sep 2005.

[99] Maxime Boissonneault, J. M. Gambetta, and Alexandre Blais. Dispersive regime of circuit QED: Photon-dependent qubit dephasing and relaxation rates. *Phys. Rev. A*, 79:013819, Jan 2009.

[100] Alexandre Blais, Ren-Shou Huang, Andreas Wallraff, S. M. Girvin, and R. J. Schoelkopf. Cavity quantum electrodynamics for superconducting electrical circuits: An architecture for quantum computation. *Phys. Rev. A*, 69:062320, Jun 2004.

[101] A. Lupaşcu, C. J. M. Verwijs, R. N. Schouten, C. J. P. M. Harmans, and J. E. Mooij. Nondestructive Readout for a Superconducting Flux Qubit. *Phys. Rev. Lett.*, 93:177006, Oct 2004.

[102] I. Siddiqi, R. Vijay, M. Metcalfe, E. Boaknin, L. Frunzio, R. J. Schoelkopf, and M. H. Devoret. Dispersive measurements of superconducting qubit coherence with a fast latching readout. *Phys. Rev. B*, 73:054510, Feb 2006.

[103] S. J. Weber. *Quantum Trajectories of a Superconducting Qubit*. University of California, Berkeley, 2014.

[104] D. H. Slichter. *Quantum Jumps and Measurement Backaction in a Superconducting Qubit*. University of California, Berkeley, 2014.

[105] Philippe Campagne-Ibarcq. *Circuit Quantum electrodynamics*. LPA-ENS Paris, 2015.

[106] Christopher Eichler and Andreas Wallraff. Controlling the dynamic range of a Josephson parametric amplifier. *EPJ Quantum Technology*, 1(1):2, Jan 2014.

[107] R. Vijay. *Josephson bifurcation amplifier: Amplifying quantum signals using a dynamical bifurcation*. University of California, Berkeley, 2008.

[108] C. W. Gardiner and M. J. Collett. Input and output in damped quantum systems: Quantum stochastic differential equations and the master equation. *Phys. Rev. A*, 31:3761–3774, Jun 1985.

[109] Carlton M. Caves, Joshua Combes, Zhang Jiang, and Shashank Pandey. Quantum limits on phase-preserving linear amplifiers. *Phys. Rev. A*, 86:063802, Dec 2012.

[110] K. W. Murch, S. J. Weber, C. Macklin, and I. Siddiqi. Observing single quantum trajectories of a superconducting qubit. *Nature*, 502:211, 2013.

[111] Nadav Katz, Matthew Neeley, M. Ansmann, Radoslaw C. Bialczak, M. Hofheinz, Erik Lucero, A. O'Connell, H. Wang, A. N. Cleland, John M. Martinis, and Alexander N. Korotkov. Reversal of the Weak Measurement of a Quantum State in a Superconducting Phase Qubit. *Phys. Rev. Lett.*, 101:200401, Nov 2008.

[112] E. Il'ichev, N. Oukhanski, A. Izmalkov, Th. Wagner, M. Grajcar, H.-G. Meyer, A. Yu. Smirnov, Alec Maassen van den Brink, M. H. S. Amin, and A. M. Zagoskin. Continuous Monitoring of Rabi Oscillations in a Josephson Flux Qubit. *Phys. Rev. Lett.*, 91:097906, Aug 2003.

[113] H. Wiseman and G. Milburn. *Quantum Measurement and Control*. Cambridge University Press, 2010.

[114] K. Jacobs and D. A. Steck. A straightforward introduction to continuous quantum measurement. *Contemp. Phys.*, 47:279, 2006.

[115] Søren. Gammelmark. *Efficient parametric inference, estimation and simulation of open quantum systems*. aarhus, 2013.

[116] M. A. Nielsen and I. L. Chuang. *Quantum Computation and Quantum Information*. Cambridge University Press, Cambridge, England, 2000.

[117] Michael A. Armen, Anthony E. Miller, and Hideo Mabuchi. Spontaneous Dressed-State Polarization in the Strong Driving Regime of Cavity QED. *Phys. Rev. Lett.*, 103:173601, Oct 2009.

[118] S. A. Vetterling W. T. Press, W. H. Teukolsky and B. P. Flannery. *Numerical Recipes: The Art of Scientific Computing*. Cambridge University Press, New York, 2007.

[119] R. Rabiner. A tutorial on hidden Markov models and selected applications in speech recognition. *Proc. IEEE*, 77:257, Aug 1989.

[120] D. H. Slichter, R. Vijay, S. J. Weber, S. Boutin, M. Boissonneault, J. M. Gambetta, A. Blais, and I. Siddiqi. Measurement-Induced Qubit State Mixing in Circuit QED from Up-Converted Dephasing Noise. *Phys. Rev. Lett.*, 109:153601, Oct 2012.

[121] Zijun Chen, Julian Kelly, Chris Quintana, R. Barends, B. Campbell, Yu Chen, B. Chiaro, A. Dunsworth, A. G. Fowler, E. Lucero, E. Jeffrey, A. Megrant, J. Mutus, M. Neeley, C. Neill, P. J. J. O'Malley, P. Roushan, D. Sank, A. Vainsencher, J. Wenner, T. C. White, A. N. Korotkov, and John M. Martinis. Measuring and Suppressing Quantum State Leakage in a Superconducting Qubit. *Phys. Rev. Lett.*, 116:020501, Jan 2016.

[122] Evan Jeffrey, Daniel Sank, J. Y. Mutus, T. C. White, J. Kelly, R. Barends, Y. Chen, Z. Chen, B. Chiaro, A. Dunsworth, A. Megrant, P. J. J. O'Malley, C. Neill, P. Roushan, A. Vainsencher, J. Wenner, A. N. Cleland, and John M. Martinis. Fast Accurate State Measurement with Superconducting Qubits. *Phys. Rev. Lett.*, 112:190504, May 2014.

[123] J. E. Johnson, C. Macklin, D. H. Slichter, R. Vijay, E. B. Weingarten, John Clarke, and I. Siddiqi. Heralded State Preparation in a Superconducting Qubit. *Phys. Rev. Lett.*, 109:050506, Aug 2012.

[124] D. Ristè, C. C. Bultink, K. W. Lehnert, and L. DiCarlo. Feedback Control of a Solid-State Qubit Using High-Fidelity Projective Measurement. *Phys. Rev. Lett.*, 109:240502, Dec 2012.

[125] A. Wallraff, D. I. Schuster, A. Blais, L. Frunzio, J. Majer, M. H. Devoret, S. M. Girvin, and R. J. Schoelkopf. Approaching Unit Visibility for Control of a Superconducting Qubit with Dispersive Readout. *Phys. Rev. Lett.*, 95:060501, Aug 2005.

[126] A. N. Korotkov. Quantum Bayesian approach to circuit QED measurement. *arXiv:1111.4016*, 2011.

[127] J. S. Bell. On the Einstein Podolsty Rosen Paradox. *Physics*, 1(3):195–200, Aug 1965.

[128] Alain Aspect, Philippe Grangier, and Gérard Roger. Experimental Tests of Realistic Local Theories via Bell's Theorem. *Phys. Rev. Lett.*, 47:460–463, Aug 1981.

[129] J. P. Groen, D. Ristè, L. Tornberg, J. Cramer, P. C. de Groot, T. Picot, G. Johansson, and L. DiCarlo. Partial-Measurement Backaction and Nonclassical Weak Values in a Superconducting Circuit. *Phys. Rev. Lett.*, 111:090506, Aug 2013.

[130] A. Palacios-Laloy, F. Mallet, F. Nguyen, F. Bertet, D. Vion, D. Esteve, and A. Korotkov. Experimental violation of a Bell's inequality in time with weak measurement. *Nature Physics*, 6:442–447, 2010.

[131] Nathan S. Williams and Andrew N. Jordan. Weak Values and the Leggett-Garg Inequality in Solid-State Qubits. *Phys. Rev. Lett.*, 100:026804, Jan 2008.

[132] M. E. Goggin, M. P. Almeida, M. Barbieri, B. P. Lanyon, J. L. OBrien, A. G. White, and G. J. Pryde. Violation of the LeggettGarg inequality with weak measurements of photons. *Proc. Natl. Acad. Sci. U.S.A.*, 108:1256, 2011.

[133] T C White, J Y Mutus, J Dressel, J Kelly, R Barends, E Jeffrey, D Sank, A Megrant, B Campbell, Yu Chen, Z Chen, B Chiaro, A Dunsworth, I-C Hoi, C Neill, P J J O'Malley, P Roushan, A Vainsencher, J Wenner, A N Korotkov, and John M Martinis. Preserving entanglement during weak measurement demonstrated with a violation of the Bell–Leggett–Garg inequality. 2:15022 EP –, 02 2016.

[134] A. J. Leggett and Anupam Garg. Quantum mechanics versus macroscopic realism: Is the flux there when nobody looks? *Phys. Rev. Lett.*, 54:857–860, Mar 1985.

[135] S. J. Weber, A. Chantasri, J. Dressel, A. N. Jordan, K. W. Murch, and I. Siddiqi. Mapping the optimal route between two quantum states. *Nature*, 511:570–573, 2014.

[136] Justin Dressel. Weak values as interference phenomena. *Phys. Rev. A*, 91:032116, Mar 2015.

[137] Mankei Tsang, Howard M. Wiseman, and Carlton M. Caves. Fundamental Quantum Limit to Waveform Estimation. *Phys. Rev. Lett.*, 106:090401, Mar 2011.

[138] T. A. Wheatley, D. W. Berry, H. Yonezawa, D. Nakane, H. Arao, D. T. Pope, T. C. Ralph, H. M. Wiseman, A. Furusawa, and E. H. Huntington. Adaptive Optical Phase Estimation Using Time-Symmetric Quantum Smoothing. *Phys. Rev. Lett.*, 104:093601, Mar 2010.

[139] T. Rybarczyk, B. Peaudecerf, M. Penasa, S. Gerlich, B. Julsgaard, K. Mølmer, S. Gleyzes, M. Brune, J. M. Raimond, S. Haroche, and I. Dotsenko. Forward-backward analysis of the photon-number evolution in a cavity. *Phys. Rev. A*, 91:062116, Jun 2015.

[140] Onur Hosten and Paul Kwiat. Observation of the Spin Hall Effect of Light via Weak Measurements. *Science*, 319(5864):787–790, 2008.

[141] Markus Ansmann, H. Wang, Radoslaw C. Bialczak, Max Hofheinz, Erik Lucero, M. Neeley, A. D. O'Connell, D. Sank, M. Weides, J. Wenner, A. N. Cleland, and John M. Martinis. Violation of Bell's inequality in Josephson phase qubits. *Nature*, 461(7263):504–506, 09 2009.

[142] Roy J. Glauber. The Quantum Theory of Optical Coherence. *Phys. Rev.*, 130:2529–2539, Jun 1963.

[143] R. Hanbury-Brown and R. Q. Twiss. Correlation between Photons in two Coherent Beams of Light. *Nature*, 177:27, 1956.

[144] Rusko Ruskov, Alexander N. Korotkov, and Ari Mizel. Signatures of Quantum Behavior in Single-Qubit Weak Measurements. *Phys. Rev. Lett.*, 96:200404, May 2006.

[145] P. Campagne-Ibarcq, L. Bretheau, E. Flurin, A. Auffèves, F. Mallet, and B. Huard. Observing Interferences between Past and Future Quantum States in Resonance Fluorescence. *Phys. Rev. Lett.*, 112:180402, May 2014.

[146] P. Campagne-Ibarcq, L. Bretheau, E. Flurin, A. Auffèves, F. Mallet, and B. Huard. Observing Interferences between Past and Future Quantum States in Resonance Fluorescence. *Phys. Rev. Lett.*, 112:180402, May 2014.

[147] H. Hayashi, G. Kimura, and Y. Ota. Kraus representation in the presence of initial correlations. *Phys. Rev. A*, 67:062109, Aug 2003.

[148] K. Kraus. *States, Effects, and Operations: Fundamental Notations of Quantum Theory*. Springer-Verlag, Berlin, 1983.

[149] Qing Xu, Eliska Greplova, Brian Julsgaard, and Klaus Mølmer. Correlation functions and conditioned quantum dynamics in photodetection theory. *Physica Scripta*, 90(12):128004, 2015.

[150] C. Gardiner and P. Zoller. *Quantum noise: a handbook of Markovian and non-Markovian quantum stochastic methods with applications to quantum optics*. Springer Science & Business Media, 2004.

[151] Yuecheng Shen, Matthew Bradford, and Jung-Tsung Shen. Single-Photon Diode by Exploiting the Photon Polarization in a Waveguide. *Phys. Rev. Lett.*, 107:173902, Oct 2011.

[152] Yuecheng Shen and Jung-Tsung Shen. Photonic-Fock-state scattering in a waveguide-QED system and their correlation functions. *Phys. Rev. A*, 92:033803, Sep 2015.

[153] Andrew Silberfarb, Poul S. Jessen, and Ivan H. Deutsch. Quantum State Reconstruction via Continuous Measurement. *Phys. Rev. Lett.*, 95:030402, Jul 2005.

[154] Areeya Chantasri and Andrew N. Jordan. Stochastic path-integral formalism for continuous quantum measurement. *Phys. Rev. A*, 92:032125, Sep 2015.

[155] Søren Gammelmark and Klaus Mølmer. Bayesian parameter inference from continuously monitored quantum systems. *Phys. Rev. A*, 87:032115, Mar 2013.

[156] E. M. Purcell, H. C. Torrey, and R. V. Pound. Resonance Absorption by Nuclear Magnetic Moments in a Solid. *Phys. Rev.*, 69:37–38, Jan 1946.

[157] O. Astafiev, A. M. Zagoskin, A. A. Abdumalikov, Yu. A. Pashkin, T. Yamamoto, K. Inomata, Y. Nakamura, and J. S. Tsai. Resonance Fluorescence of a Single Artificial Atom. *Science*, 327(5967):840–843, 2010.

[158] M. Naghiloo, N. Foroozani, D. Tan, A. Jadbabaie, and K. W. Murch. Mapping quantum state dynamics in spontaneous emission. *Nature Communications*, 7:11527, 2016.

[159] P. Campagne-Ibarcq, P. Six, L. Bretheau, A. Sarlette, M. Mirrahimi, P. Rouchon, and B. Huard. Observing Quantum State Diffusion by Heterodyne Detection of Fluorescence. *Phys. Rev. X*, 6:011002, Jan 2016.

[160] Sebastien Gleyzes, Stefan Kuhr, Christine Guerlin, Julien Bernu, Samuel Deleglise, Ulrich Busk Hoff, Michel Brune, Jean-Michel Raimond, and Serge Haroche. Quantum jumps of light recording the birth and death of a photon in a cavity. *Nature*, 446(7133):297–300, 03 2007.

[161] Aephraim M. Steinberg. Conditional probabilities in quantum theory and the tunneling-time controversy. *Phys. Rev. A*, 52:32–42, Jul 1995.

[162] Anders Bolund and Klaus Mølmer. Stochastic excitation during the decay of a two-level emitter subject to homodyne and heterodyne detection. *Phys. Rev. A*, 89:023827, Feb 2014.

[163] M. Naghiloo, D. Tan, P. M. Harrington, K., P. Lewalle, A. N. Jordan, and K. W. Murch. Quantum caustics in resonance fluorescence trajectories. *arXiv:1612.03189*, 2016.

[164] K. Jacobs. *Stochastic Processes for Physicists: Understanding Noisy Systems*. Cambridge University Press, 2010.

[165] H. M. Wiseman. Weak values, quantum trajectories, and the cavity-QED experiment on wave-particle correlation. *Phys. Rev. A*, 65:032111, Feb 2002.

[166] Shengshi Pang, Justin Dressel, and Todd A. Brun. Entanglement-Assisted Weak Value Amplification. *Phys. Rev. Lett.*, 113:030401, Jul 2014.

[167] P. Ben Dixon, David J. Starling, Andrew N. Jordan, and John C. Howell. Ultrasensitive Beam Deflection Measurement via Interferometric Weak Value Amplification. *Phys. Rev. Lett.*, 102:173601, Apr 2009.